

DTIC® has determined on 28/07/2009 that this Technical Document has the Distribution Statement checked below. The current distribution for this document can be found in the DTIC® Technical Report Database.

☒ **DISTRIBUTION STATEMENT A.** Approved for public release; distribution is unlimited.

☐ **© COPYRIGHTED;** U.S. Government or Federal Rights License. All other rights and uses except those permitted by copyright law are reserved by the copyright owner.

☐ **DISTRIBUTION STATEMENT B.** Distribution authorized to U.S. Government agencies only (fill in reason) (date of determination). Other requests for this document shall be referred to (insert controlling DoD office)

☐ **DISTRIBUTION STATEMENT C.** Distribution authorized to U.S. Government Agencies and their contractors (fill in reason) (date of determination). Other requests for this document shall be referred to (insert controlling DoD office)

☐ **DISTRIBUTION STATEMENT D.** Distribution authorized to the Department of Defense and U.S. DoD contractors only (fill in reason) (date of determination). Other requests shall be referred to (insert controlling DoD office).

☐ **DISTRIBUTION STATEMENT E.** Distribution authorized to DoD Components only (fill in reason) (date of determination). Other requests shall be referred to (insert controlling DoD office).

☐ **DISTRIBUTION STATEMENT F.** Further dissemination only as directed by (inserting controlling DoD office) (date of determination) or higher DoD authority.

Distribution Statement F is also used when a document does not contain a distribution statement and no distribution statement can be determined.

☐ **DISTRIBUTION STATEMENT X.** Distribution authorized to U.S. Government Agencies and private individuals or enterprises eligible to obtain export-controlled technical data in accordance with DoDD 5230.25; (date of determination). DoD Controlling Office is (insert controlling DoD office).

AIR FORCE OFFICE OF SCIENTIFIC RESEARCH

04 SEP 2008

DTIC Data

Page 1 of 2

Purchase Request Number: FQ8671-0500655
BPN: F1ATA04337B655
Proposal Number: 05-NL-041
Research Title: (MEANS2 THEME) INTEGRATED ANALYSIS TOOLS FOR DETERMINATION OF STRUCTURAL INTEGRITY AND DURABILITY OF HIGH TEMPERATURE POLYMER MATRIX COMPOSITES
Type Submission: ~~New Work Effort~~ *Final Report*
Inst. Control Number: FA9550-05-1-0101DEF
Institution: PENNSYLVANIA STATE UNIVERSITY
Primary Investigator: Dr. Gregory Dillon
Invention Ind: none
Project/Task: 2306T / X
Program Manager: Dr. Charles Y-C. Lee

Objective:

To develop a materials qualification approach based on a combinatorial multi-scale modeling and optimization methodology for reduced qualification testing to obviate the need for exhaustive testing of HTPMC's in simulated service environments during the materials qualification process.

Approach:

Polymer processing and degradation models will be incorporated into selective micro-mechanics, meso-mechanics, and laminate models to predict environmental performance of polymer matrix composites. High fidelity polymer material models will be used to enable a minimum number of strategic tests for materials characterization vs. the current "empirical" approach, which is based on accumulating statistics from large test programs. A model-based design methodology will be developed for composite materials, which populates the Design Allowables Database while maintaining the fidelity of the current empirically established database. Computer models with the appropriate level of fidelity will be used to reduce the massive experimental testing and associated time required for qualification of new materials. Tools and approaches will be identified and targeted to provide the material supplier with a more efficient way to optimize the material for a particular application.

Progress:

Year: 2005 **Month:** 10

ANNUAL REPORT - 1 FEB 05 TO 31 AUG 05

Stevens Institute of Technology has made significant progress in developing a model of the thermo-oxidative process for polymer systems, that incorporates the effects of reaction rates, Fickian diffusion, time varying concentration gradients, consumption of reactants (solid and gas phase), and weight loss from a system under degradation. The model has been shown to correlate well with experimental oxidation layer growth at various exposure temperatures, and a sensitivity study has been performed in order to identify the parameters that have greatest effect on degradation system kinetics. The model has been incorporated into a finite element model of a representative element of a fiber composite and the resultant simulations have been shown to realistically represent the impact of multiple phases on degradation processes.

Year: 2005 **Month:** 12

Not required at this time.

AIR FORCE OFFICE OF SCIENTIFIC RESEARCH

04 SEP 2008

DTIC Data

Page 2 of 2

Progress:

Year: 2006 Month: 12

Annual Report:

Findings in this phase of the program have been in the general areas of polymer degradation characterization and modeling, incorporation into composite modeling and prediction of microcrack patterns based on composite architecture.

Year: 2008 Month: 08 Final

This report outlines an approach to reducing implementation cycle time for high temperature polymer matrix composites (PMCs) using integrated high fidelity physical models in preference to exhaustive experimentation and testing. The fundamental mechanisms of thermo-oxidative degradation of high temperature PMCs were studied and a three dimensional finite element modeling approach was developed that represents degradation, aging and oxidation effects. The effect of composite microstructure on damage development mechanisms was also explored using the finite element method. Digital Image Correlation was used to measure local (fiber level) stress and strain profiles in composites subjected to complex (bending) load conditions. Statistical analysis methods were also developed that may allow the relationship between composite architecture and variability in performance to be determined from measurable material attributes rather than large test databases.

REPORT DOCUMENTATION PAGE

Public reporting burden for this collection of information is estimated to average 1 hour per response, including the time for reviewing instructions, searching existing data needed, and completing and reviewing this collection of information. Send comments regarding this burden estimate or any other aspect of this collection of information, including suggestions to reduce this burden to Department of Defense, Washington Headquarters Services, Directorate for Information Operations and Reports (0704-0188), 1215 Jefferson Davis Highway, Suite 1204, Arlington, VA 22202-4302. Respondents should be aware that notwithstanding any other provision of law, no person shall be subject to any penalty for failing to comply with a collection of information if it does not display a currently valid OMB control number. **PLEASE DO NOT RETURN YOUR FORM TO THE ABOVE ADDRESS.**

1. REPORT DATE (DD-MM-YYYY) 18-08-2008		2. REPORT TYPE Final		3. DATES COVERED (From - To) 01-02-2005 to 31-01-2008	
4. TITLE AND SUBTITLE Integrated Analysis Tools for Determination of Structural Integrity and Durability of High Temperature Polymer Matrix Composites				5a. CONTRACT NUMBER	
				5b. GRANT NUMBER FA9550-05-1-0101	
				5c. PROGRAM ELEMENT NUMBER	
6. AUTHOR(S) Dillon, Gregory P.				5d. PROJECT NUMBER	
				5e. TASK NUMBER	
				5f. WORK UNIT NUMBER	
7. PERFORMING ORGANIZATION NAME(S) AND ADDRESS(ES) Pennsylvania State University 110 Technology Center University Park, PA 16802 Stevens Institute Of Technology Castle Point on Hudson Hoboken, NJ 07030				8. PERFORMING ORGANIZATION REPORT NUMBER AFOSR-GPD-8-18-2008	
9. SPONSORING / MONITORING AGENCY NAME(S) AND ADDRESS(ES) AFOSR/NL 875 Randolph Street Suite 325, Room 3112 Arlington, VA 22203-1954				10. SPONSOR/MONITOR'S ACRONYM(S) AFOSR	
				11. SPONSOR/MONITOR'S REPORT NUMBER(S)	
12. DISTRIBUTION / AVAILABILITY STATEMENT Unrestricted					
13. SUPPLEMENTARY NOTES					
14. ABSTRACT This report outlines an approach to reducing implementation cycle time for high temperature polymer matrix composites (PMCs) using integrated high fidelity physical models in preference to exhaustive experimentation and testing. The fundamental mechanisms of thermo-oxidative degradation of high temperature PMCs were studied and a three dimensional finite element modeling approach was developed that represents degradation, aging and oxidation effects. The effect of composite microstructure on damage development mechanisms was also explored using the finite element method. Digital Image Correlation was used to measure local (fiber level) stress and strain profiles in composites subjected to complex (bending) load conditions. Statistical analysis methods were also developed that may allow the relationship between composite architecture and variability in performance to be determined from measurable material attributes rather than large test databases.					
15. SUBJECT TERMS High Temperature Composites, Thermo-Oxidative Degradation, Durability, Polymer Matrix Composites					
16. SECURITY CLASSIFICATION OF:			17. LIMITATION OF ABSTRACT U	18. NUMBER OF PAGES 109	19a. NAME OF RESPONSIBLE PERSON Gregory P. Dillon
a. REPORT U	b. ABSTRACT U	c. THIS PAGE U			19b. TELEPHONE NUMBER (include area code) (814) 865-5879

Performance Report

**Integrated Analysis Tools for Determination of
Structural Integrity and Durability of High
Temperature Polymer Matrix Composites**

Principal Investigator: Dr. Gregory P Dillon

**Composite Materials Division
Applied Research Laboratory
The Pennsylvania State University
110 Technology Center
University Park, PA 16802**

For Period: 1 February 2005 to January 31 2008

Agreement Number: FA9550-05-1-0101

Report Covers Work Performed by;

**Penn State University
Air Force Materials Laboratory
Stevens Institute of Technology
The Boeing Company**

20090723686

Table of Contents

	Page
List of Figures	ii
List of Tables	vii
1.0 Program Objectives and Approach	1
2.0 Engineering Focus Areas	3
3.0 Team Members and Specific Roles	3
4.0 Executive Summary	5
5.0 Accomplishments & Findings	10
5.1 Fundamental Thermo-oxidative Mechanisms in Polymeric Materials	10
5.1.1 Anisotropy of Oxidation /Surface Dependent Oxidation Rates	10
5.1.2 Weight Loss Predictions	11
5.1.3 Accelerated Aging	17
5.2 Modeling Micro-Structure Evolution in Thermo-Oxidative Environments	19
5.2.1 Sorption and Diffusion Modeling	19
5.2.1.1 Heterogeneity in Diffusivity	20
5.2.2 Reaction Modeling	20
5.2.3 Oxidation Layer Growth Modeling	22
5.2.3.1 Active Oxidation Layer Size	22
5.2.3.2 Reaction Termination Criterion	22
5.2.4 Determination of ϕ_{ox} from Weight Loss Experimentation	24
5.2.5 Modeling of Accelerated Aging of High Temperature Polymers	25
5.2.5.1 Simulation of Arrhenius Temperature Dependence	25
5.2.5.2 Influence of Pressure on Oxidation Growth	25
5.2.7 Three-Dimension Finite Element Model	27
5.2.7.1 Extension of Oxidation Growth Prediction to Representative Volume Elements	27
5.2.7.2 Oxidative Aging of Unidirectional Composites	28
5.2.7.3 Composite Oxidation Studies with Representative Volume Elements	33
5.2.7.4 Modeling Oxidation Induced Stress and Deformation	27
5.2.8 Thermo-oxidative Aging of Carbon Fibers	40
5.2.8.1 Fiber Weight Loss Studies	40
5.2.8.2 Fiber Mechanical Properties	41
5.2.8.3 Fiber Surface Characterization	42
5.2.9 Monitoring of Oxidation Induced Fiber/Matrix Debond Propagation	43
5.2.10 Validation of Nanoindentation Measurements for Non Flat Surfaces	45
5.3 Determination of Fiber Architecture Effects on Crack Development	47
5.3.1 Automated Finite Element Analysis	48
5.3.2 Strain Mapping Using Digital Image Correlation	61
5.3.2.1 Fundamentals of Digital Image Correlation	61

5.3.2.2	Model System: Materials and Experimental Methods	63
5.3.2.2.1	Material Processing and Microstructure	63
5.3.2.2.2	Specimen Geometry and Mechanical Testing Procedures	64
5.3.2.2.3	Mechanical Testing System	64
5.3.2.2.4	Data and Image Analysis Methods	65
5.3.2.2.5	Mechanical Testing Results and Discussion	67
5.3.2.3	Composite System: Materials and Methods	69
5.3.2.4	Composite System: Low Magnification Results and Discussion	72
5.3.2.5	Composite System: High Magnification Results and Discussion	75
5.3.2.6	Composite System: Fracture Results and Discussion	81
5.4	Statistical Analysis	83
5.4.1	Basic Methods	83
5.4.2	Multivariate Characterization of Microstructures	87
5.4.3	Statistical Correlation with Measured Data	90
6.0	Concluding Remarks	91
7.0	Personnel Supported	94
8.0	Publications	95
9.0	Interactions/Transitions	97
9.1	Presentations at Conferences/Meetings	98
9.2	Consultative and Advisory Functions to Other Laboratories and Agencies	99
9.3	Technology Transitions	99
10.0	New Discoveries, Inventions, or Patent Disclosures	99
11.0	Honors/Awards	99
12.0	References	100

List of Figures

Figure 1	Oxidation after (a) 197 hours and (b) 1,200 hours for unidirectional G30-500/PMR015 composite exposed at 288°C	11
Figure 2	Weight loss parameters based on specimens with 3.3 and 8.2 surface area ratio	12
Figure 3	Weight loss prediction for specimens with 11.2 and 19.1 area ratios based on 3.3 and 8.2 area ratio specimen data	12
Figure 4	The weight loss rate function f_A as a function of aging temperature	15
Figure 5	Weight loss rate function as a function of aging temperature	15
Figure 6	Weight loss rate functions and based on T-3 and T-12 specimen data used to predict T-5 weight loss history at 204°C for aging times over 25000 hours. Based on experimental data from Bowles et.al.	16
Figure 7	Weight loss rate functions and based on T-5 and T-50 specimen data used to predict T-3 and T-12 weight loss history at 316°C for aging times over 1700 hours. Based on experimental data from Bowles et.al.	16
Figure 8	Influence of (a) temperature and (b) pressure on oxidation layer thickness in PMR-15 resin as a function of aging time	18
Figure 9	Influence of (a) temperature and (b) pressure on oxidation layer growth rate in PMR-15 resin as a function of aging time	19
Figure 10	Typical model of reaction rate dependence on concentration	21
Figure 11	Active reaction zone variation with time illustrating slowing of the oxidation reaction after 40 hours of aging	22
Figure 12	Schematic of the three-zones in thermo-oxidation. The oxidized region is followed by active zone separating the oxidized and unoxidized regions	23
Figure 13	Geometry of the specimen used for aging with all boundaries exposed to oxygen. The oxidized layer, active reaction zone and the unoxidized regions are illustrated in the sectional view	24
Figure 14	Prediction of oxidation thickness at 316°C and 343°C based on 288°C model parameters	26
Figure 15	Influence of sorption on the oxidation layer thickness	26
Figure 16	Prediction of oxidation thickness for pressurized aging of PMR-15	27
Figure 17	Typical unit cells used in the FEA analysis. (a) without an interphase region and (b) with an interphase region	27
Figure 18	Unit cells for modeling (a) axial oxidation, (b) transverse oxidation, and (c) the influence of interphase on oxidation growth in a unidirectional composite	29
Figure 19	Simulations of oxidation growth in axial direction at (a) 50 hrs, (b) 100 hrs, (c) 150 hrs, and (d) 200 hrs of exposure	30
Figure 20	Effect of fiber diffusivity on matrix oxidation	30
Figure 21	Transverse oxidation growth in a composite lamina	31
Figure 22	Detail of active reaction zone from transverse simulation	31
Figure 23	Transverse vs. axial oxidation depth in a unidirectional composite	32
Figure 24	Oxidation layer size variation with interface diffusivity	33
Figure 25	Effect of fiber diffusivity on composite oxidation	34

Figure 26	Effect of a highly diffusive fiber-matrix interphase region. The anisotropy in the oxidation layer can be clearly seen	36
Figure 27	Figure 27 (a)-(d): Oxidation state and effective stress distributions after 10 hours of oxidative aging	39
Figure 28	Weight loss of T650-35 carbon fiber as a function of aging temperature	41
Figure 29	Normalized weight loss of T650-35 fiber and PMR-15 resin	41
Figure 30	Normalized strength of unsized T650-35 carbon fibers aged at 343°C	42
Figure 31	Normalized failure strain of unsized T650-35 fibers aged 343°C	42
Figure 32	SEMs showing surface morphology of unsized T650-35 carbon fibers in (a) the unaged condition, (b) aged for 1052 hours at 343°C	42
Figure 33	Cross section of 96-hr aged specimen	44
Figure 34	Cross section of 668-hr aged specimen	44
Figure 35	Cross section of 2584-hr aged specimen	45
Figure 36	3D image of the 1556hr aged PMR-15 specimen	46
Figure 37	2-D image of a 1556 hr aged PMR-15 sample	47
Figure 38	Central ply of a (0/90)2S laminate tested to onset of microcracking	48
Figure 39	Fiber centers and associated Voronoi cells for laminate shown in Figure 38	49
Figure 40	Fiber volume fraction map for micro-cracked composite laminate made from YLA material	49
Figure 41	Fiber volume fraction map showing gradient plot across a selected horizontal line	50
Figure 42	Fiber centers as transferred to FEA Mesh Generator	50
Figure 43	Voronoi Cell Tessellation as calculated by FEA Mesh Generator	51
Figure 44	Sample FEA mesh, as generated by automated FEA mesher	52
Figure 45	FEA model, predicted strain, uniform edge load at right side of specimen	53
Figure 46	FEA model, predicted stress, uniform edge load at right side of specimen	54
Figure 47	FEA model, predicted displacement, uniform edge load applied at right side of specimen	54
Figure 48	Mode I crack development in homogenous isotropic material subjected to a boundary crack opening displacement.	56
Figure 49	Internal crack propagation in two directions with adaptive meshing	56
Figure 50	Flow chart of iterative adaptive meshing algorithm	58
Figure 51	Comparison of predicted crack propagation mechanisms with and without adaptive meshing	59
Figure 52	Comparison of predicted crack propagation mechanisms with and without adaptive meshing for a shear loaded crack	59
Figure 53	Application of adaptive meshing algorithm to mesh generated using voronoi cells from a real composite microstructure	60
Figure 54	Application of adaptive meshing algorithm to mesh generated using voronoi cells from a real composite microstructure	60
Figure 55	Tensile test of specimen 1 initially loaded to 1 N (234 MPa)	67
Figure 56	DIC tensile test of specimen 2 initially loaded to 1 N (234 MPa)	68

Figure 57	Comparison of strain data generated by crosshead displacement (2ed56 Crosshead and DC 208 Crosshead) to strain data generated by DIC (2ed56 DIC and DC 208 DIC).	69
Figure 58	Photograph of the mechanical testing and strain measurement system	70
Figure 59	Schematic depiction of the composite specimen and the analysis regions.	71
Figure 60	Typical mechanical test of a composite laminate in the Penn State system.	71
Figure 61	Average longitudinal and transverse strains measured in the composite during the flexure test	72
Figure 62	Optical micrograph of the [(0/90) ₂]s laminate surfaces at a higher magnification (50× objective lens) at the start (423 MPa) and end (674 MPa) of a linear ramp test under load control	73
Figure 63	Longitudinal and transverse strains measured during a linear ramp from 423 MPa to 674 MPa.	73
Figure 64	Spatial distribution of strains in a laminate composite	74
Figure 65	High resolution digital images of fibers and the various grid arrays that were used for strain mapping	74
Figure 66	Evolution of strains in the central portion of the outer, tensile ply of the composite and a schematic of the location of the measurement	76
Figure 67	High resolution strain maps from the central portion of the outer, tensile ply of the composite.	76
Figure 68	Evolution of strains in the [0/90] interface portion of the outer, tensile ply of the composite and a schematic of the location of the measurement	77
Figure 69	High resolution strain maps from the [0/90] interface portion of the outer, tensile ply of the composite. Large tensile strains oriented along the ply interface were observed	77
Figure 70	Evolution of strains in the neutral axis region of the composite and a schematic of the location of the measurement	79
Figure 71	High resolution strain maps from the neutral axis portion of the composite	79
Figure 72	Evolution of strains in the compressive axis region of the composite and a schematic of the location of the measurement	80
Figure 73	High resolution strain maps from the compressive axis portion of the composite.	81
Figure 74	Cracking in the outer (tensile) ply of the composite	82
Figure 75	Evolution of strains during reloading of the cracked composite (without crack extension)	82
Figure 76	High resolution strain maps from the cracked portion of the composite	83
Figure 77	Cumulative Distribution Function and Probability Density Function data for Fiber Area Fraction in Sample Microstructure	84
Figure 78	Micrographs of uncured graphite epoxy prepreg material and laminate fabricated by conventional autoclave processing	84
Figure 79	Fiber volume fraction maps for uncured prepreg and laminate micrographs shown in Figure 78	85

Figure 80	Example of output from automated image analysis tool being used to generate statistical data	85
Figure 81	Fiber volume fraction plots of >500 fibers for prepreg (left) and cured laminate	86
Figure 82	Probability density function of fiber volume fraction for plots shown in Figure 81	87
Figure 83	Portion of the output for the variable, "50 longest runs at 0°, 45°, 90°, and 135°"	88
Figure 84	Delaunay triangulation analysis for the white circled cell, showing successive layers of neighboring cells	88
Figure 85	A microcrack located in a composite microstructure along with neighboring fibers	91
Figure 86	Levels at which modeling effort was devoted in an effort to provide for a fully integrated predictive capability	92

List of Tables

Table 1	Specimen configurations	12
Table 2	Specimen configurations from Bowles et.al.	14
Table 3	Constants for evaluating diffusivity of polyimide resin	20
Table 4	Anisotropy in composite diffusivity and its correlation with oxidation layer size	35
Table 5	Total volumetric shrinkage observed for PMR-15 at elevated temperatures	38
Table 6	Atomic percent of elemental impurities in electrodeposited nickel specimens	63

1.0 Program Objective and Approach

Military platform system performance is frequently limited by material capabilities. Often, viable material options exist, but conservativeness on the part of designers leads to an involved, time consuming, and test intensive implementation cycle. Efforts such as the Materials Engineering for Affordable New Systems (MEANS) initiative and the Accelerated Insertion of Materials – Composites (AIM-C) programs sought to shorten the duration and decrease the costs for the materials transition process. The development of a design methodology based on high fidelity modeling with strategic experimentation is the key to inserting new and innovative materials into aerospace applications. A hierarchy of models for predicting behavior from the constituent level up to the structure level, coupled with advanced statistical methods, will enable rapid and cost effective generation of design allowables. Once this design methodology has been established, validated, and instituted, the development of materials and processes that optimize performance and life expectancy can facilitate advancements in aircraft design and operational limits.

Polymeric Matrix Composite (PMC) materials have provided great benefit to military platforms, primarily in aerospace structures. High specific strength and stiffness, multi-directional property tailorability and corrosion resistance are among the many advantages offered by these material systems. Over the last decade there has been an intensification of effort in the development of higher temperature polymer matrix systems, spurred by a well founded desire to exploit the structural efficiencies afforded by these materials in applications that are closer to heat sources. Engine components and exhaust washed surfaces have traditionally been made from metallic and ceramic materials that may not offer all of the varied benefits of composites.

The principal challenges confronting the implementation of High Temperature Polymer Matrix Composites (HTPMC) include the development of polymer systems that are thermally stable at high temperatures, and the need to provide such materials with viable processing characteristics. Nonetheless, recent advances suggest that application temperatures up to 650°F and beyond may well be feasible. The major impediments to rapid transition of these systems are, as with most advanced materials, the lack of an analytical capability to predict key performance attributes in application environments of interest and attendant uncertainty in key design parameters. The objective of the work described in this report was to develop a materials qualification approach based on a combinatorial multi-scale modeling and optimization methodology for reduced qualification testing to obviate the need for exhaustive testing of HTPMCs in simulated service environments during the materials qualification process.

The approach adopted was designed to enable a more efficient insertion of HTPMCs in terms of time, cost, and performance, into Air Force systems. The approach involved three major features:

- Incorporating polymer processing and degradation models into selective micromechanic, mesomechanics, and laminate models to predict environmental performance of polymer matrix composites.
- The use of high fidelity polymer material models to enable a minimum number of strategic tests for materials characterization vs. the current "empirical" approach, which is based on accumulating statistics from large test programs.
- Development of a model-based design methodology for composite materials, which allows for populating the Design Allowables Database while maintaining the fidelity of the current empirically based database.
- Development and application of new and more powerful experimental techniques that yield fundamental material properties as a foundation of the design database
- Identification of efficient statistical analysis techniques that may relate fundamental material structure attributes to variations in performance

These features can effect a reduction in the time and cost (and potentially a reduction in structural weight) required for insertion of new polymer composites into critical Air Force applications.

The basis of this MEANS approach is analyses with the proper level of fidelity coupled with strategic/intelligent testing. Most analytical tools currently used in material qualification ignore explicit phase representations and microstructural features of the material. Features of the material response that can be readily described using the natural primitive material variables (i.e. ones that acknowledge the appropriate scale) in concert with high fidelity models can capture critical performance information not achievable with cruder models. Methodologies that employ the lower fidelity models require a significant number of experiments to statistically characterize the material, leading to proportionate increases in the cost and time for insertion. The use of high fidelity models enables the various inputs for the materials qualification database, wherein models/experiments at the various geometric scales can interact, to be assembled.

The three features of the approach as described above directly address the key impediments in the current materials qualification methodology. Firstly, computer models with the appropriate level of fidelity will substantially reduce the exhaustive experimental testing and associated time required for qualification of new materials. Secondly, tools and approaches can be targeted to provide the material supplier with a more efficient way to optimize the material for a particular application. It is believed that implementation of this methodology will facilitate the achievement of the MEANS objective of significantly reducing the testing (cost and time) required for insertion of new materials into mission critical Air Force applications.

Recent focus on the development of polymer matrix materials for high temperature applications has forced a new emphasis on analytical descriptions of material behavior, particularly in terms of long-term durability in thermo-oxidative environments. In order to foster efficient generation of a designer knowledge base, a multi-disciplinary research team was assembled, with the central focus of maturing and integrating material models and analysis tools to provide a reliable lifetime prediction of performance for HTPMCs.

This Integrated Materials Design Team (IMDT) composed of The Pennsylvania State University, Stevens Institute of Technology, Air Force Research Laboratory, and The Boeing Company addressed aspects of structural integrity and durability of HTPMCs. The ultimate goal of the program was to provide a predictive methodology that will allow the elevated temperature performance of composite systems to be determined based on constituent properties and processing environment. The models, protocols and procedures devised are believed to be sufficiently broad ranging to allow key performance metrics of new systems to be predicted, without recourse to exhaustive materials coupon testing.

2.0 Engineering Focus Areas

Awards made under the MEANS II initiative were structured to provide benefit in specific Engineering Focus Areas (EFA). The IMDT described above elected to direct this initiative to Airframe Structures, though the models and methodologies developed are believed to have equal applicability to HTPMCs in Propulsion Systems. Achievement of the program goals was required effort in a number of Research Concentration Areas, as follows:

- i. Degradation Kinetics and Polymer Mechanics: As composite system durability depends on the constituent (fiber and matrix) durability, considerable effort was devoted to the modeling and characterization of resins and fibers under long-term environmental exposure
- ii. Interface and Micromechanics: The fiber-matrix interface behavior is critical in determining the composite behavior. The structure and properties of the fiber-matrix interface region are a result of the composite manufacturing process and were therefore investigated.
- iii. Meso and Structural: The structure and distribution of the fiber phase has a critical effect on composite performance and, perhaps more importantly, variation in material attributes. It was therefore considered important to consider reinforcement materials in a statistical sense to create a high fidelity representation of the microstructure. The designers of air frames work on the materials and life predictions at the structural (laminate) scale. Homogenization approaches and effective long-term behavior prediction, including long-term thermo-oxidative and visco-elastic behavior, were critical research focus areas for this IMDT.

It is considered important that each of the IMDT members had significant expertise in several of these research concentration areas which overlap and are interdisciplinary in nature.

3.0 Team Members and Specific Roles

The IMDT members had specific experience and capability in lifetime prediction of HTPMCs. Modeling initiatives that addressed critical issues relating to matrix performance, fiber architecture variability and interface development were already underway at program outset. In addition The Boeing Company provided the potential for

access to the AIM-C multi-scale modeling hierarchy, through which the pertinent models could be integrated. Boeing also provided critical access to the airframe design community and this allowed the model development and methodology implementation initiatives to be guided from the perspective of established practice. The IMDT team members and their roles are summarized below:

- AFRL/ML: Work at AFRL/ML was focused on modeling the mechanisms that control the oxidative and physical aging processes of PMCs. Fundamental mechanisms of oxide growth were uncovered and the relative contributions from free surface and crack assisted penetration of oxide layers were successfully described. AFRL/ML led the Degradation Kinetics and Polymer Mechanics activities.
- Stevens Institute of Technology: Stevens led an activity aimed at generalizing the degradation behavior of polymer matrix composites by integrating models that described the three major mechanisms that drive age-related degradation of the polymeric matrix composite materials. Stevens collaborated closely with AFRL/ML on the kinetics and mechanics activity. Stevens also led the lamina scale degradation modeling.
- Pennsylvania State University: Penn State developed rapid microstructure characterization techniques that allowed the impact of material variability, resulting from prepreg process variation and subsequent component fabrication effects, on structural performance to be determined. Penn state led the Meso and Structural Mechanics Tasks as well and also collaborated with Stevens and AFRL on integration of modeling initiatives.
- Boeing Corporation: The final critical element of the program team was The Boeing Company, who provide guidance on selection of demonstration platforms for developed models and brought accumulated experiences on model integration in the DARPA AIM-C program to bear on the project.

Program award occurred on February 1st 2005 as a grant to Pennsylvania State University with subcontracts to Stevens Institute of Technology and The Boeing Company. The former was negotiated relatively quickly, though contractual issues prevented full participation of the Boeing Company until late in the first year of the program. Special clauses had to be incorporated into the agreement relating to liability and data exchange and an exception to normal procedure was procured from upper Boeing management to allow the work to be performed without imposition of the customary fee. While this caused an unintended delay in Boeing's participation significant progress on basic model development was achieved and therefore subsequent interactions with the Boeing Company were more beneficial.

The Air Force Research Laboratory was not a direct subcontractor to Penn State University in this program, but was an integrated team member. Therefore progress due to AFRL was included in this report and is submitted in fulfillment of their reporting requirements.

4.0 Executive Summary

The program team collaborated on several model development and experimentation initiatives as the project proceeded. However the first year of work was focused on establishing the general foundations in the focus areas described in Section 3. Therefore this early phase of the work necessarily involved independent activity at the individual research centers. As these elements of a design database development methodology were assembled the program gradually migrated to the collaborative activities anticipated at the beginning of the program.

The early program focus of AFRL/ML was in three principal areas i.e. characterization of the anisotropy of oxidation and surface dependant oxidation of composites, weight loss prediction and design of accelerated aging techniques. In the first year of the program AFRL/ML used X-ray Photoelectron Spectroscopy to track oxidation layer depth in neat polymer samples of AFR-PE-4 resin. By tracking either the oxygen or fluorine concentration it was shown to be possible to achieve accurate correlations with experimental data. Further experiments carried out on G30-500/PMR 15 composites showed that the rate of oxidation layer growth along the axis of fibers is much greater than in the transverse direction and a weight loss prediction model that accounts for the ratio of exposed fiber end surfaces to transverse surfaces was developed and shown to accurately correlate with experimental data for a wide range of sample geometries. In the first year, effort was also devoted to the identification and development of accelerated aging techniques that would allow determination of long term oxidative degradation effects to be achieved in timescales that are significantly shorter than anticipated platform life. However temperature dependant aging mechanisms limit the usefulness of elevated temperature aging. Elevated pressures were shown to increase degradation rates, and acceleration techniques based on this expedient were further evaluated in Year 2.

In the second year of the program AFRL/ML performed three-dimensional oxidation modeling by finite element analysis (FEA) on micromechanical representations of unidirectional composite using the previously developed diffusion/reaction model for the neat resin developed in Year 1 and a unit cell representation of the composite. Micromechanics models described the geometry of the constituents, volume fraction, and orientation in the composite, while the models allowed multi-fiber and multi-cell simulations to be performed. Assuming idealized bonding of fiber and matrix through the interphase, prediction of oxidation propagation along the fiber direction is less than the experimentally observed extent of oxidation indicating that the diffusion of oxygen in the fiber direction is not fully accounted for. Parametric studies, in which the diffusivity of the interphase and fiber were varied, showed that the diffusivity of the interphase has little effect on the effective unit cell diffusivity. This is due to the fact that the interphase only makes up a tiny volume percentage of the unit cell. Furthermore, the diffusivity of the fiber would have to be on the order of, or greater than, neat resin diffusivity to significantly influence the effective unit cell diffusivity. Unfortunately, measurements of the interphase diffusivity and the orthotropic diffusivity of the carbon fibers were not accomplished. If the ratio of the transverse to axial oxidation growth is assumed to be proportional to the ratio of the transverse to axial diffusivity for unidirectional

composites, the study showed that the high rate of axial oxidation growth can not be properly accounted for by considering diffusion of oxygen alone. However, initial modeling indicated that the differences between the axial and transverse diffusivities can be accounted for by modeling the fiber/interphase/matrix debond that provides a pathway for oxygen to propagate deeper into the composite. Experimental evidence showing that the fiber/matrix debond propagates with the axial oxidation front was collected.

Durability and degradation mechanisms in composites are fundamentally influenced by the fiber, matrix, and interphase regions that constitute the composite domain and the effects of these material features on thermo-oxidative stability were studied in detail, primarily in a close collaboration between AFRL/ML and Stevens Institute of Technology. The thermo-oxidative behavior of the composite is significantly different from that of the constituents as the composite microstructure introduces anisotropy in the diffusion behavior as well as many fiber/matrix interphases/interfaces. Unidirectional G30-500/PMR-15 composite specimens were aged at elevated temperatures in air resulting in oxidation propagation parallel and perpendicular to the fibers as described above. These experimental observations were compared with micro-structural based kinetic models to evaluate the oxidation behavior of unidirectional composites. It was determined that the interface has a dominant effect on the propagation of oxidative degradation. Quantification of the effect of fiber-matrix interface diffusivity on the effective composite diffusivity was attempted.

Since the use temperature of HTPMCs is often near the glass transition temperature of the material, the ability to accelerate aging by increasing the temperature is limited. The use of pressure to accelerate the oxidative aging process is used in the aircraft engine community based in part on the fact that engine parts experience elevated pressures during use. Although the oxidation mechanisms in HTPMCs are not fully understood some of the functional relationships that govern aging, can be determined. For example, the acceleration of aging due to increased pressure would be a result of increased transport of the oxygen to the interior of the specimen. The effect of elevated pressure on the oxidation layer growth in neat resin PMR-15 samples was successfully modeled in Year 2. Since the partial pressure of a gas is directly proportional to the total pressure at which specimens are aged, and in general the solubility of gases increases with increasing pressure, the boundary sorption would be expected to increase with increasing pressure. A parametric study was conducted and it was found that for the sorption value, there is a good correlation with the pressurized aging data for aging times up to 800 hours. Validation of the constituent level response to elevated pressure provides confidence in using the neat resin model in unit cell analysis to predict the lamina response to elevated pressure.

In the concluding phase of the program AFRL/ML focused on monitoring of oxidation induced fiber/matrix de-bond propagation. The oxidation process is generally limited by the amount of oxygen that can diffuse into the material and react with the polymer, rather than by the rate of reaction of oxygen with the polymer. The diffusion limited oxidation behavior of polymer matrix composites is predominantly controlled by the properties of the resin and the fiber-matrix interface and the total surface area through which the

oxygen can diffuse. Various factors may lead to the preferential oxidation along the fiber paths. Resin cure shrinkage and mismatches in the coefficient of thermal expansion of the fibers and matrix during the composite cure process give rise to localized micromechanical residual stresses in the fiber-matrix interphase region. In the final year, optical micrographs were taken on polished internal sections and viewed in the dark-field mode to measure the degree, depth and distribution of thermal oxidation development from external surfaces perpendicular and parallel to the fibers. It was shown that alternative pathways for transport of oxygen into the interior of the composite were provided by fiber-matrix de-bonds that propagate with the oxidation front, with the oxidation front consistently preceding the debond crack front. This finding emphasized the importance of understanding the impact of fiber architecture on matrix crack development, which was a primary focus at Penn State University.

Stevens Institute of Technology initiated an activity aimed at formulating a generalized description of the degradation behavior of polymer matrix composites in Year 1, by developing a model of the thermo-oxidative process for polymer systems, that incorporated the effects of reaction rates, Fickian diffusion, time varying concentration gradients, consumption of reactants (solid and gas phases), and weight loss from a system under degradation. The model was shown to correlate well with experimental oxidation layer growth at various exposure temperatures, and a sensitivity study was performed to identify the parameters that have greatest effect on degradation system kinetics. The model was incorporated into a finite element description of a representative element of a fiber composite and the resultant simulations were shown to realistically represent the impact of multiple phases on degradation processes. In close collaboration with AFRL/ML, Stevens Institute of Technology extended the modeling activity in Year 2 to consider creep deformation, in an analysis that attempted to couple these effects with the degradation modeling.

In the final year of the program Stevens Institute of Technology continued activity in two main modeling thrust areas. First thrust area was the evolution of the framework needed to simulate the orthotropic oxidation growth in fiber reinforced composites. At this stage the thermo-oxidative behavior of the composite was shown to be significantly different from that of the constituents as the composite microstructure, including the fiber/matrix interphase/interface, introduces anisotropy in the diffusion and oxidation behavior. Unit cell analyses were continued using three-dimensional finite element analysis of repeated volume elements representing the fiber, matrix and interphase regions, and the previously developed resin oxidation model. Parametric studies illustrating the anisotropy in the oxidative region growth and the effect of fiber and interphase diffusivity on the oxidation layer growth were considered. It was suggested that fiber-matrix debonding could provide additional diffusion paths to explain the extent of observed anisotropic oxidation growth. The second thrust area focused on simulating the development of stresses and deformations. Three-dimensional Galerkin finite element methods (GFEM) that model the thermo-oxidative layer growth with time were used together with homogenization techniques to analyze lamina-scale behavior using representative volume elements (RVEs). Thermo-oxidation-induced shrinkage was characterized from dimensional changes observed during aging in inert (argon) and oxidative (air) environments.

Temperature-dependent macro-scale (bulk) mechanical testing and nano-indentation techniques were used for characterizing the effect of oxidative aging on modulus evolution. The stress and deformation fields in a single ply unidirectional lamina were studied using coupled oxidation evolution and non-linear elastic deformation analyses. Deformation and stress states were determined as a function of the aging time. While the thermo-oxidative processes are controlled by diffusion phenomena in neat resin, the onset and propagation of damage determines the oxidative response of an HTPMC.

In the first year of the program Penn State University used an automated image analysis tool, developed under prior AFOSR funding, to form the basis of an Automated Finite Element grid generation code that facilitates the determination of fiber architecture influences on micro-crack generation. This predictive capability allowed the effects of crack patterns on thermo oxidative degradation mechanisms to be determined and vice versa. Also in the first year Penn State began to evaluate a new Digital Image Correlation (DIC) technique for application to the measurement of micro stress and strain profiles in composites at various length scales and it was thought that this work would provide for scale appropriate calibration of the predictive tools described above. Statistical analysis techniques were also sought to allow the impact of normal material variability on associated variance in critical design performance parameters to be determined. Automated image analysis combined with advanced statistical techniques was expected to provide a means of correlating material architectural features with test data.

In Year 2 of the program Penn State University continued progress in the first two areas mentioned above i.e. automated structural analysis of composite microstructures and non contact strain mapping using Digital Image Correlation. Initial work had shown that use of finite element grids based on Voronoi Cell Analyses to predict crack initiation and propagation was limited by the fact that local grid configurations influenced the predicted direction. An adaptive meshing algorithm was therefore developed that overcame this problem. Software coded in the second year automatically refines and reorients the grid in the region close to the crack tip so that crack propagation is seen to occur along planes and directions suggested by strain energy release rate analyses. This development was seen as very significant as it provided the final component of an FEA analysis tool suite that allows the effect of fiber architecture variations on damage development to be determined in a completely automated fashion. While adaptive meshing techniques had been developed in other programs, none were available that were uniquely suited to efficient modeling of crack development and propagation mechanisms at this refined scale

In the second year of the program a number of technical problems were solved to allow the DIC technique to be applied to mechanical testing of composites. For example the method was successfully applied to provide the first known strain maps for composites under load. These initial maps allowed the strain fields to be determined for length scales on the order of those associated with fiber bundles or tows. In the later months of the second year DIC was further refined to allow measurement at the fundamental length scale of the individual fiber. This provided a critical check or calibration for the

Automated FEA (described above) as well as furnishing insight into stress redistribution mechanisms around propagating cracks. This development is considered very significant as it provides the capability to perform scale appropriate testing of composite materials to determine fundamental material mechanisms associated with progressive failure.

In the final year of the program the capability of the Digital Image Correlation tool was further enhanced by refining the grid generation scheme, on which the strain maps was based, to allow for more accurate delineation between strain and stress patterns developed within the fiber and resin phases. Versions developed in Years 1 and 2 provided strain maps that were essentially smeared across fibers and matrix. In the final Year a scheme was developed that allowed the original grid to be placed exactly at the fiber/matrix interface and this facility allowed the critical parameter of interface load transfer to be studied at a level of detail hitherto impractical.

The automated FEA tool was further refined in the last year of the program and was used to interrogate some of the stress and strain distributions measured using the Digital Image Correlation technique. Broad agreement between measured and predicted patterns was seen to exist, though some non-intuitive effects seen in the former were not successfully represented. For instance, one surprising result from the DIC measurements suggested that local compressive stresses could be generated in regions where the global stress was tensile. While the broad variability in local stress generated by far field loads was seen in the FEA analyses, the sense reversal was not predicted. It was suspected that this was due to three dimensional and/or edge effects that were not captured in the 2.5 D FEA analysis.

Also in the final year of the program Penn State University developed several computational tools to allow the application of Multivariate Discriminant Analysis (MVA) to the identification of statistical features in real fiber packing arrangements that may influence variability in resultant structural (or other) performance. The fundamental basis of this approach is the capture of a broad range of candidate packing factors, such as fiber spacing, local fiber volume fractions, material alignments etc., and attempt to relate them to each other (to uncover self consistent parameters or 'factors') and then to some performance metric, such as propensity to micro-cracking. If the factors are then seen to scale with some measureable quantity, such as crack density at a given load level, a predictive capability results that allows variability to be predicted as a function of architectural features. A software code was developed that allows automatic capture of approximately 200 user defined packing factors. However full application of this method was not achieved prior to contract expiry.

The involvement of the Boeing Company essentially remained the same throughout the program duration. Periodically the Boeing Team was briefed on the progress of the model development activities and suggestions on future direction were routinely provided. In the final Year of the program Boeing hosted a program review in the St. Louis facility in November 2007, with a focus on assessment of the program activity and recommendations for future work. A large amount of subcontracted funding (to Boeing) remained unexpended and a no-cost extension was informally requested to allow

completion of work assigned to Boeing. The no-cost extension could not be approved. However the feedback received at the St. Louis review provides a valuable template for potential future programs. Senior technical staff at Boeing, with broad experience on both airframe and engine programs, suggested that the modeling activities be expanded to consider the effects residual stresses on degradation and thermo-oxidative stability. They also pointed out that on prior programs, such as HSR/HSCT, interface phenomena were seen to be of great importance and urged future focus on using the tools developed in the MEANS II program to uncover the underlying effects.

In summary The MEANS II program has provided for the development of several tools that, if fully integrated, could form the basis of a new materials implementation protocol for high temperature systems. Comprehensive degradation models, allied with fundamental structural analyses and advanced statistical techniques could dramatically reduce the need for time consuming and expensive test programs and accelerate materials transition.

5.0 Accomplishments & Findings

Findings in the initial phase of the program were in the general areas of polymer degradation characterization and modeling, incorporation into composite modeling and prediction of microcrack patterns based on composite architecture, as described in the following sections.

5.1 Fundamental Thermo-oxidative Mechanisms in Polymeric Materials

Early in the program an initiative was undertaken to uncover the fundamental thermo-oxidative behavior of polymeric materials with a particular focus on high temperature systems as applied in composites. The influence of fiber orientation on oxidation propagation was studied in unidirectional laminates. A weight loss model was developed that described degradation as a function of characteristic specimen dimensions and aspect ratios. Since long exposure times are of particular interest in pertinent applications accelerated aging was also considered in the early stages of the research.

5.1.1 Anisotropy of Oxidation /Surface Dependent Oxidation Rates

Unidirectional 16 ply G30-500/PMR-15 composite specimens were aged in air at 288°C to monitor the oxidation propagation rates in both the axial direction (along the fiber) and the transverse direction (transverse to the fibers). Specimens were removed from the aging oven at specified times and a small cross-section of the specimen was cut off and mounted in an epoxy plug for polishing. The original specimen was then placed back into the oven until the next specified aging time. The 197-hour sample was found to contain evidence of only minimal oxidation transverse to the fibers, but had distinct oxidation development in the axial direction. Figure 1(a) shows an enhanced micrograph that clearly distinguishes the white oxidized material from the black unoxidized material.

The oxidation layer appears as a frame around the composite specimen just as seen in

aged neat resin PMR-15 samples [1]. Quantification of the overall level of oxidation was achieved by measuring the percentage of the specimen cross-sectional surface area that was oxidized. Using the constructed enhanced micrograph image, a histogram of the image was used to determine the ratio of white to black pixels and the ratio was used to quantify the amount of surface area of the composite cross-section that has been oxidized. Quantification of the oxidation area using this process is a 2D computation and does not account for stochastic variations of the oxidized cross-section through the thickness of the specimen.

Measurements of oxidation layer development were completed up to 2500 hrs of aging. Figure 1(b) shows the results of specimen oxidation at 1200 hours. It appears that the rate of oxidation growth in the axial direction is an order of magnitude greater than the rate of oxidation growth in the transverse direction. Figure 1 clearly shows the dominance of the axial oxidation degradation as compared to the transverse degradation in composites which is attributed to the higher diffusivity in the fiber-matrix interphase region. Thus, the presence of fibers accelerates the growth of the oxidized region along their length.

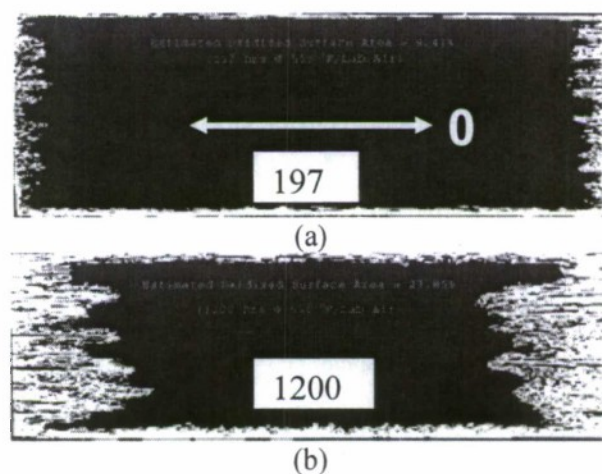


Figure 1 Oxidation after (a) 197 hours and (b) 1,200 hours for unidirectional G30-500/PMR015 composite exposed at 288°C

5.1.2 Weight Loss Predictions

The preferential diffusion and oxidation along the fiber matrix interphase regions leads to anisotropic oxidation in unidirectional composites. Likewise in woven cloth composites, the oxidation progresses more rapidly in directions normal to exposed fiber ends. The anisotropic nature of oxidation in high temperature polymer matrix composites has been observed by numerous investigators including the earlier work of Nam and Seferis [2] and Skontorp [3].

In this work 16 ply unidirectional G30-500 /PMR-15 composites with a Toho EPOI fiber sizing were isothermally aged at 288°C. Three different specimen configurations were chosen such that different surface area ratios of 3.3, 8.2, and 19.1 [i.e., ratios of surface

area parallel to the fibers (transverse) to surface area perpendicular (axial) to the fibers] were obtained while the overall surface areas of the three specimen geometries were all approximately 800 mm². A fourth specimen with a surface area ratio of 11.2 and a total surface area of approximately 1500 mm² was also chosen. Table 1 gives the axial surface area A_A , which is the surface normal to the exposed fiber ends, and the transverse surface area A_T , which is the surface transverse to the fiber axes for each of the four specimens. Specimens were aged in lab air (2 specimens for each configuration) at 288°C. Weight loss and volumetric changes were monitored as a function of aging time to study the high temperature anisotropic oxidation process.

Table 1. Specimen configurations

A_T / A_A	A_A (mm ²)	A_T (mm ²)	A_{total} (mm ²)
3.3	184.4	609.0	793.4
8.2	85.6	701.7	787.3
11.2	123.1	1381.0	1504.1
19.1	40.5	773.9	814.4

A primary measure of the thermal oxidative stability of PMR-15 and other high temperature composite materials is the percentage weight loss as a function of isothermal aging time and temperature. In general, the relationship between weight loss and property changes can be highly nonlinear and provides little measure of the spatial variability of degradation within the specimen. The reliability of predictive methods based on weight loss, in which small changes in weight can result in significant declines in mechanical properties, is highly questionable. However, in the absence of methods to predict end of life properties, weight loss is an accepted screening tool to compare the thermal oxidative stability (TOS) of different materials.

Bowles et al. [4] considered three different rates of weight loss from three different types of composite surfaces. The weight losses were expressed as weight-loss fluxes or weight loss per unit surface area per unit of time. Composite weight loss was determined as $weight\ loss = At^B + C$ where A is expressed as $A = S_1k_1 + S_2k_2 + S_3k_3$. In this expression: S_1 = Area of un-machined resin-rich surface; S_2 = Area of surface cut parallel to fibers; and S_3 = Area of surface cut perpendicular to fibers. Knowing A for the entire specimen, k_1 , k_2 , k_3 can be determined from 3 specimens [4]. For his weight loss data, he found that k_1 and k_2 are nearly equal which is what is assumed in Skontorp [3]. Although represented as being constant, Bowles admits that the fluxes change with time and concluded that short-term isothermal aging tests cannot be used to produce data for predicting long-term degradation.

Skontorp [3] approximated the total isothermal aging weight loss Δm_{total} of a unidirectional composite as

$$\Delta m_{total}(t) = \Delta m_A(t) \frac{A_A}{A_{total}} + \Delta m_T(t) \frac{A_T}{A_{total}} \quad (1)$$

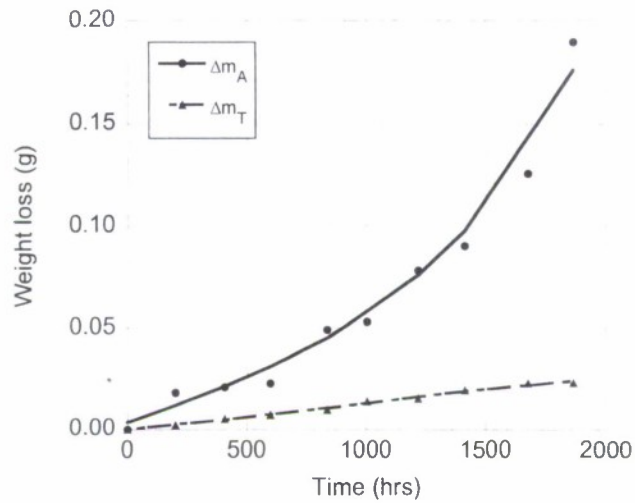


Figure 2 Weight loss parameters based on specimens with 3.3 and 8.2 surface area ratio

where the total surface area $A_{total} = A_A + A_T$, and the weight loss per unit of axial surface area Δm_A and the weight loss per unit of transverse surface area Δm_T are empirically determined parameters based on weight loss data from two specimens with different ratios of A_A/A_T but with equivalent A_{total} . This approximation has been shown to provide reasonable predictions of the weight loss of specimens over a limited range of transverse to axial surface area ratios for specimens with the same total surface area A_{total} .

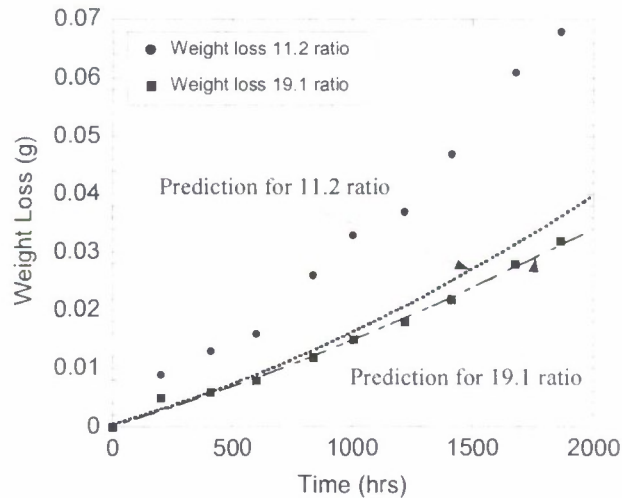


Figure 3 Weight loss prediction for specimens with 11.2 and 19.1 area ratios based on 3.3 and 8.2 area ratio specimen data

The weight loss per unit of axial surface area Δm_A and the weight loss per unit of transverse surface area Δm_T were determined using data from specimens with transverse to axial ratios of 3.3 and 8.2 as given in Table 1. As seen in Figure 2, whereas Δm_T is linear, Δm_A is highly nonlinear and an order of magnitude greater than Δm_T for longer aging times.

The prediction of the weight loss of the specimens with a 19.1 ratio of transverse to axial surface area is shown in Figure 3 and found to be in good agreement with the experimental weight loss data. Also in Figure 3 the weight loss for a fourth specimen with a surface area ratio of 11.2 and a total surface area 87 percent greater than the first three specimens was predicted and it did not scale according to Equation (1) due to a different total surface area.

A new relationship, based on time dependent weight loss rates is introduced. The total weight loss as in terms of weight loss per unit area is expressed as;

$$\Delta m_{total}(t) = f_A(t)A_A + f_T(t)A_T \quad (2)$$

where f_A is the time dependent weight loss per unit area of the axial surface area and f_T is the time dependent weight loss per unit area for the transverse surface area. Using this expression, the weight loss per unit areas f_A and f_T can be determined using two specimens with different total surface areas. These weight loss factors are both time and temperature dependent for a given material system.

To demonstrate the predictive capability of Equation (2), data from Bowles et.al.[5] was used. Bowles et.al. [5] performed an extensive test program to measure the weight loss, oxidation layer thickness, and shrinkage of T650-35/PMR-15, 8 harness satin weave composites subjected to a wide range of aging temperatures. They also determined the effect of aging on the compressive strength of the material. Four specimen geometries with different A_A/A_{total} and A_T/A_{total} ratios aged at five different temperatures ranging from 204°C to 343 °C were examined. The specimen designation used by Bowles et.al and the area fraction ratios are given in Table 2.

Table 2. Specimen configurations from Bowles et.al. [5]

Specimen	A_A/A_{total}	A_T/A_{total}	$A_{total} (mm^2)$
T-3	0.014355	0.98564	19898.5
T-5	0.028442	0.97156	20385.5
T-12	0.068102	0.93190	21962.8
T-50	0.142571	0.85743	3233.6

For each of the test temperatures, two of the four specimen types were used to calculate f_A and f_T . Figures 4 and 5 show the variation of the weight loss factors as a function of

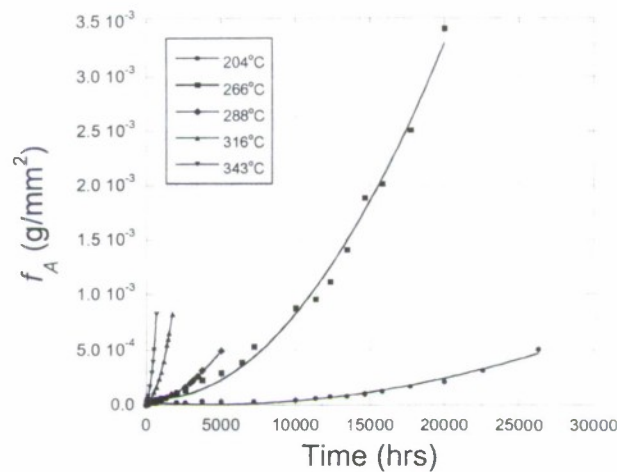


Figure 4 The weight loss rate function f_A as a function of aging temperature

aging temperature. Again, the magnitude of f_A is an order of magnitude greater than f_T for all aging temperatures. Additionally, Figure 4 illustrates the increase in the rate of f_A with an increase in aging time. This 'apparent' rate increase may be due to increases in the actual surface area (due to aging cracks). Since the oxidation process is typically diffusion rate limited rather than reaction rate limited, the crack development provides pathways for oxygen to diffuse deeper into the composite that increases the overall oxidation rate.

Figure 6 shows the prediction of T-5 weight loss history at 240°C over 25,000 hours of aging time. The T-5 specimen predictions are based on the functions f_A and f_T

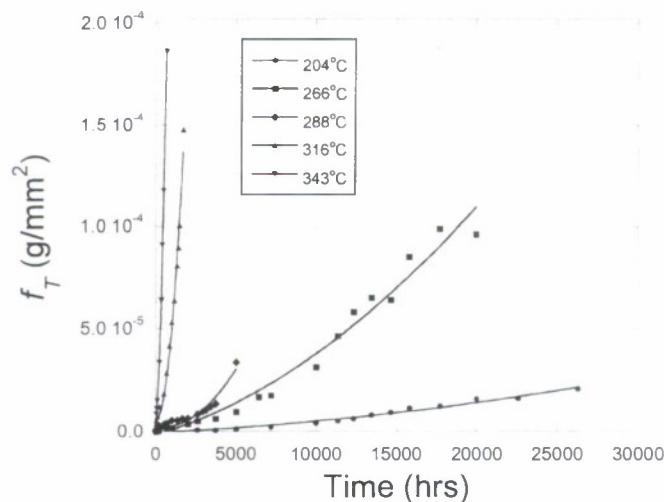


Figure 5 Weight loss rate function f_T as a function of aging temperature

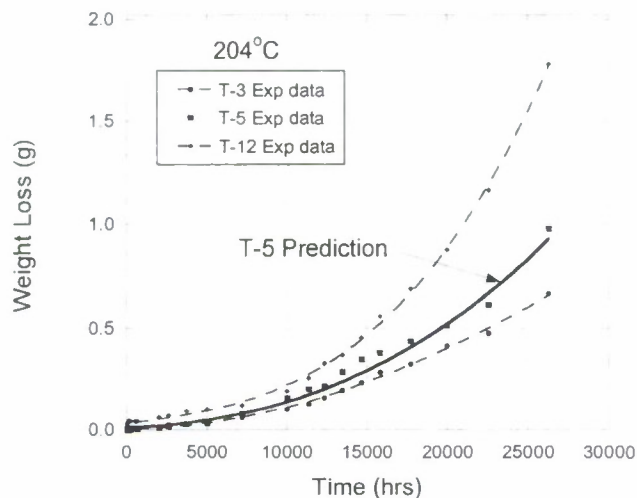


Figure 6 Weight loss rate functions f_A and f_T based on T-3 and T-12 specimen data used to predict T-5 weight loss history at 204°C for aging times over 25000 hours. Based on experimental data from Bowles et.al. [5].

determined from the T-3 and T-12 specimen data. From Table 2 it can be seen that the T-3, T-5, and T12 specimens all have similar total surface areas of approximately 20,000 mm². There is an excellent correlation of the predicted weight loss of the T-5 specimens and the predicted weight loss over the entire 25000 hour history. Similarly, Figure 7 shows the prediction of T-5 and T-50 weight loss history at 316°C based on functions f_A

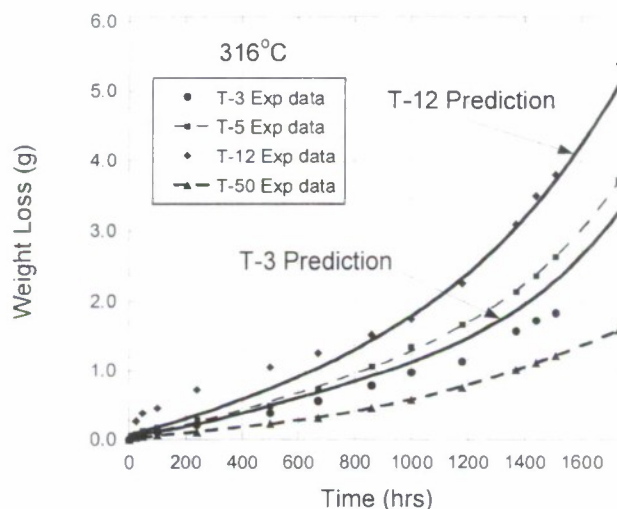


Figure 7 Weight loss rate functions f_A and f_T based on T-5 and T-50 specimen data used to predict T-3 and T-12 weight loss history at 316°C for aging times over 1700 hours. Based on experimental data from Bowles et.al. [5].

and f_T determined from T-3 and T-12 specimen data. It should be noted that the total surface area A_{total} of the T-50 specimens is approximately 6 times smaller than the T-3 and T-12 specimens. The prediction of weight loss for the T-3 specimen is excellent for aging times less than 600 hours and slightly higher than the experimental data for longer aging times. The weight loss data for the T-12 specimens is not consistent with other weight loss data for short aging time and is not well predicted by Equation (2). However for long aging times up to 1700 hours, there is excellent agreement between the predicted and measured weight loss data. The newly developed expression shown in Equation (2) is shown to accurately represent the long-term isothermal weight loss response of both unidirectional and woven composites. It has yet to be shown if the relationship will work for multidirectional composites. It represents the first time that the weight loss of specimens with significantly different axial, transverse, and total surface areas can be compared.

5.1.3 Accelerated Aging

Accelerated aging methods are needed to evaluate materials which are to be used under long-term exposure to elevated temperatures in oxidative environments. This work is conducted to examine the use of elevated pressure in conjunction with a 'realistic' use temperature to accelerate the rate of thermo-oxidative degradation in PMR-15 resin. Neat resin specimens are isothermally aged over a range of time periods in a pressure chamber, with a continuous supply of pressurized air, placed inside an air-circulating oven at an elevated temperature. Weight loss and volumetric changes are monitored as a function of aging time to quantify the degradation behavior. Optical microscopy is utilized to measure the degree and depth of oxidation development and to provide an insight into the formation and the growth of the oxidative layer. In addition, aged neat resin dogbone specimens are tested in tension, and their mechanical properties compared. Test data from this work will be subsequently utilized to link the diffusion-reaction models of chemical and thermo-oxidative degradation with micromechanical analysis and for development of a constitutive law to predict the behavior of PMR-15 reinforced composites.

Figure 8 shows the evolution of the oxidized layer as a function of aging time for PMR-15 specimens aged in air. Within a very short time period of 1 hr, an oxidized layer 11.0 μm thick forms on the exposed surfaces. The thickness of the oxidized layer for 288°C is seen to approach a plateau value as the oxidation growth rate reduces considerably for longer aging times. For the various temperatures, the aging of the specimens was terminated at the time surface cracks appeared. After surface crack initiation, the oxidation layer thickness no longer remains uniform, rather the oxidation progresses more rapidly into the resin at the crack sites. The time for surface crack initiation decreased for increasing aging temperature. Although the oxidation layer thickness appears to approach a plateau for the specimens aged at 316°C and 343°C prior to cracking, the high temperatures accelerate the crack initiation.

As with the volume change and weight loss measurements, the effect of the ambient moisture has a negligible effect on oxidation layer growth as compared to the dry air aging at 288°C. Since the ambient air aging is much less labor intensive, and thus less

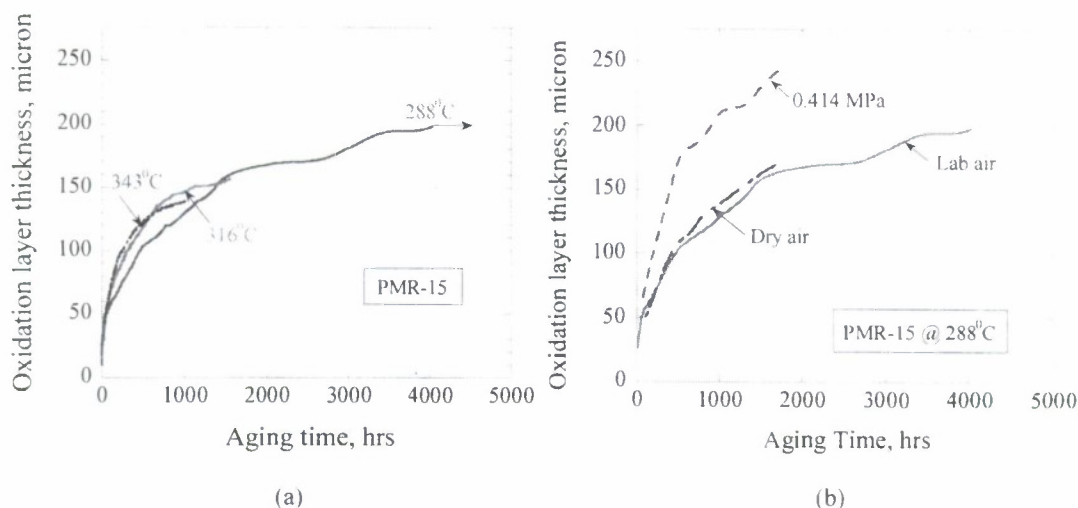


Figure 8 Influence of (a) temperature and (b) pressure on oxidation layer thickness in PMR-15 resin as a function of aging time

expensive to conduct than the dry air aging, the ambient air aging is preferable if the difference in the two aging conditions can be shown to be negligible. The effect of aging in PMR-15 neat resin at 0.414 MPa pressure versus ambient air pressure at 288°C is shown in Figure 8(b). The elevated pressure clearly increases the thickness of the oxidative layer. Whereas the oxidize layer thickness was similar for all of the aging temperatures up to approximately 1000 hours as shown in Figure 8(a), the elevated air pressure (thus increased partial pressure of oxygen) at the specimen surface resulted in a substantial increase in oxidation layer growth rate.

Figure 9 shows the influence of temperature and pressure on the oxidation layer growth rate. Although there is limited data in this region of steep gradients for the growth rate, the initial oxidation layer growth rate appears to be equivalent for the three aging temperatures shown in Figure 9(a). For aging times up to approximately 500 hours, the growth rate is higher for the higher temperatures. For latter times, the growth rate appears to approach an asymptote during which the oxygen diffusing to the oxidation front or transition region decreases due to the oxygen consumption within the oxidation layer and due to the distance that oxygen must diffuse to reach the transition region. In the absence of surface cracks, this oxidation process approaches an auto-retardation state due to the absence of oxygen in the transition region. The pressurization of the air during aging substantially increases the diffusion rate of the oxygen into the neat resin. Figure 9(b) shows a significantly higher oxidation layer growth rate for the specimens aged at 0.414 MPa air pressure. Again, the presence of ambient moisture in the air had negligible effect on the growth rate of the oxidation layer. Since the differences in the volume changes, weight changes, and oxidation layer thickness for the dry air aging specimens and the ambient air aging specimens was nearly equivalent, aging of the dry air specimens was terminated after approximately 2300 hours. Although, it is well know

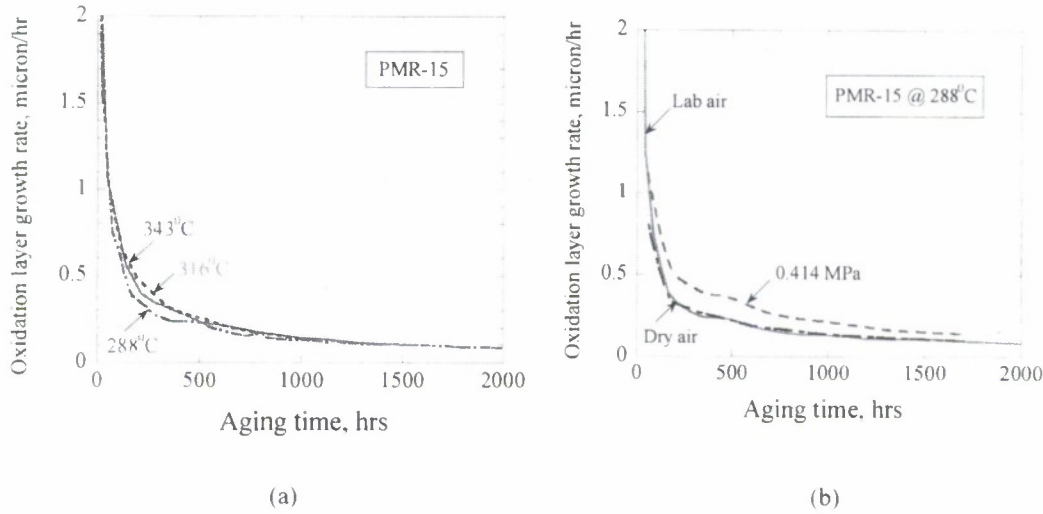


Figure 9 Influence of (a) temperature and (b) pressure on oxidation layer growth rate in PMR-15 resin as a function of aging time

that PMR-15 is highly susceptible to hydrolytic degradation [6], the ambient lab air did not appear to contain enough moisture to affect the results of the aging study.

5.2 Modeling Micro-Structure Evolution in Thermo-Oxidative Environments

In this modeling effort, it is assumed that the transport of the gas within the material is controlled by Fickian diffusion. The adsorbed oxygen diffuses into the volume and initiates the reaction of the polymer. The rate of reaction is modeled as a function of both the oxygen availability (through diffusion) and the polymer availability (tracking end products of reaction). The oxygen predominately diffuses again (deeper through the thickness of the polymer) when polymer availability for reaction is restricted.

5.2.1 Sorption and Diffusion Modeling

With $C(x,y,z;t)$ denoting the concentration field at any time within a domain with a diffusivity of D_{ij} and consumptive reaction with a rate $R(c)$, the diffusion reaction with orthotropic diffusivity is given by Equation (3)

$$\frac{\partial C}{\partial t} = \left(D_{11} \frac{\partial^2 C}{\partial x^2} + D_{22} \frac{\partial^2 C}{\partial y^2} + D_{33} \frac{\partial^2 C}{\partial z^2} \right) - R(C) \quad (3)$$

subjected to the boundary conditions,

$$\begin{aligned} C &= C^s \text{ on the exposed boundaries} \\ dC/dt &= 0 \text{ on symmetry boundaries} \end{aligned}$$

The boundary sorption on the exposed boundaries is given by Henry's equation

$$C^S = S P \quad (4)$$

where S is the solubility and P is the partial pressure of the oxygen in the environment. The diffusivities are temperature dependent typically given in Arrhenius form:

$$D_{ij} = D_0 \exp(-E_a/RT) \quad (5)$$

and determined using permeability tests at lower temperatures to determine the pre-exponent (D_0) and the activation energy parameters (E_a). Table 3 shows the values of these parameters for a typical high-temperature polyimide resin as determined in its virgin state, i.e., unoxidized condition.

Table 3 Constants for evaluating diffusivity of polyimide resin

	Unoxidized, $\phi=1$ (Abdeljaoued, 1999)
D_0	$6.10 \text{ e-}11 \text{ m}^2/\text{sec}$
E_a	-19700 J/mol
R	$8.31447 \text{ J}/(\text{mol}^0\text{K})$

5.2.1.1 Heterogeneity in Diffusivity

Thermo-oxidative aging of the polymeric material will change the chemical composition of the polymer and hence the physical properties of the material. Therefore, any part of the polymer subjected to thermo-oxidation will invariably contain multiple material phases - namely, the unoxidized or virgin polymer, the active reaction zone (where a mix of oxidized and unoxidized polymers exists) and an oxidized polymer phase. In general, the diffusivities for each of these phases will be different, while the diffusivity of the oxidized polymer layer is the controlling parameter as the diffusion of oxygen through the oxidized layer is the source of oxygen supply to the unoxidized layer. In this work several simulations of oxidation layer growth were performed. Initially, for lack of better information, it was assumed that the diffusivities for the three phases are the same and equal to the unoxidized value. Later, the case where the diffusivity D_{ij} at a material location is assumed to be a linear interpolation of the diffusivities of the oxidized and unoxidized materials, denoted by D_{ij}^{ox} and D_{ij}^{un} , respectively is considered. For the remainder of this report, superscripts ox and un will be used with diffusivity values whenever needed for clarity.

5.2.2 Reaction Modeling

The reaction rate term, $R(C)$, in Equation (3), models the reaction of the oxygen with the polymer. Oxygen can react with the end caps of the polymer and/or the backbone of the polymer. The reaction modeling presented here assumes that the reaction products (water and other volatiles) leave the polymer instantaneously and no modeling of the outgassing is therefore attempted. The reaction rate depends upon temperature and oxygen concentration. While the Arrhenius-type kinetics models are suitable for capturing the

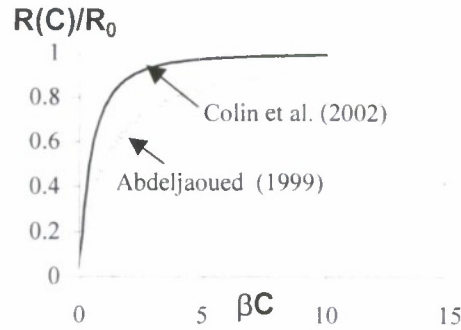


Figure 10 Typical model of reaction rate dependence on concentration.

temperature, the mechanistic models capture the reaction-rate dependence on the concentration dependence as well. The mechanistic models typically determine the reaction rate based on a saturation reaction rate (R_0) when the reaction is not oxygen deprived. The reaction rate is reduced when the oxygen availability is reduced, therefore,

$$R(C) = R_0 f(C) \quad (6)$$

where R_0 is the saturation reaction rate. The function $f(C)$ in Equation (6) models the situation in which the amount of oxygen available for reaction is lower than that required for the maximum reaction rate reached under saturation conditions. The reduction in reaction rate can be modeled using Equation (7).

$$f(C) = \frac{2\beta C}{1 + \beta C} \left[1 - \frac{\beta C}{2(1 + \beta C)} \right] \quad (7)$$

Figure 10 shows the dependence of the reaction rate on the concentration as modeled by Equation (7). The abscissa has a normalized concentration parameter (βC) in which the parameter, β , nondimensionalizes the concentration field. According to Equation 7, there is a rapid acceleration phase ($0 < \beta C < \sim 3$) and a constant phase ($\beta C > 3$). For this analysis, the simpler, two-phase, reaction rate to concentration dependence is chosen.

The value of β can be determined from weight loss data obtained at two oxygen partial pressures, typically in pure O_2 and in air. In order to determine this value, we need weight loss measurements at two concentrations which translate to the reaction rates at those two concentration values. Since the weight loss is taken to be proportional to the oxygen consumption rate, the ratio of the weight loss determined at two concentrations is the same as $R_1(C_1)/R_2(C_2)$. For example, the ratio of the weight loss between pure O_2 ($C_2 = 3.74 \text{ mol/m}^3$) and air ($C_1 = 0.79 \text{ mol/m}^3$) is about 0.7. Therefore,

$$\frac{2\beta C_1}{1 + \beta C_1} \left[1 - \frac{\beta C_1}{2(1 + \beta C_1)} \right] = 0.7 \frac{2\beta C_2}{1 + \beta C_2} \left[1 - \frac{\beta C_2}{2(1 + \beta C_2)} \right] \quad (8)$$

Solving the equations produces three roots: $[-3.5593, -0.42657, 0.91947]$, with only one physically feasible value for the polyimide resin being $\beta = 0.919$.

5.2.3 Oxidation Layer Growth Modeling

The simulation of the oxidation layer growth requires the specification of the reaction rate R_0 and a mechanism for reaction completion/cessation. Considering that the oxidation reaction will stop if it is oxygen-starved as modeled by Equation (7), the reaction will stop when all the active polymer sites are consumed. In the latter case, the oxygen will again diffuse deeper into the material in favor of the reaction. In this section the case where the diffusing oxygen finds the active polymer reaction sites creating an active oxidation layer followed by advancement of the layer upon the reaction completion is considered.

5.2.3.1 Active Oxidation Layer Size

Under the assumption that abundant active sites are available for reaction in the polymer, the diffusion reaction equation (Eq. 3) leads to a zone over which oxidation takes place. This zone will be proportional to the ratio of the diffused oxygen volume over reacted volume. For the polyimide resin under consideration, the active reaction zone forms quickly (can be seen within 1 hour). The optical experimental observations reported by Ripberger, et al. (2004) also verify the existence of a zone between the oxidized and unoxidized regions. Figure 11 shows the active reaction zone measurements for polyimide resin at 288°C . This figure shows two distinguishable region sizes - namely $17\ \mu\text{m}$ before 40 hours and $25\ \mu\text{m}$ after 40 hrs of aging. These active reaction zone sizes correspond to an R_0 value of about $3.5\ \text{mol}/\text{m}^3\cdot\text{min}$ for the first 40 hours of aging which then slows down to a reaction rate corresponding to about $2\ \text{mol}/\text{m}^3\cdot\text{min}$.

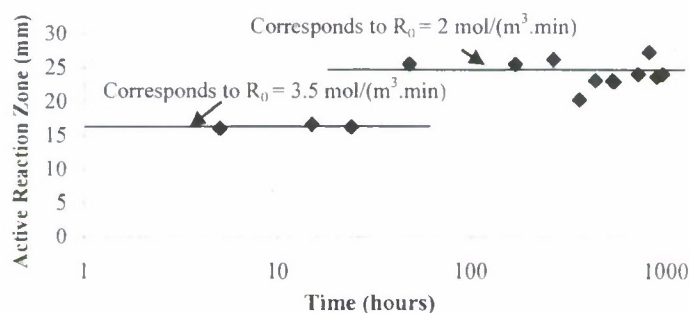


Figure 11 Active reaction zone variation with time illustrating slowing of the oxidation reaction after 40 hours of aging.

5.2.3.2 Reaction Termination Criterion

While the active zone modeling describes the reaction rate and its dependence on oxygen availability (concentration fields), the diffusion-reaction system will be stationary (does not grow into the polymer thickness) if sufficient amount of polymer is available for reaction. However, under longer-term aging (tens to hundreds of hours) conditions, the

oxidation layer will grow moving the active reaction zone into the polymer, and three zones can be observed along the depth of the polymer, as illustrated in Figure 12. Therefore, a polymer availability state variable (ϕ) is defined which indicates the availability of an active polymer site for reaction. The state variable ϕ is parameterized to vary from $\phi_{ox} < \phi < 1$, where ϕ_{ox} denotes completely oxidized polymer, and $\phi = 1$ denotes unoxidized polymer. It is assumed that the reaction is terminated when ϕ equals ϕ_{ox} .

In this effort, the weight loss information is utilized to determine the value of ϕ_{ox} . In order to determine this value, a relation between the oxidation layer size and the weight loss must first be established. The most common assumption relating the two parameters is that the weight loss rate ($\frac{dW}{dt}$) is proportional to the reaction rate $R(C)$, and α is the constant of proportionality:

$$\frac{dW}{dt} = \alpha R(C) \quad (9)$$

The oxidation state parameter determined at any material point in the material is determined as the current weight of the material over its original (unoxidized) weight, i.e.,

$$\frac{d\phi}{dt} = \frac{dW}{dt} \quad (10)$$

Combining Equations (9) and (10), we obtain,

$$\frac{d\phi(t)}{dt} = \alpha R(C) \quad (11)$$

The parameters, ϕ_{ox} and α , can be determined from the weight loss data for a known specimen geometry together with oxidation layer size data measurements.

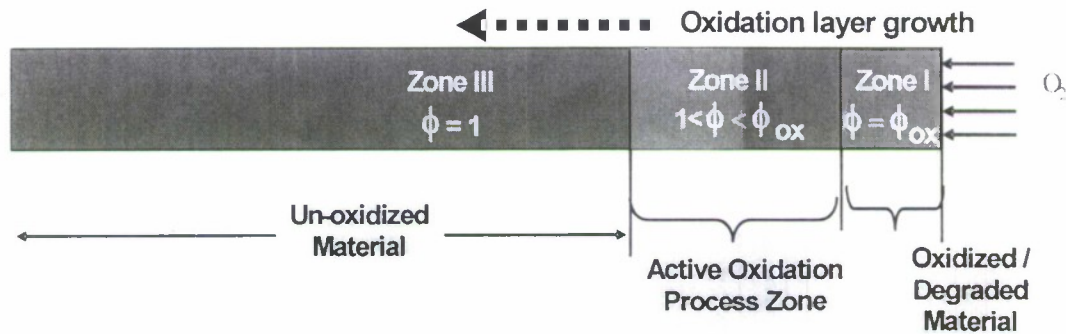


Figure 12 Schematic of the three-zones in thermo-oxidation. The oxidized region is followed by active zone separating the oxidized and unoxidized regions

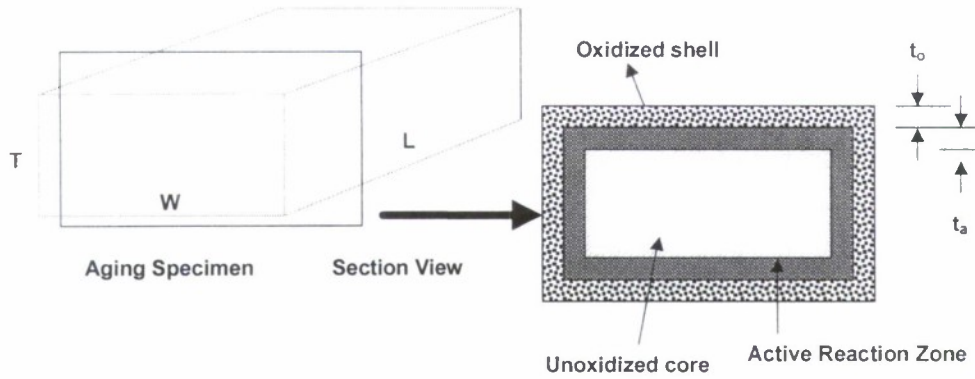


Figure 13 Geometry of the specimen used for aging with all boundaries exposed to oxygen. The oxidized layer, active reaction zone and the unoxidized regions are illustrated in the sectional view.

5.2.4 Determination of ϕ_{ox} from Weight Loss Experimentation

In an inert environment, polymers undergo physical and chemical aging only, whereas in an oxidizing environment, specimens will undergo physical, chemical and oxidative aging. Therefore, aging experiments are conducted both in inert atmospheres (e.g. argon) and oxidative atmospheres (air), and the weight loss is recorded at various time intervals in order to determine the effect of oxidation on aging. Let the initial specimen dimensions be given by length (L), width (W) and thickness (T). At a particular time interval if the weight loss fraction (weight loss/original weight) in the inert atmosphere is given as γ , and weight loss fraction after the same time period in air is given by ε , then the weight loss fraction due to oxidation alone is $(\varepsilon - \gamma)$. Let the observed thickness of the completely oxidized layer and the active oxidation layer be denoted by t_o , and t_a , respectively, as shown in Figure 13. The initial volume of the specimen (V), the volume of the fully oxidized zone (V_o), and the volume of the active oxidation zone (V_a) are therefore given by:

$$V = LWT$$

$$V_o = \{LWT - (L - 2 * t_o)(W - 2 * t_o)(T - 2 * t_o)\} \quad (12)$$

$$V_a = \{LWT - V_o - (L - 2 * (t_o + t_a))(W - 2 * (t_o + t_a))(T - 2 * (t_o + t_a))\}$$

Assuming that the oxidative weight loss is confined to the oxidation zone and that ϕ_{ox} varies linearly in the active oxidation zone, the weight loss in the oxidized zone should therefore be equal to the weight loss in the specimen, i.e.,

$$\left[(1 - \phi_{ox})V_o + \left(\frac{1 - \phi_{ox}}{2}\right)V_a \right] \rho = (L * W * T)[\varepsilon - \gamma]\rho \quad (13)$$

Solving for ϕ_{ox} , we obtain,

$$\phi_{ox} = 1 - \frac{V(\varepsilon - \gamma)}{V_o + \frac{1}{2}V_a} \quad (14)$$

Equations (12)-(14) determine the value of ϕ_{ox} from oxidation layer size observations and weight loss data determined from aging in inert (γ) and oxidative (ε) environments.

5.2.5 Modeling of Accelerated Aging of High Temperature Polymers

The particular issue of accelerated aging by application of excess temperature or pressure is of interest, as it may allow expedited determination of thermo-oxidative properties of new systems. Data presented in section 5.1.3 provides evidence of the physical effects of the controllable parameters. An effort was therefore initiated to model the temperature and pressure effects.

5.2.5.1 Simulation of Arrhenius Temperature Dependence

We note again that the oxygen concentration is tracked through the Fickian diffusion equation with a reaction term and orthotropic diffusivity, as given by

$$\frac{\partial C}{\partial t} = \left(D_{11} \frac{\partial^2 C}{\partial x^2} + D_{22} \frac{\partial^2 C}{\partial y^2} + D_{33} \frac{\partial^2 C}{\partial z^2} \right) - R(C)$$

subject to the boundary conditions,

$$C = C^s \text{ on the exposed boundaries}$$

$$dC/dt = 0 \text{ on symmetry boundaries}$$

The temperature dependence of the diffusivity $D_{ij} = D_{ij}^0 \exp(-E_{ij}^a/RT)$ and the reaction rate $R(C)$ through the saturation reaction rate $R_o(T) = R_o' \cdot \exp(-R^a/RT)$ are expressed by Arrhenius-type relationships. Along with experimental oxidation layer thickness measurements for neat resin PMR-15 specimens aged at 288°C, oxidation thickness measurements were accomplished for specimens aged at 316°C and 343°C. Figure 14 shows predictions of the oxidation layer thicknesses for 288°C, 316°C, and 343°C neat resin PMR-15 specimens based on 288°C properties. The figure shows that the model accurately predicts the 316°C and 343°C oxidation layer thicknesses, and the temperature dependence of the reaction rate and diffusivity are accurately represented.

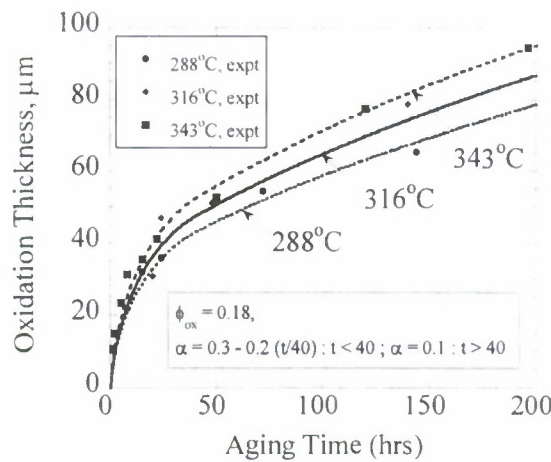


Figure 14 Prediction of oxidation thickness at 316°C and 343°C based on 288°C model parameters

5.2.5.2 Influence of Pressure on Oxidation Growth

Thermal aging in a pressurized environment has been shown to accelerate the oxidation layer growth rate and increase the weight loss. Since the partial pressure of a gas is directly proportional to the total pressure and in general the solubility of gases increase with increasing pressure, the boundary sorption as expressed by $C^S = S \cdot P^O$ is expected to increase with increasing pressure. Figure 15 shows the results of a parametric evaluation of how changes in the sorption affect the predicted oxidation layer thickness. Oxidation layer thickness for neat resin PMR-15 specimens aged at ambient and elevated pressures at 288°C are also shown in the figure. The predicted oxidation layer thickness increases with increasing oxygen concentration on the boundary and for the sorption value $C^S = 1.25$, there is a good correlation with the pressurized aging data for aging times up to 200 hours. Figure 16 shows the predicted oxidation layer thickness for predictions up to 800 hours of aging time. The results show good agreement with the experimental data.

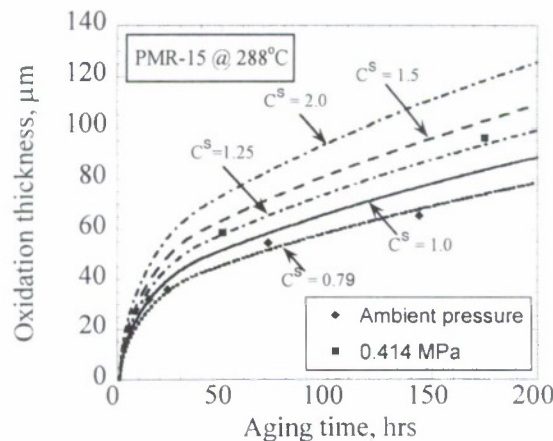


Figure 15 Influence of sorption on the oxidation layer thickness

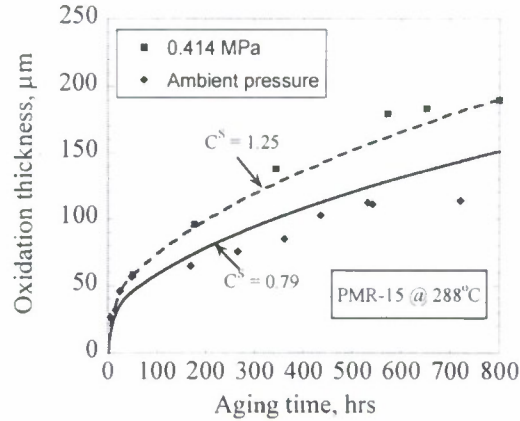


Figure 16 Prediction of oxidation thickness for pressurized aging of PMR-15

5.2.7 Three-Dimensional Finite Element Model

The diffusion-reaction oxidation model presented here is implemented into a three-dimensional Galerkin Finite Element Analysis (GFEA). The GFEA method is more

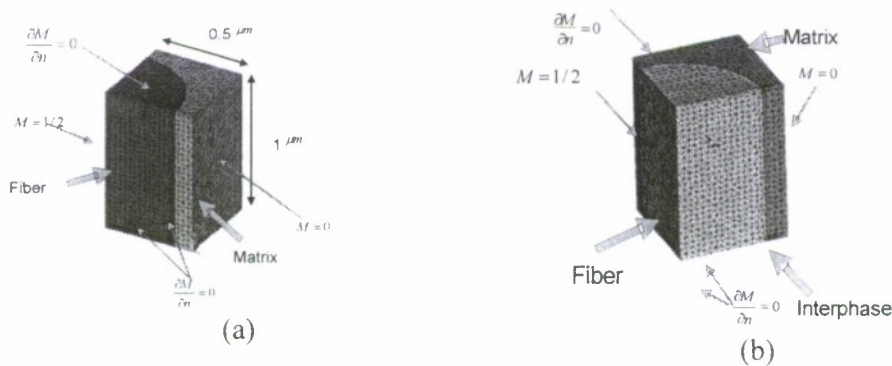


Figure 17 Typical unit cells used in the FEA analysis. (a) without an interphase region and (b) with an interphase region

appropriate for studying structural scale problems, and the CPU time required precludes its use in parametric analyses as required for correlation with experimental results and parameter determination. The GFEA requires mesh sizes in 1-μm scale and time increments in 1-sec steps. A 200-hour oxidation simulation with 100-μm zone size typically requires mesh sizes in the order of 100,000 DOF and 720,000 time steps.

5.2.7.1 Extension of Oxidation Growth Prediction to Representative Volume Elements

A composite repeated volume element (unit cell) consisting of a single fiber in a hexagonal unit-cell packing is considered. The fiber, matrix and interphase domains are individually modeled for a nominal fiber volume fraction of 50% and an assumed

interphase thickness. Figure 17 shows the unit-cell structure after exploiting the geometric symmetries.

Consider the time-dependent three-dimensional temperature distribution in a three-dimensional part, $\Omega \subset R^3$ bounded by $\Gamma = \Gamma_T \cup \Gamma_Q$ and $\Gamma_T \cap \Gamma_Q = \emptyset$, where Γ_T is the temperature specified and Γ_Q is the heat flux specified boundaries. The spatial and temporal coordinates are denoted by $x = \{x, y, z\}$ and $t \in (0, \infty)$. The overall thermal energy balance equation for the effective composite media is:

$$\left(v_p \rho_r C_{pr} + v_f \rho_f C_{pf} \right) \frac{\partial T}{\partial t} = \left(K_{xx} \frac{\partial^2 T}{\partial x^2} + K_{yy} \frac{\partial^2 T}{\partial y^2} + K_{zz} \frac{\partial^2 T}{\partial z^2} \right) \quad (15)$$

Where v_p is the porosity volume fraction, v_f is the fiber volume fraction, ρ_r is the resin density and ρ_f is the fiber density. C_{pr} is the specific heat of resin, C_{pf} is the specific heat of fiber, T is the absolute temperature and t is time and K_{ij} is the equivalent thermal conductivity. The equivalent thermal conductivity (K_{ij}) can be calculated by the fiber thermal conductivity tensor (K_{ij}^f) and the resin thermal conductivity (K_{ij}^r) using Equation (16).

$$K_{ij} = K_{ij}^r \frac{1 + k_{ij}^f}{1 - k_{ij}^f} \quad k_{ij}^f = \frac{(K_{ij}^f - K_{ij}^r)(1 - V_p)}{(K_{ij}^f + K_{ij}^r)} \quad (16)$$

The diffusion in a composite structure is assumed to be governed by Fick's second law

$$\frac{\partial C}{\partial t} = D_{11} \frac{\partial^2 C}{\partial x^2} + D_{22} \frac{\partial^2 C}{\partial y^2} + D_{33} \frac{\partial^2 C}{\partial z^2} \quad (17)$$

D_{ij} are the anisotropic and temperature dependent mass diffusion constants. C is the concentration of the oxygen uptake in percent weight.

5.2.7.2 Oxidative Aging of Unidirectional Composites

Three-dimensional oxidation modeling is performed using finite element analysis (FEM) on representative volume elements of the composite. Inputs to the model include material properties, simulation parameters, and the unit-cell geometry. Unit cells, as shown in Figure 18, describe the geometry of the constituents, volume fraction, and orientation of the constituents in the composite, while the model allows multi-fiber and multi-cell simulations to be performed. The unit cell geometry and element meshes are generated using commercially available computer aided design (CAD) and FEM programs. For pure oxygen, the boundary concentration is taken to be C^s is 3.74 mol/m^3 . For air (as used for all simulations in this work), it is 0.79 mol/m^3 . The model is meshed such that all constituents are perfectly bonded with continuity of the oxygen concentration imposed at

the interface. The mesh size is varied between simulations. Two output files describing the concentration profiles (C) and the oxidation state (ϕ) in the model are produced at every time step.

For the majority of the PMC simulations presented, a 50% fiber volume fraction is assumed with no explicit representation of the interphase region, unless otherwise noted. It is assumed that the fibers are in a square packing arrangement, with each having a diameter of $10\text{ }\mu\text{m}$ and a spacing of $12.532\text{ }\mu\text{m}$ (center-to-center) between adjacent fibers. To reduce simulation time, the representative volume element (RVE) model consists of only one quarter of a unit cell single fiber and the surrounding matrix as shown in Figure 18(a). The mesh has an element size of $1.28\text{ }\mu\text{m}$, with a total of 13,226 nodes and 6,845 elements. The length of this model is $200\text{ }\mu\text{m}$. The results of the oxidation simulation of the RVE with the surface exposed to the air being parallel to the fiber cross section are shown in Figure 19. The figure shows the region where the ϕ values are within 5% of completely oxidized (light gray, $\phi = \phi_{ox}$) and un-oxidized (dark, $\phi = 1$) at 50, 100, 150 and 200 hours of exposure. The fiber diffusivity (D_f) is taken to be 1/1000 that of the unoxidized diffusivity of the matrix ($D_f = D_m^{un}/1000$). The prediction of oxidation propagation along the fiber direction is less than the experimentally observed extent of oxidation

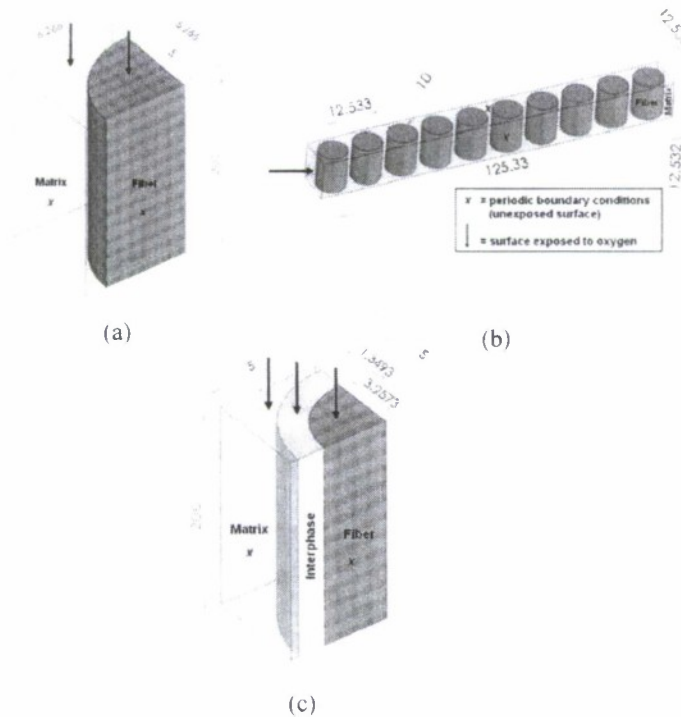


Figure 18 Unit cells for modeling (a) axial oxidation, (b) transverse oxidation, and (c) the influence of interphase on oxidation growth in a unidirectional composite

indicating that the diffusion of oxygen in the fiber direction is not fully accounted for in this model. Next, several simulations are performed to determine the impact of the fiber diffusivity on the oxidation of the matrix. The fiber diffusivity is varied such that $D_f = (1/1000, 1/100, 1/10, 1, 10) \times D_m^{un}$. The results are shown in Figure 20. The differences between the effective unit cell diffusivity assuming that the fiber diffusivity D_f is $1/10$, 1 , and 10 times matrix diffusivity D_m^{un} are significant, indicating that fiber diffusivity has a considerable effect on composite oxidation behavior. For fiber diffusivities below $1/10 \times D_m^{un}$, oxygen diffusion through the fiber becomes insignificant, there is little change in overall oxidation, and oxidation is driven by matrix diffusivity alone.

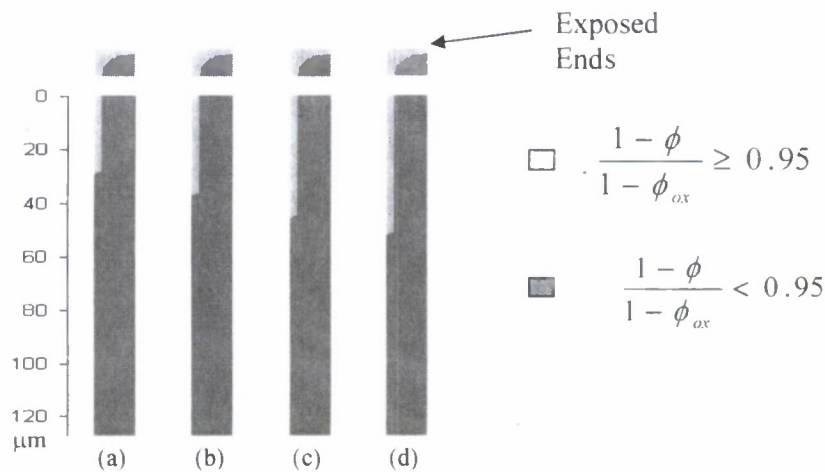


Figure 19 Simulations of oxidation growth in axial direction at (a) 50 hrs, (b) 100 hrs, (c) 150 hrs, and (d) 200 hrs of exposure

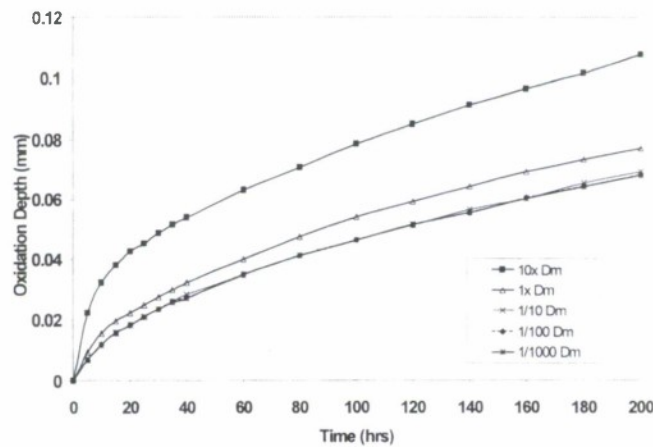


Figure 20 Effect of fiber diffusivity on matrix oxidation

Simulations corresponding to the exposure of transverse surfaces of the lamina were also performed. Since the repeated unit is not a single fiber, a model consisting of 10 fibers in a single row was created as shown in Figure 18(b). As before, the fibers have a diameter of $10\text{ }\mu\text{m}$ and a spacing of $12.532\text{ }\mu\text{m}$ (center-to-center). The mesh has an element size of $1.86\text{ }\mu\text{m}$, with a total of 34,300 nodes and 22,493 elements. As before, the fiber diffusivity is taken to be 1/1000 that of the unoxidized diffusivity of the matrix ($D_f = D_m^{un} / 1000$). Figure 21 illustrates the simulation of oxidation growth transverse to the fibers while Figure 22 shows a detailed view of the active reaction zone as oxidation

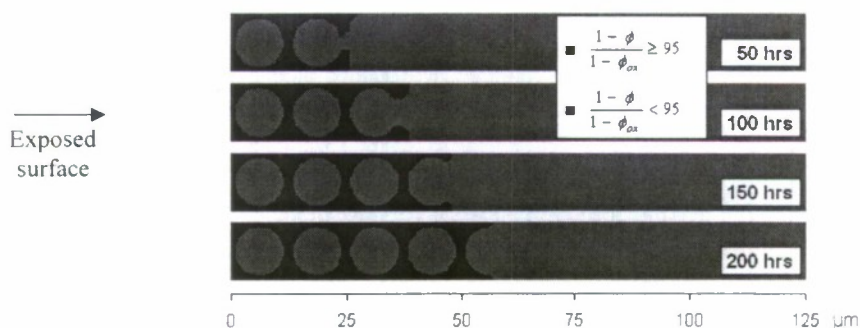


Figure 21 Transverse oxidation growth in a composite lamina

occurs around the fiber. The observed active reaction front (zone II) is approximately one fiber diameter in size ($10\text{ }\mu\text{m}$) which is smaller than that observed in the neat resin. The smaller active reaction zone (II) is a result of lower effective diffusivity in the transverse direction due to the presence of the fiber.

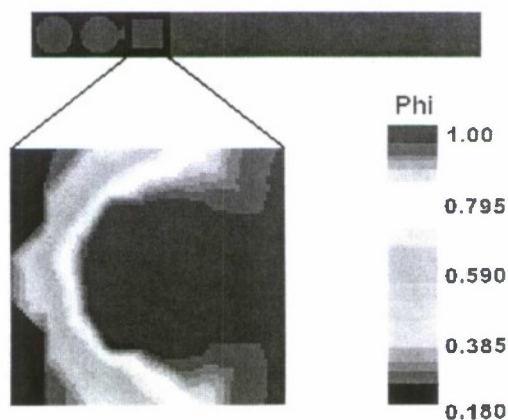


Figure 22 Detail of active reaction zone from transverse simulation

A comparison of the anisotropic nature of the oxidation growth in the transverse and axial directions for 200 hours of aging is shown in Figure 23. The differences in the transverse and axial oxidation growth are observed to be small for the simulations performed. This

is to be expected because the diffusion process for these simulations is dominated by the diffusivity of the matrix alone, since the fiber diffusivity is assumed to be negligible ($D_f = D_m^{un} / 1000$). Moreover, the RVE unit cells shown in Figure 18 do not include the fiber-matrix interphase region that can greatly contribute to the diffusion along the fiber axis

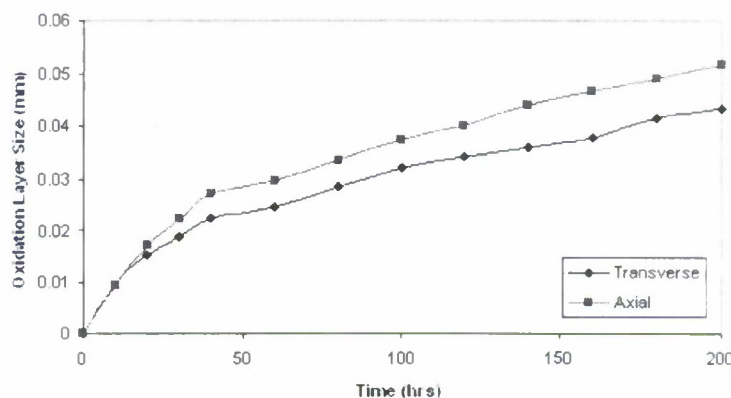


Figure 23 Transverse vs. axial oxidation depth in a unidirectional composite

direction. Neither have we accounted for the increase in effective diffusivity due to presence of damage such as fiber-matrix debonds and/or matrix microcracking.

To investigate the role of the interphase region, particularly if the interphase thickness and its diffusivity are large, a parametric study is next conducted to understand the influence of the interphase parameters on the oxygen diffusivity and transport in the composite. This is accomplished by adding a concentric region around the fiber that has distinct material properties to represent the interphase region. A high interphase volume fraction (33%) and a low fiber volume fraction (33%) are chosen to exaggerate the effects of the presence of the interphase. For geometric and meshing convenience, the model assumes that the fiber diameter is $6.51 \mu\text{m}$, the interphase thickness is $1.35 \mu\text{m}$, and the fiber spacing is $10 \mu\text{m}$ center-to-center, as shown in Figure 18(c). This produces a quarter model unit cell measuring $5 \mu\text{m} \times 5 \mu\text{m} \times 200 \mu\text{m}$ in size. In addition, the fiber is assigned an anisotropic diffusivity. For the initial simulations, the axial diffusivity is assumed to be equal to that of the resin (D_m^{un}) and the transverse diffusivity is taken to be $D_m^{un} / 10$. The interphase layer is assigned a diffusivity values of $100\times$, $1\times$ and $1/100\times$ that of the un-oxidized resin (D_m^{un}). Both the fiber and the interphase region are assumed to be nonoxidized and only the matrix phase reacts with oxygen.

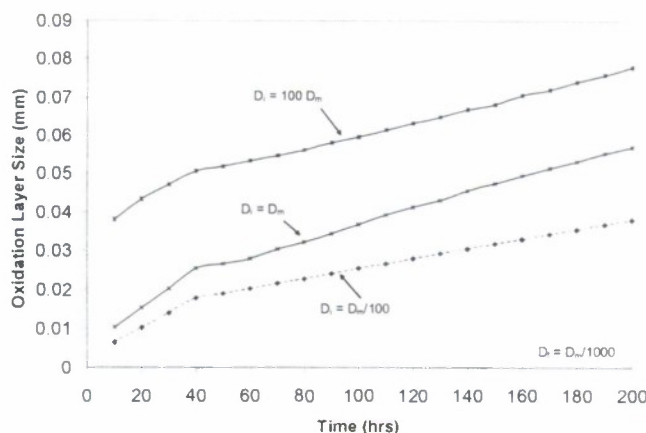


Figure 24 Oxidation layer size variation with interface diffusivity

Figure 24 shows the parametric analysis of axial oxidation region growth for the three interphase diffusivity values. The simulation with the high interphase diffusivity value shows considerable oxidation layer thicknesses and accelerated growth even during the early hours of aging. The diffusion-controlled behavior is clearly evident as the oxidation process is accelerated due to the presence of additional diffusion paths through the interphase.

For the case where the path of the oxygen to the matrix/interphase region is due to the fiber-matrix debonds, the effective diffusivity and hence the oxidation process can be effectively modeled without a discrete representation of the debonds. This can be accomplished by assigning an artificially high diffusivity value to the fiber. For such a case, it is in essence assumed that the path the oxygen takes to penetrate to the interior is inconsequential, and that it is the consequence of having the oxygen available for the oxidation process in the interior of the composite that is important. Using this approach may eliminate the need to do costly modeling of the discrete fiber-matrix debonds in the analysis. Further analysis is in progress to parametrically estimate the increase in the oxidation layer depth in the matrix due to the presence of a diffusive fiber and interphase region.

5.2.7.3 Composite Oxidation Studies with Representative Volume Elements

In this section, the diffusivity of the fiber is parametrically varied to evaluate its influence on oxidative growth. Let D_f , D_i and D_m denote the constituent level isotropic diffusivity values of the fiber, interphase region and matrix, respectively. A three-dimensional RVE is used with PMR-15 matrix and an interphase region is initially not included. The oxidation simulation is run for up to 200 hours because steady state oxidation layer growth can be expected at that time. The oxidation state in the model is plotted at various time intervals (25, 50, 100 and 200 hours).

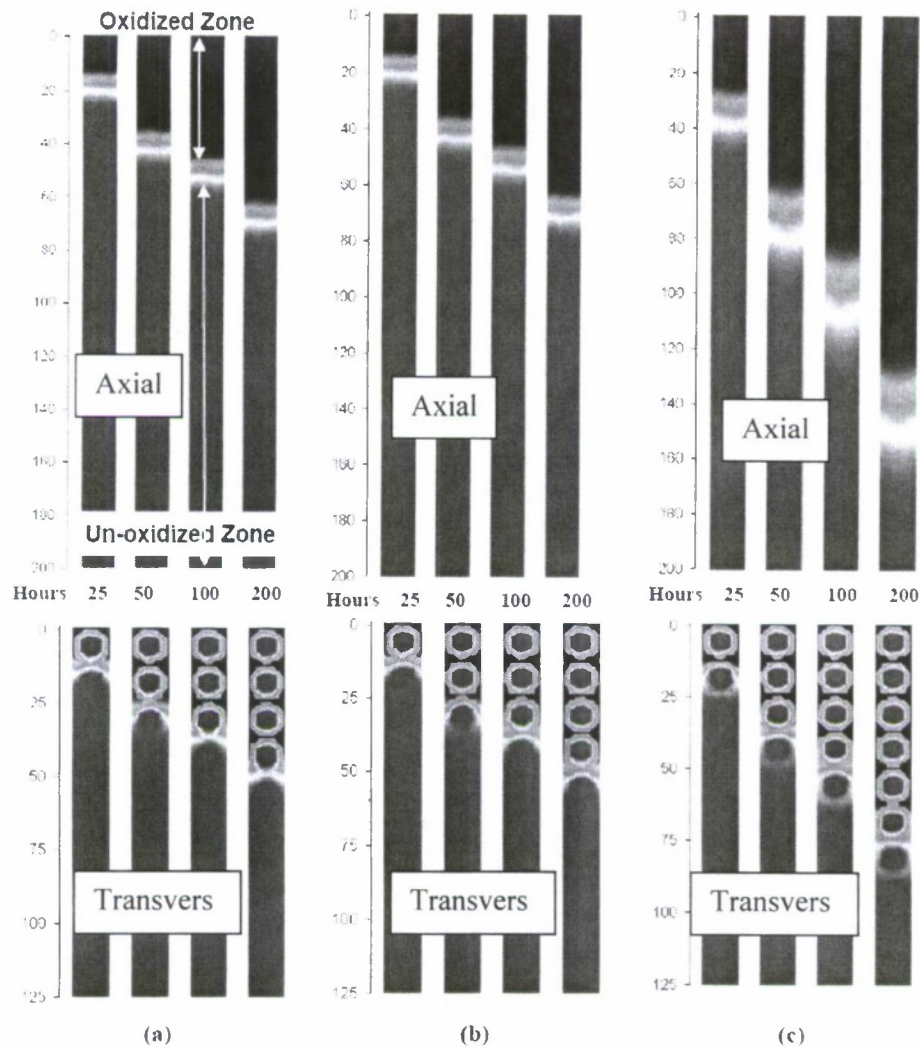


Figure 25 Effect of fiber diffusivity on composite oxidation. Black regions are completely oxidized and grey regions are unoxidized. The transition region is contoured from black to grey based on the oxidation state. All dimensions shown are in μm . (a) $D_f = 0.01 D_m^{\text{ox}}$, (b) $D_f = 0.1 D_m^{\text{ox}}$, (c) $D_f = 10 D_m^{\text{ox}}$

Figure 25 shows the oxidation growth in both axial and transverse directions for various fiber diffusivities and at several hours of exposure. Let the oxidation thickness in the axial and transverse direction be denoted by t_{axial} and t_{trans} , respectively. Similarly, the thickness of the reaction zone in the axial and transverse directions are denoted by l_{axial} and l_{trans} , respectively. The oxidation layer sizes (t_{axial} and t_{trans}) and the reaction zone size (l_{axial} and l_{trans}) are measured using the oxidation state (ϕ) values. The oxidized layer has been considered to have $\phi < 0.181$ (99.5% oxidation) and the unoxidized layer with $\phi > 0.998$ (corresponding to 0.2 % oxidation in the material). These limits are primarily chosen to ensure consistent measurement of the zone sizes throughout the parametric study.

Figure 25(a) shows the case in which fiber has a very low diffusivity, equivalent to one hundredth that of the oxidized resin, Figure 25(b) corresponds to that with a fiber diffusivity of one tenth that of the resin and Figure 25(c) shows the oxidation layer size when the fiber diffusivity is about ten times that of the resin. For these simulations, only the diffusive behavior of the fibers is varied whereas both the diffusion and reaction behavior of the resin is considered. When the oxidation state of the resin reaches full oxidation ($\phi=\phi_{ox}=0.18$), the oxidized resin becomes non-reactive and diffusive only. Prior analysis shows that the diffusivity of the oxidized matrix is higher than that of the unoxidized matrix.

It is generally believed that the oxidation process in PMR-15 resin is diffusion limited versus reaction rate limited. Although the constituent level diffusivities of the composite are assumed to be isotropic, the geometry of the unidirectional composite results in effective diffusivity that is transversely isotropic. Thus, in order to establish the relationship between the homogenized diffusivities of the oxidized composite and the observed oxidation layer size, we calculate the ratio of the oxidation layer size in the composite in the axial direction (t_{axial}) to that in the transverse direction (t_{trans}) and as a first approximation compare it with the corresponding ratio of homogenized diffusivities of the composite. The composite effective diffusivities were recently calculated using homogenization theories for various ratios of D_f/D_m and are listed in Table 4. Here D_1 and D_2 denote the effective axial and transverse diffusivities, respectively, of the unidirectional composite. Table 4 also shows a comparison of the anisotropy ratio of the diffusivities (D_1/D_2) with the corresponding oxidation layer ratio (t_{axial}/t_{trans}) and the reaction zone ratio (l_{axial}/l_{trans}) at 200 hour simulations for some selected fiber and matrix diffusivity values. For values of $D_f/D_m < 10$, the oxidation growth is diffusion limited and

Table 4 Anisotropy in composite diffusivity and its correlation with oxidation layer size

Diffusivity/ D_m^{ox}		Diffusivity Factor			Predicted Oxidation Layer Size Ratio (t_{axial}/t_{trans})	Predicted Reaction Zone Size Ratio (l_{axial}/l_{trans})
Matrix	Fiber	D_1/D_m^{ox}	D_2/D_m^{ox}	D_1/D_2		
1	0.1	0.551	0.415	1.33	1.31	1.15
	2	1.499	1.4	1.07	1.20	0.83
	4	2.34	1.653	1.42	1.43	0.95
	10	5.49	2.41	2.28	1.56	2.00
	20	10.48	2.69	3.89	2.71	2.68
	46	23.45	2.89	8.11	3.25	3.5
	60	30.52	2.91	10.49	3.45	3.93
	100	50.37	2.99	16.84	4.41	5.39
	200	100.5	3.015	33.33	7.40	10.53

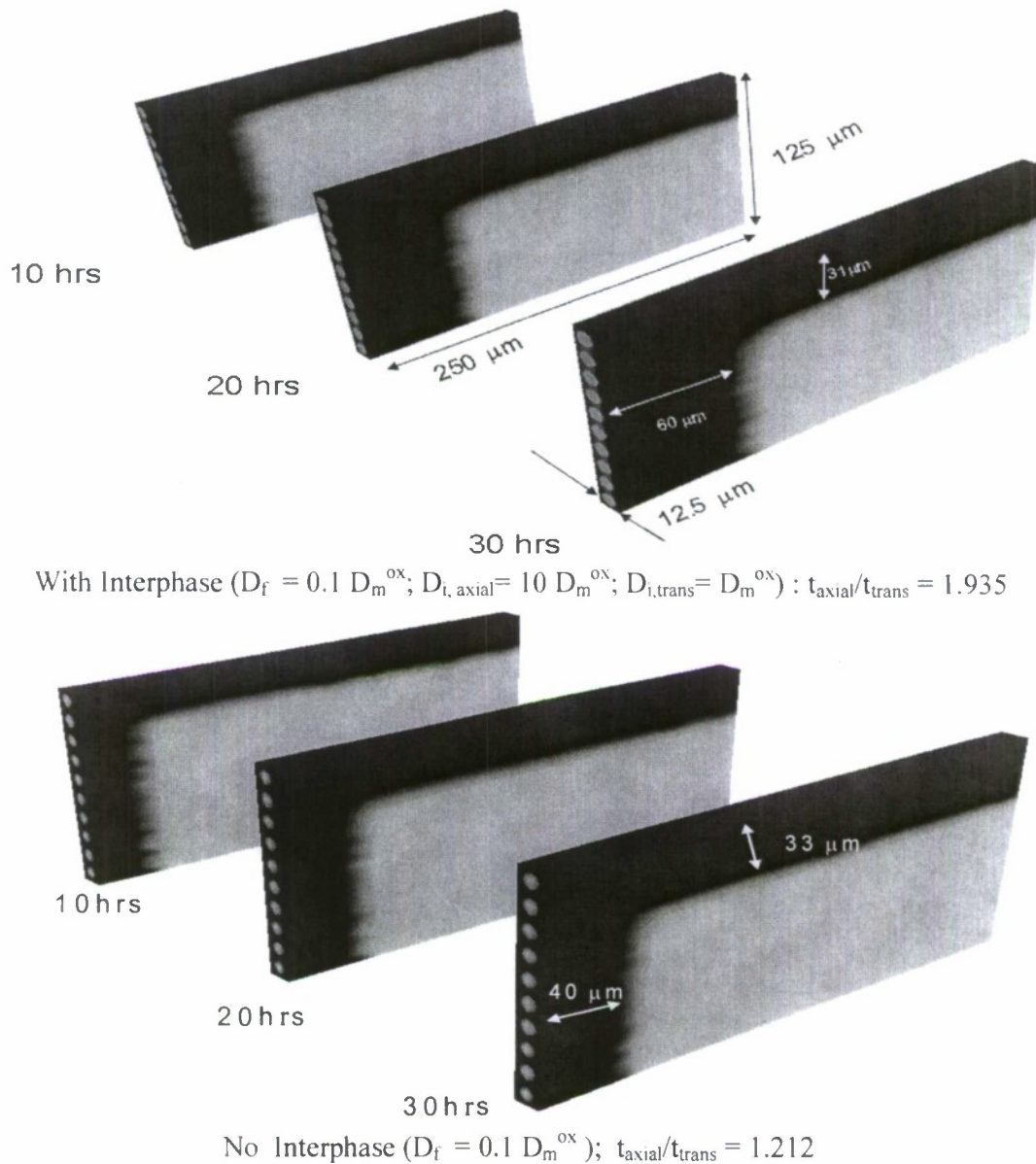


Figure 26 Effect of a highly diffusive fiber-matrix interphase region. The anisotropy in the oxidation layer can be clearly seen

the diffusivity factor obtained from the homogenization method closely matches the observed anisotropy in the oxidation layer sizes. However for larger ratios of D_f/D_m (i.e., >10), the oxidation process is observed to become reaction rate limited as the reaction zone ratio also increases with increasing D_f/D_m ratio. The oxidation layer ratio t_{axial}/t_{trans} therefore is calculated to be less than the corresponding D_1/D_2 diffusivity factor since oxidation is not occurring as rapidly as the rate at which oxygen is being supplied. Hence a larger portion of the surface layer now has regions in which complete oxidation has not occurred, leading to an increase in the size of the "active" reaction zone.

To investigate the role of the interphase region, particularly if the interphase thickness and its diffusivity are large, a study is conducted to understand the influence of the interphase parameters on the oxygen diffusivity and transport in the composite. This is accomplished by extending the RVE analysis to include a finite thickness interphase layer. The interphase layer is assumed to be a concentric cylinder with that of the fiber with a thickness of 5% that of the fiber radius. We assume the fiber diffusivity to be isotropic and set it equal to $0.1 D_m^{ox}$, while the diffusivity of the interphase is assumed to be anisotropic, with axial diffusivity $D_{i,axial} = 10 D_m^{ox}$ and transverse diffusivity $D_{i,trans} = D_m^{ox}$. Figure 26 shows the comparison of the oxidation layer growth within an RVE which includes the interphase with another RVE in which no interphase is present at various time intervals (10, 20 and 30 hours). Clearly, the presence of a highly diffusive interphase region contributes to an increase in the oxidation layer growth transverse to and in the fiber direction. The evidence of higher diffusivity in the axial direction compared to that in transverse direction can also be found in the sizes of the active reaction zones.

5.2.7.4 Modeling Oxidation Induced Stress and Deformation

The following three main assumptions were made to establish the shrinkage strain in inert (non-oxidizing) and air (oxidizing) environments. It is first assumed that the shrinkage of the specimen aged in argon is representative of the shrinkage in the interior (unoxidized) region of the specimen undergoing oxidation. Secondly, we assume that the oxidized layer has uniform shrinkage and that it does not depend upon concentration of the absorbed oxygen. Thirdly, we assume that there is no erosion loss of material from the surface of the specimens. It has been documented that for long aging times, the oxidation layer thickness remains constant, i.e., the thickness versus aging time reaches some asymptote. This doesn't mean that the oxidation front is stationary, but it may imply that the rate of erosion from the surface of the specimen is equivalent to the oxidation layer growth. Therefore, the shrinkage model is not applicable for long aging times when erosion becomes significant.

Table 5 shows the rate of volumetric shrinkages computed from volumetric shrinkage in Argon and oxidative environments. Subtracting these two volumetric shrinkage rates, the oxidation-caused shrinkage is 0.00254%/hr at 288°C. We set the simulation window to 200 hours wherein the surface erosion is not significant. The total volumetric shrinkage computed at 200 hours for non-oxidized regions are taken as 0.152% and the oxidized region to be 0.66%. The value used for the oxidized zone consists of both the inert shrinkage contribution and the oxidation-induced shrinkage. The isotropy of the shrinkage assumption leads to the definition of the volumetric shrinkage in a unit elemental volume as $\epsilon_v = (1+\epsilon_\lambda)(1+\epsilon_\lambda)(1+\epsilon_\lambda) - 1 = \epsilon_\lambda^3 + 3\epsilon_\lambda^2 + 3\epsilon_\lambda$, where ϵ_λ is the lineal shrinkage strain. Solving for ϵ_λ from known ϵ_v , we get the lineal shrinkage strains to be 0.0005 (0.05%) and 0.0022 (0.22%) for un-oxidized ($\phi=1$) and oxidized zones ($\phi=\phi_{ox}$), respectively. The oxidation causes an increase of 0.17% strain compared to that induced by inert environments. The total lineal shrinkage strains for a material point with an

Table 5 Total volumetric shrinkage observed for PMR-15 at elevated temperatures

Temp	Air %/hr	Argon %/hr
343°C (650°F)	-0.023	-0.0075
288°C (550°F)	-0.0033	-0.00076

oxidation state of ϕ are obtained by interpolation of shrinkage strains for oxidized and unoxidized materials.

The modulus of PMR-15 is sensitive to the temperature and oxidation state. Test data reveals that the resin is stiffer in compression, and that the compressive modulus of unaged PMR-15 resin decreases from 4.72 GPa to 3.39 GPa due to temperature rise from 25°C to 288°C. Nano-indentation was used to determine the room temperature (RT) modulus of the oxidized specimens. Nano-indentation data show that the stiffness of the oxidized resin is higher than that of the unoxidized portion of the sample. The data show that the unoxidized resin has a room temperature modulus of 4.84 GPa and the oxidized resin a modulus of 5.84 GPa. Thus, there is a small discrepancy between the values obtained from the bulk testing (4.72 GPa at RT) and those obtained from the nano-indentation (4.84 GPa) for the unoxidized resin. This small discrepancy could be attributed to some pile-up observed in PMR-15 specimens during nano-indentation leading to contact areas that are greater than the cross-sectional area of the indenter at a given depth, and hence a larger apparent modulus measurement.

In order to model the temperature (T), oxidation state (ϕ) and time dependence of the modulus, we use the framework suggested by Wise, et al.[7],

$$E(\phi, T) = E_{un}(T) e^{(K_{ox} \frac{1-\phi}{1-\phi_{ox}})} e^{(K_{nox} \frac{\phi-\phi_{ox}}{1-\phi_{ox}} t)} \quad (18)$$

where $E_{un}(T)$ is the unaged resin modulus at temperature T. The modulus of the oxidized resin at any temperature is given as in Equation (18). Two constants, K_{ox} and K_{nox} , are assumed to be temperature independent and are obtained from room temperature nano-indentation results. K_{ox} represents the oxidation state (ϕ) dependence and K_{nox} controls the aging time (t) dependent modulus changes. It is seen that the modulus of the resin is stable and does not change with the aging time in an inert environment. Therefore, K_{nox} is set to zero and $K_{ox} = 0.1878$ is obtained.

As the nano-indentation data were not obtained at elevated temperatures, the bulk specimen data is used for the temperature-dependent modulus of the un-oxidized resin. Obtaining the modulus of the oxidized resin through bulk mechanical testing is extremely challenging. Therefore, a mixed set of parameters is used to determine the temperature-dependent modulus of the oxidized resin. The K_{ox} value is determined from nano-indentation data and the same value is used with the modulus data obtained with bulk

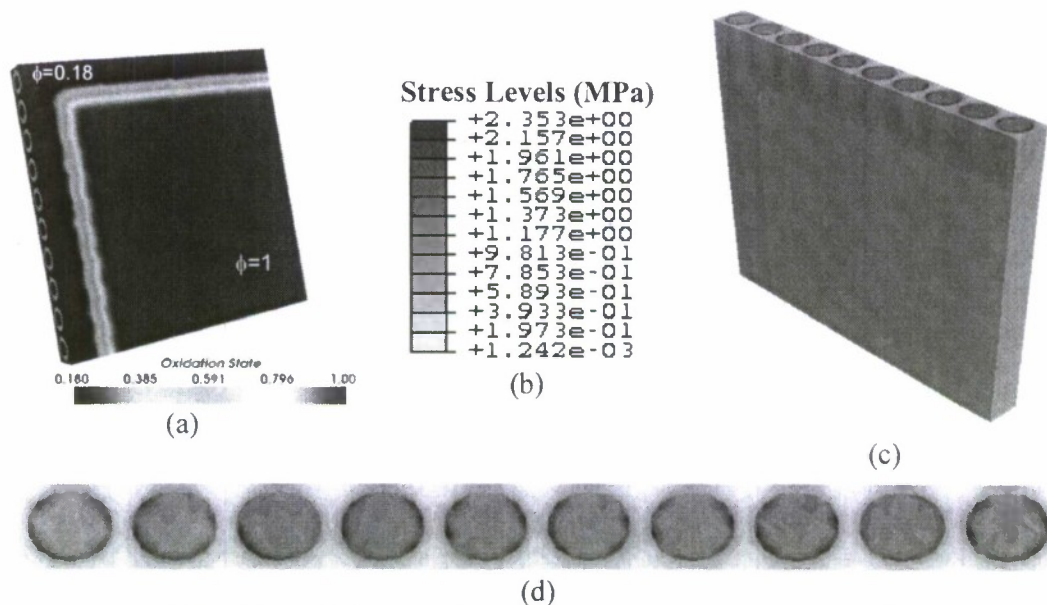


Figure 17 (a)-(d): Oxidation state and effective stress distributions after 10 hours of oxidative aging

mechanical testing at higher temperature. With this assumption, it is determined that the modulus of the oxidized resin is 4.09 GPa at 288°C. Significant shrinkage strains are induced due to thermo-oxidation in the resin, and with the fiber assumed to be relatively dimensionally stable during oxidation, substantial amount of stresses develop in the HTPMCs. As the shrinkage strains and the oxidation state dependent modulus have been characterized earlier, the evolution of the deformation, strain and stress fields are next determined during thermo-oxidative aging.

Figure 27 (a) shows the simulated oxidation state in a G30-500/PMR-15 composite. The picture frame oxidation layer growth is shown after 10 hours of exposure. Finite element analysis is conducted to determine the deformation and stress. The model is subjected to symmetry boundary conditions on the unexposed surfaces, and the surfaces exposed to oxygen are specified as stress free. No mechanical loading is applied to the RVE. The oxidation state variable (ϕ) at each material integration point in the stress analysis mesh is used to compute the appropriate modulus (Equation 18) and shrinkage strains induced due to thermo-oxidation are determined earlier. Figure 27 (c) and (d) show the Von-Mises effective stress distribution in the RVE with the corresponding grey-scale bar shown in Figure 27 (b). The figure shows stress concentrations at the fiber-matrix interface regions and in the interstitial regions between the fiber and matrix. The peak stress is seen at the fiber-matrix interface and at the free edge where a stress singularity is expected. The approximate average stress in the fiber after 10 hours is 1.4 MPa, and the interstitial matrix regions have stresses on the order of 0.4 MPa, while the peak stress is 2.4 MPa.

5.2.8 Thermo-oxidative Aging of Carbon Fibers

The effects of service temperatures and oxidation on the mechanical properties of high-temperature polymer composites is primarily manifested in the polymer-dominated properties, namely, the transverse properties (perpendicular to the fiber direction) and the shear properties. However, the fiber-dominated properties may be affected by degradation of the fiber and deterioration of the fiber-matrix interface. This may be particularly true for composites with glass fibers [8] in which magnesium and sodium can leach out from the fiber and possibly contribute to polymer/interface degradation. It is reported that graphite fibers containing significant amounts of sodium and potassium as contaminants are less thermo-oxidatively stable than graphite fibers with very low alkali metal contents [9,10]. Studies conducted by Bowles and Nowak [4] indicate that extreme oxidative erosion of the Celion 6000 graphite fiber occurs at elevated temperatures in the presence of the polyimide matrix. Bowles [11] has revealed the effects of different fiber reinforcements on thermo-oxidative stability of various fiber-reinforced PMR-15 composites. The ceramic Nicalon and Nextel fibers were found to drastically accelerate thermal oxidation of the corresponding composites because of the active fiber-matrix interface. Compared to polyimide matrices, reinforcing carbon fibers [12] are usually far more stable at the elevated temperatures considered. Studies conducted by Wong, et al. [13] indicate that IM6 carbon fibers are more stable than the G30-500 fibers within the first 600 hours during thermal oxidation at 371°C. The oxidation rate of the IM6 fibers then increases substantially, leading to complete decomposition of the fibers during the final stage. The sudden increase in the oxidation rate in the IM6 fibers implies the possibility of additional degradation mechanisms, such as different carbon molecule structures, increase in microcracks or micro-pores, and different levels of impurity content.

The three polyacrylonitrile (PAN)-based carbon fibers of interest to the present body of work are two low modulus carbon fibers, namely, T650-35 and G30-500, that are typically used in HTPMCs, and one intermediate modulus carbon fiber, namely, IM7. Recently, isothermal aging studies were conducted [14] on these three types of fibers to study their oxidation behavior. Both sized and unsized fibers were exposed to different elevated temperatures for varying time periods, in an attempt to understand the influence of the fiber sizing/coupling agent on their thermo-oxidative stability. Note that aging of the bare fibers may not necessarily be representative of the behavior of the in-situ fibers embedded in the matrix because the exposed surface area of the fibers in the composite is only a very small percentage of the total surface area of the fibers. Thermal degradation is quantified by the amount of weight loss measured, while degradation of mechanical properties was measured using single filament tests on unaged and aged fibers. Finally surface morphology changes were monitored in an attempt to relate physical and surface changes to the knockdowns in mechanical performance as a function of aging.

5.2.8.1 Fiber Weight Loss Studies

Figure 28 shows that the thermal degradation (as measured by weight loss) of unsized T650-35 carbon fibers is substantial for moderate temperatures above 316°C. It is seen that there is a large (~ 40 %) weight reduction of T650-35 carbon fibers after 2000 hrs of aging at 343°C. At the lower temperature of 232°C, the weight loss is not significant, and

the weight loss as a function of time follows approximately a linear relationship. However, as the aging temperature is increased to 343°C, the T650-35 fibers are observed to lose weight rapidly. There seems to be a change in slope in the weight loss curve at around 750 hours of aging possibly signifying a change of degradation mechanism. Typically, the weight loss data for neat polymer specimens is normalized with respect to the specimen surface area, since oxidative weight loss occurs through the exposed surfaces and edges of the specimen. Note that carbon fibers have an extremely large surface area due to their small diameter (typically 4 to 8 μm) and large aspect ratio (typically > 1000). Figure 29 shows a comparison of the normalized weight loss of T650-35 carbon fiber and PMR-15 neat resin at 343°C. Note that the normalized fiber weight loss is almost negligible compared to that of neat resin over the entire 2000 hours of aging time. Thus, even though the carbon fiber loses a significant weight fraction with aging at elevated temperatures, the weight loss normalized by the fiber surface area is negligible compared to that of the resin. Weight loss studies on sized fibers [14] further indicates that the sizing/coupling agent is released within a short time period (~ 24 hrs) of aging beyond which the weight loss trend is similar to the corresponding unsized fibers.

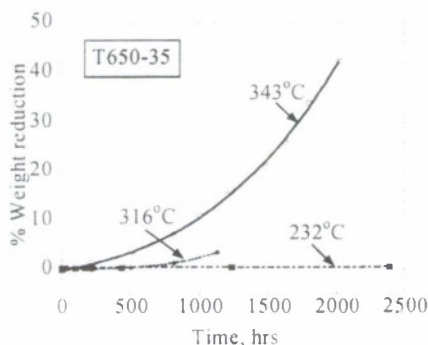


Figure 28 Weight loss of T650-35 carbon fiber as a function of aging temperature

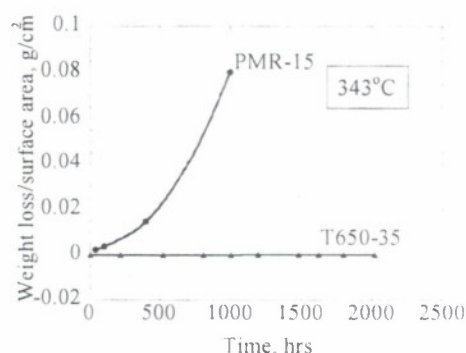


Figure 29 Normalized weight loss of T650-35 fiber and PMR-15 resin

5.2.8.2 Fiber Mechanical Properties

Single fiber specimens were tested at room temperature in tension using the single filament test. Figures 30 and 31 show the normalized failure strength and failure strain, respectively, of unsized T650-35 carbon fibers aged at 343°C. The strengths and failure strains are normalized with respect to their corresponding unaged values, such that the observed decreases are a reflection of the reduction resulting from isothermal aging. A minimum of 10 fibers were tested for each condition considered, and the standard deviation is shown as the error bar across the measured mean values. There is some scatter in the strength and failure strain data which is typically encountered in single fiber testing as failure is sensitive to the presence of flaws over the fiber gage length. Fibers aged at the elevated temperature of 343°C show a large decrease in the strength after 1000 hours of aging. The significant decrease in mechanical strength signifies that the carbon fibers should not be treated as static entities when composites containing these fibers are aged at this temperature for extended periods. However, the reported data are a worst case scenario in which all surfaces of the fibers are exposed during aging. In-situ

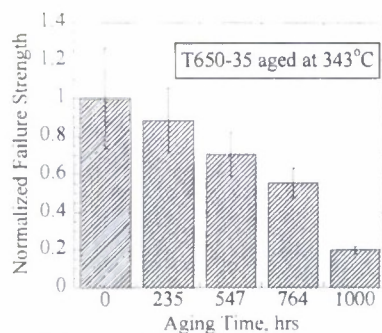


Figure 30 Normalized strength of unsized T650-35 carbon fibers aged at 343°C

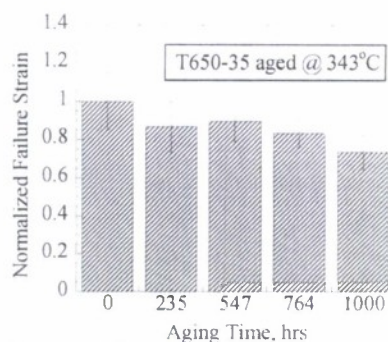


Figure 31 Normalized failure strain of unsized T650-35 fibers aged 343°C

fibers of the composite have only a small fraction of their total surface area exposed to the oxidizing environment, and should therefore suffer less degradation. Further, test data from single filament testing [14] indicates that application of fiber sizing may result in an improved performance of the carbon fiber in the unaged condition but could result in some loss of mechanical performance after aging at elevated temperatures. Failure is sensitive to the presence of flaws, and it is likely that the sizing/coupling agent on the fiber helps to decrease the influence of the fiber surface flaws resulting in a slightly superior performance in the unaged condition.

5.2.8.3 Fiber Surface Characterization

Scanning electron microscope (SEM) microstructural studies were conducted to determine the carbon fiber surface morphology changes during long-term isothermal aging. Figure 32(a) compares the SEMs of unsized T650-35 carbon fiber in the unaged condition with that of the fiber aged for 1052 hours at 343°C in Figure 32(b). No significant visible damage or surface morphology changes are observed, although some minimal amount of pitting is visible on the previously smooth fiber surfaces after 1052 hours of aging. Thus, the fiber surfaces provide little indication of the deterioration in the mechanical performance of the aged fiber.

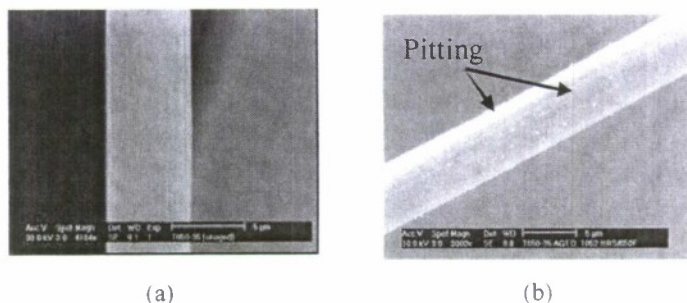


Figure 32 SEMs showing surface morphology of unsized T650-35 carbon fibers in (a) the unaged condition, (b) aged for 1052 hours at 343°C

5.2.9 Monitoring of Oxidation Induced Fiber/Matrix Debond Propagation

The anisotropic nature of oxidation in high-temperature polymer matrix composites is primarily a surface reaction phenomenon controlled by the diffusion and rate of reaction of oxygen with the material so that surfaces with different microstructural characteristics are expected to exhibit different oxidation behavior. The oxidation process is generally limited by the amount of oxygen that can diffuse into the material and react with the polymer rather than limited by the rate of reaction of oxygen with the polymer. The diffusion limited oxidation behavior of polymer matrix composites is predominantly controlled by the properties of the resin and the fiber-matrix interface and the total surface area through which the oxygen can diffuse. Various factors may lead to the preferential oxidation [15] along the fiber paths. Resin cure shrinkage and mismatches in the coefficient of thermal expansion of the fibers and matrix during the composite cure process give rise to localized micromechanical residual stresses in the fiber-matrix interphase region. In this work, unidirectional G30-500/PMR-15 composite specimens are aged at elevated temperature in air resulting in oxidation propagation parallel and perpendicular to the fibers. The observed anisotropy in composite oxidation is explained by carefully monitoring the development and growth of damage in composite specimens through the use of fluorescence imaging using dye impregnation in conjunction with optical microscopy. Optical micrographs are taken on polished internal sections and viewed in the dark-field mode to measure the degree, depth and distribution of thermal oxidation development from external surfaces perpendicular and parallel to the fibers. It is shown that alternative pathways for transport of oxygen into the interior of the composite are fiber-matrix debonds that propagate with the oxidation front, with the oxidation front consistently preceding the debond crack front.

A series of photomicrographs of aged specimens containing the fluorescent dye were taken for aging times up to 3112 hrs. Figure 33 shows a cross section of the 16-ply unidirectional specimen after 96 hrs of isothermal aging at 288°C. The dark-field image micrograph on the left shows a thin oxidation layer on the surfaces exposed during aging. For PMR-15 neat resin and composite specimens, oxidation causes a slight change in the grayscale color of the polymer. The fluorescent dye image on the right side of Figure 33 shows short fiber matrix debonds along the 0° fiber direction. Experimental evidence suggests that these debond cracks will continue to increase in length while new cracks continue to develop at the free surfaces of the specimen. It is observed as illustrated in the series of micrographs in Figures 34 and 35 for aging times of 668 hrs and 2584 hrs, respectively, that the debond crack lengths and the extent of oxidation increase for increasing aging time. Note in Figure 34 that there appears to be a broad distribution of crack lengths implying that new debond cracks are forming as aging time is increased. It is presumed that the longest of the debond cracks correspond to the free-edge cracks that formed first on the specimen. The difficulty in measuring the extent of oxidation and quantifying the debond cracks is illustrated in Figure 35. The left image showing the oxidation reveals that the oxidation front is highly nonuniform, and the oxidation has advanced to a greater extent in the midplane region of the specimen corresponding to the location of the debond cracks.

The right image of Figure 3 indicates that for long aging times, the nature of oxidation-induced cracking has changed from individual fiber-matrix debond cracks to a coalescence of oxidation damage. It appears that the surfaces of the debond cracks have oxidized, thereby widening the crack. The fluorescence image shows a large region in the interior of the specimen in which presumably all of the polymer phase of the composite has been oxidized. Whereas documentation of the number and length of the debond cracks is unambiguous for short aging times, for long aging times at which cracks interact and coalesce, it is not clear how to rigorously quantify the oxidative cracking damage.

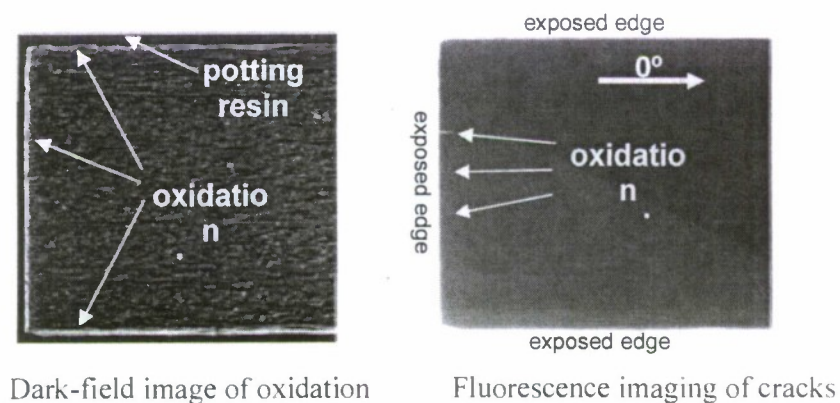


Figure 33 Cross section of 96-hr aged specimen

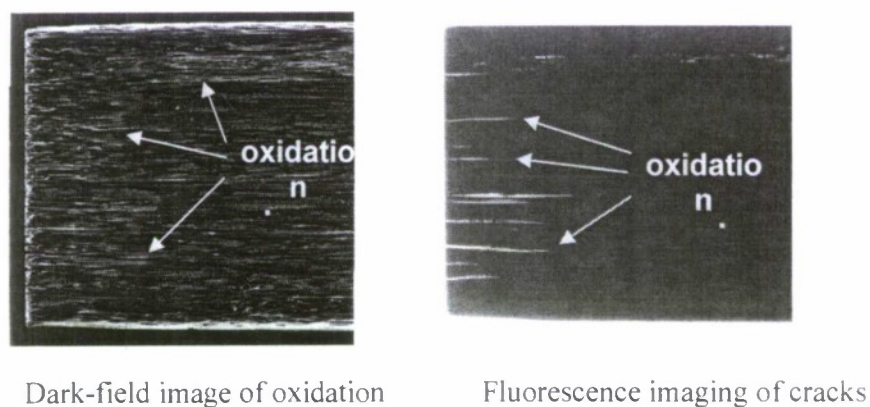
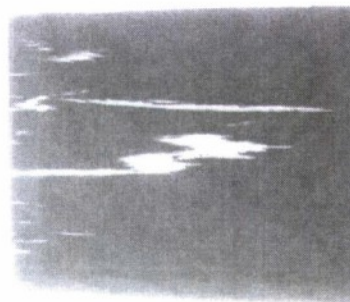


Figure 34 Cross section of 668-hr aged specimen



Dark-field image of oxidation



Fluorescence imaging of cracks

Figure 35 Cross section of 2584-hr aged specimen

It is shown that alternative pathways for transport of oxygen into the interior of the composite are fiber-matrix debonds that propagate with the oxidation front. It has been further determined through examination of the oxidation front and the debond crack front for discrete regions of the specimens, that the oxidation front consistently precedes the debond crack front. This mechanism for accelerated oxidation along the composite fiber direction is an excellent example of the intrinsic coupling of chemical oxidative aging and damage. Whereas cracks can accelerate oxidation by providing pathways for oxidants, so can oxidation lead to cracking in the resin matrix and at fiber-matrix interfaces. The critical nature of the fiber-matrix interphase on degradation and failure processes in composites signifies the importance of proper representation of its behavior in predictive models. Since failure initiation is typically associated with the fiber-matrix interface/interphase region, the importance of modeling the coupling effects of damage and oxidation cannot be over emphasized.

5.2.10 Validation of Nanoindentation Measurements for Non Flat Surfaces

The effect of polishing time on measured oxidation thickness and elastic modulus of isothermally aged PMR-15 neat resin was investigated. Specimens aged for 956 and 1556 hours in ambient air at 288°C (550°F) were selected for this study. They were polished at consecutive time periods from a quick polishing to extensive polishing. A white light interferometer was used as a surface profiler to measure height variations from the specimen edges into the interior of the material. Subsequently, optical microscopy and nanoindentation experiments were conducted to correlate observations of oxidation thickness and elastic modulus measurements with polishing time. The modulus profiles obtained from nanoindentation experiments indicate formation of an outer brittle layer followed by a sharp drop in the transition region to the unoxidized interior. During the course of the study, it was observed that surface profiles of PMR-15 resin specimens were not flat after being polished. Material near specimen edges was polished to a higher degree than the interior material. Concerned that the specimen surface profile might affect the oxidation thickness measurements, the effect of polishing time on the measured

oxidation thickness and elastic modulus of isothermally aged PMR-15 neat resin specimens was investigated and is reported here. The maximum variation in the surface profile is limited to 5-6 micrometers across the oxidation layer (~175 micrometers), which results in a slope of $\sim 1-2^\circ$ over the oxidized region. Optical measurements of thickness of oxidized layer and transition region are in good agreement with the depth and modulus profiles obtained using the interferometer and nano-indenter, respectively. Results from three techniques show that the measured oxidation thickness and elastic modulus are independent of the amount of polishing time.

A white light interferometer is an optical microscope with a parallel mirror interferometer below the objective lens. It is a non-contact, optical technique for measuring surface height and shape with great speed and accuracy. White light passes through a beam splitter, which directs light to the sample surface and a reference mirror. Light reflected from these two surfaces combines to produce interference fringes. Maximum fringe contrast occurs at optimal focus. White light interferometry allows one to obtain 3D images of the 1556hr aged PMR-15 specimen, as seen in Figure 36. Areas around the sample edges (seen in blue) are lower than the interior of specimen.

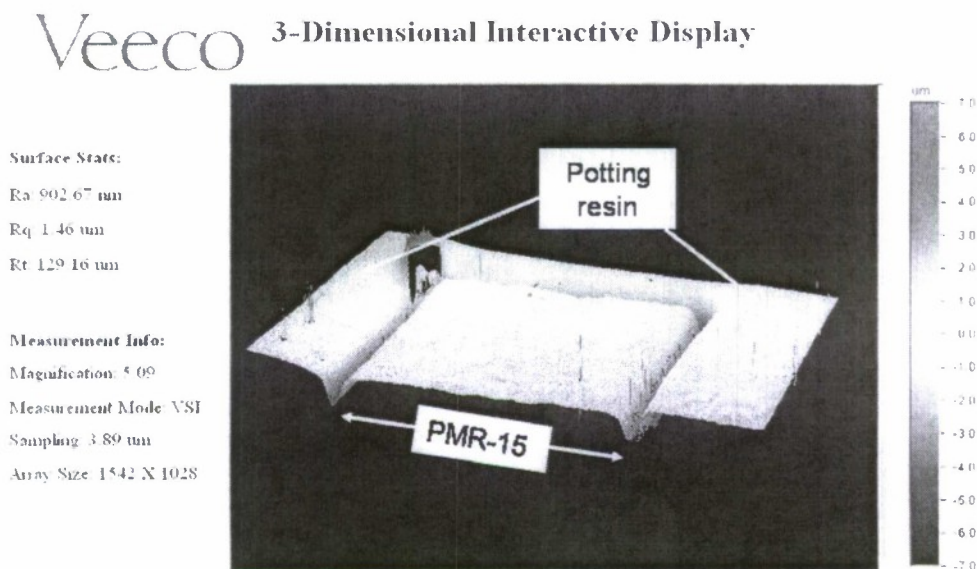


Figure 36 3D image of the 1556hr aged PMR-15 specimen

Figure 37 shows a 2-D image of a 1556 hr aged PMR-15 specimen. Line scans were conducted along the horizontal and vertical directions, as indicated by the X-scan and Y-scan lines.

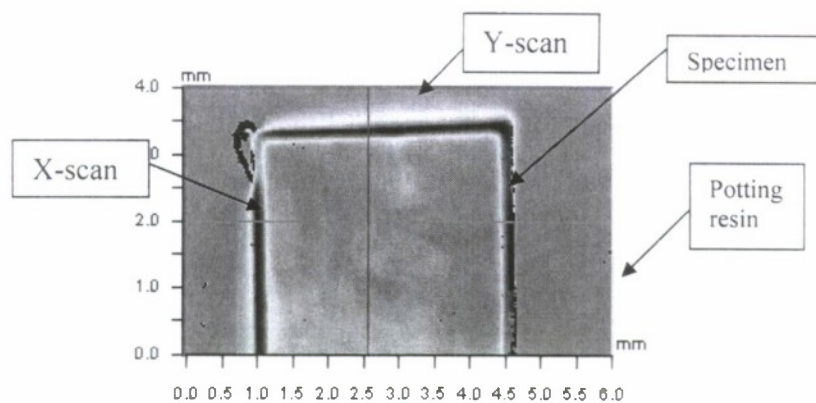


Figure 37 2-D image of a 1556 hr aged PMR-15 sample

Nanoindentation experiments were performed to examine the influence of specimen surface topography on the elastic modulus. Experiments were performed by first focusing in the middle of the oxidized layer near the specimen outer edge and traversing to the interior of the specimen. Alternatively, focusing was done in the unoxidized interior of the specimen and traversing to the outer exposed edge of the specimen. Observations/results from the study are listed here:

- Measurement of surface profiles using a white light interferometer indicates that the maximum variation in depth is limited to 6 micrometers across the thickness of the oxidation layer (~175 micrometers), which results in a slope of $\sim 2^\circ$ over the oxidized region.
- For specimens with uneven surfaces, the measured elastic modulus values are independent of the choice of initial focus point. There is some local variation due to heterogeneity of the oxidation process.
- The modulus profiles indicate formation of an outer higher modulus layer followed by a sharp drop of modulus in the transition region to the unoxidized interior.
- Optical microscopy measurements of thicknesses of the oxidized layer and transition region are in good agreement with the depth and modulus profiles obtained using the profilometer and nanoindenter, respectively.
- All three techniques yield experimental data to support that the measured oxidation thickness and elastic modulus are independent of the amount of polishing time. .

5.3 Determination of Fiber Architecture Effects on Crack Development

The high temperature degradation mechanisms described and analyzed above for both neat polymer and fiber matrix composite systems lead to, and are also dependant upon, the development of a network of cracks that act as conduits for the transport of oxygen consumed by the thermal oxidative processes. In prior AFOSR funded work an

automated image analysis technique was developed that allows fiber center data from real microstructures to be rapidly collected over a wide range of length scales. This provides data for the application of a Dirichlet Tessellation process that allows fiber volume fraction data to be developed for real composites with various fiber packing characteristics. The fiber center data is also used to form the basis of an automated Finite Element Grid Generation process that allows the impact of fiber arrangements on stress profiles within loaded composites to be determined. This latter facility will be crucial in predicting the concomitant effects crack pattern generation.

5.3.1 Automated Finite Element Analysis

The automated image analysis software was applied to a number of examples of microcracked composites, both from laminates made and tested in the course of this and the prior study and legacy images taken from published articles. Figure 38 shows a YLA prepreg laminate fabricated by autoclave molding. The micrograph shows the central ply of a $(0/90)_{25}$ laminate that was pulled in tension (along the horizontal axis as shown) until the onset of transverse ply cracking.

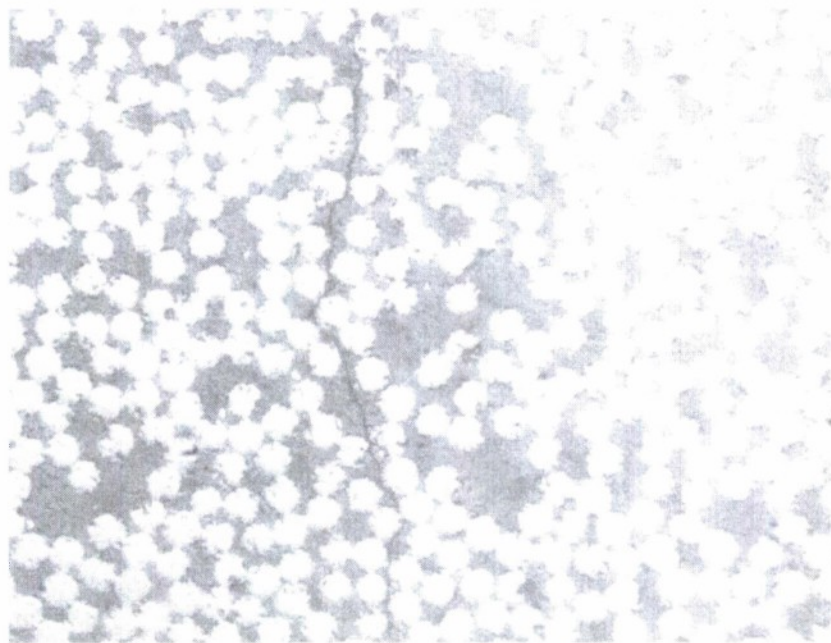


Figure 38 Central ply of a $(0/90)_{2S}$ laminate tested to onset of microcracking

The fiber centers and associated Voronoi cells (yielded by the Dirichlet tessellation) for this image are shown in Figure 39. Note that the fiber center identification accuracy is in this case 100%, and therefore the resultant fiber volume fraction mapping would also be expected to be similarly accurate. Figure 40 shows the mapping for this microstructure with the crack path highlighted in red for clarity.



Figure 39 Fiber centers and associated Voronoi cells for laminate shown in Figure 38.

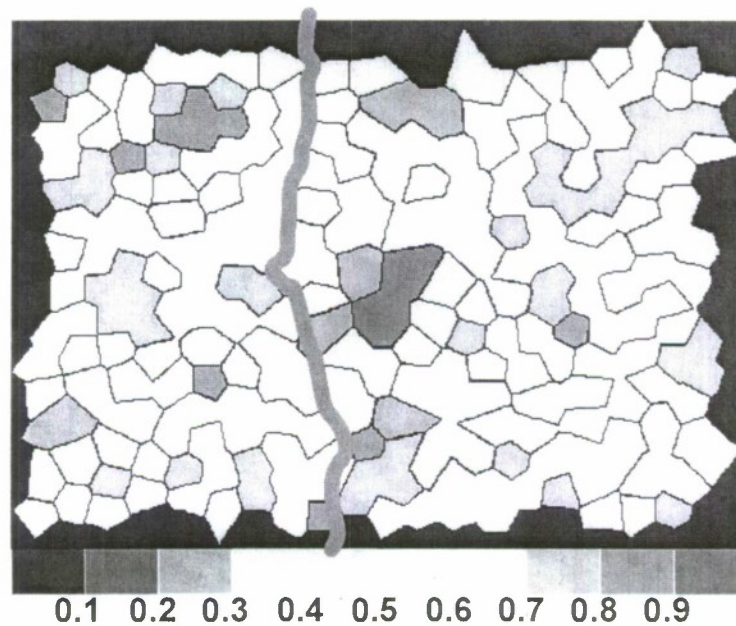


Figure 40 Fiber volume fraction map for micro-cracked composite laminate made from YLA material

Visual inspection of the fiber volume fraction map suggests that the crack path follows the generally low fiber volume fraction regions, but more importantly it seems that it is close to the region in which the fiber volume fraction *gradient* is greatest. Figure 41

shows the same data presented in Figure 40 but with a plot of fiber volume fraction gradient over the horizontal red line shown for illustration. This is a typical effect seen repeatedly using the fiber volume fraction mapping facility where local crack paths have a tendency to follow regions of high fiber volume fraction gradient.

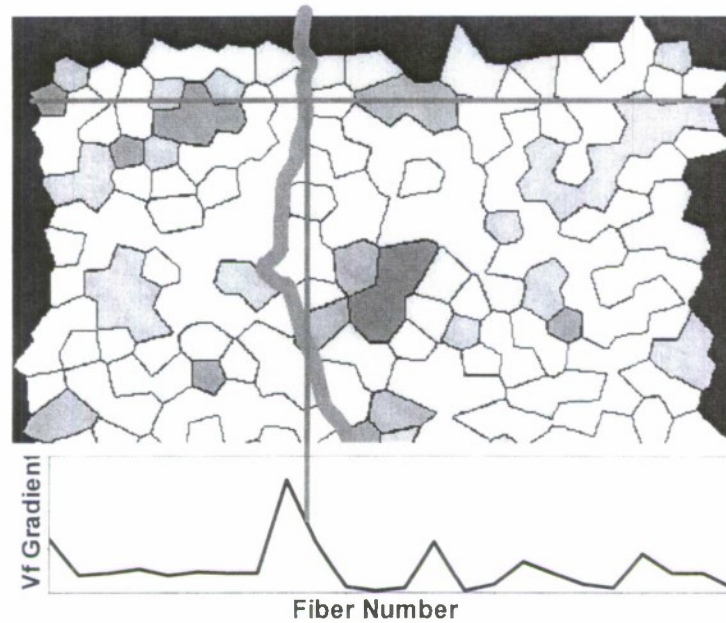


Figure 41 Fiber volume fraction map showing gradient plot across a selected horizontal line



Figure 42 Fiber centers as transferred to FEA Mesh Generator

A finite element analysis technique based on the Dirichlet tessellation approach was developed to analyze the performance of composites laminates with various fiber distributions. Analyses were completed at the fiber diameter scale to investigate fiber positioning contribution to structural performance. This effort was focused on extension of the previous analysis technique coupled with development of FEA models of actual measured fiber distributions from as-fabricated laminate specimens. The automated image analysis software utilizes the Dirichlet tessellation to generate a FEA mesh of the measured fiber locations in a 2-D plane strain laminate cross-section. The developed FEA models were used to predict the stress / strain distributions through the composite for varying fiber distributions and load conditions.

Micrograph data were acquired for as-fabricated laminate samples which had been tested to micro-crack initiation. The microstructure used to initiate development of this capability is shown in Figure 38. The center point of each fiber is calculated using topographical imaging of the fiber micrograph, and a baseline Voronoi cell set for the test data is generated to estimate fiber volume fraction. Figure 39 shows the calculated fiber centers and Voronoi cells for the micrograph shown in Figure 38.

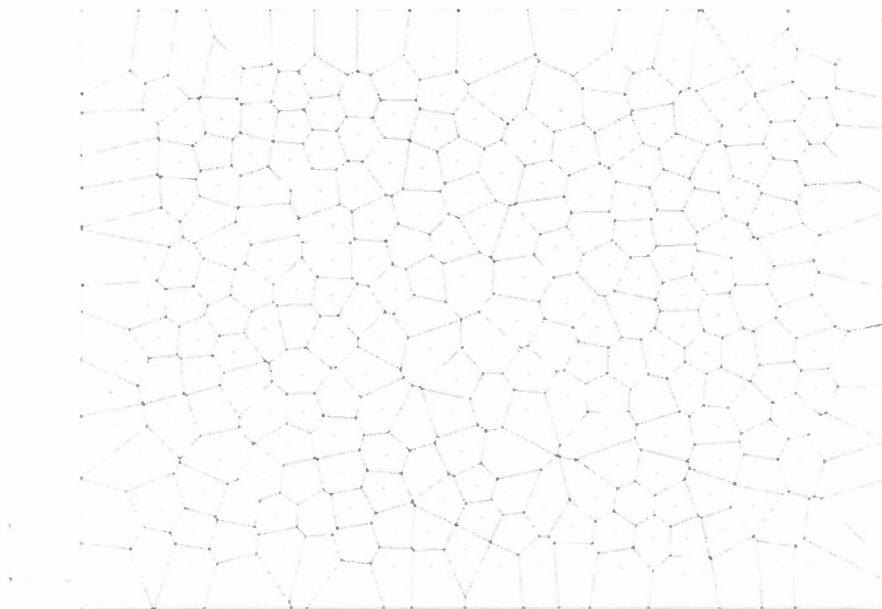


Figure 43 Voronoi Cell Tessellation as calculated by FEA Mesh Generator

The FEA models are generated by reconstructing the Voronoi cells for the measured data, and subsequently developing a fiber mesh and matrix mesh within each cell. The Voronoi cells are recalculated for the FEA mesh generation rather than using the test data calculated cells directly, since the Voronoi boundary edges must be generated specifically for the FEA mesh. The minimum distance between a fiber diameter and the model boundary edge is a mesh generation variable.

The Voronoi cells are determined by connecting the perpendicular bisector of line segments which connect adjacent points. This tessellation has the following characteristic properties, which follow from the definition of the Voronoi cells:

- Every Voronoi cell has at least three vertices
- The vertices of a Voronoi cell form a convex hull around the center
- Every vertex of a Voronoi cell lies midway between the two centers of the adjacent Voronoi cells
- All points within the area bounded by a Voronoi cell are closer to the Voronoi cell center point than any other center in adjacent Voronoi cells

Figure 42 shows typical fiber center points which are transferred from the measured data to the FEA mesh generator. Figure 43 shows the FEA model Voronoi cell configuration which is generated by the automated mesher. The interior region of the cell definition is identical to the test data of Figure 39, while the boundary edges have been defined by the model generator to develop a total FEA mesh. The FEA elements are developed by defining a fiber mesh at each fiber center and filling the remainder of the Voronoi cell with matrix material (see Figure 44). The fiber diameter is a program variable. The FEA

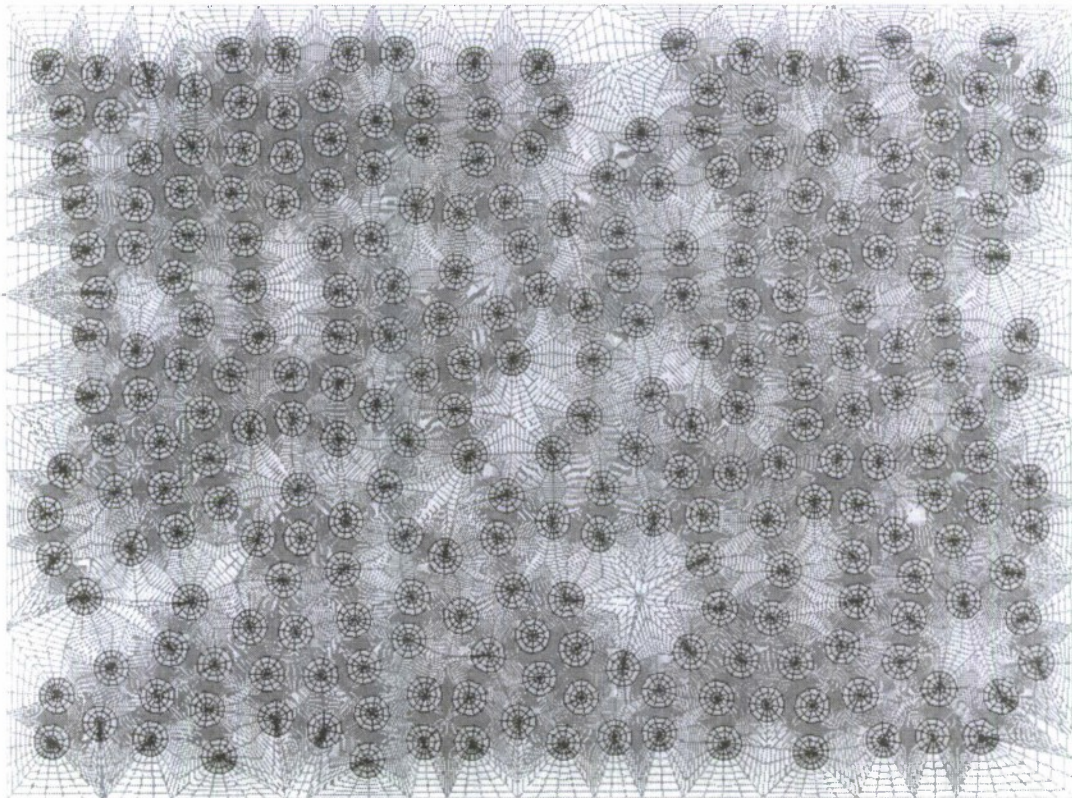


Figure 44 Sample FEA mesh, as generated by automated FEA mesher

mesh is developed using quadrilateral plane strain elements. The mesh generation logic can be simplified if triangular elements are used for the automated mesh generation, but the quadrilateral elements are superior to triangular elements for stress and strain predictions. The only triangular elements in the automatically generated FEA mesh are at the extreme fiber centers. Mesh density can be varied in the radial and tangential directions for each fiber and Voronoi cell. Additionally, the mesh generation program logic makes additional meshing decisions based on minimum element sizes, acceptable element shapes, and mesh gradients between neighboring cells.

Analyses were conducted using the developed models to predict sample failures and correlate to measured data. Figure 45 shows a typical FEA result for strain predictions with a uniform edge load applied to the sample. Figure 46 shows typical results for stress predictions for the same mesh. The stress and strain contours are shown to vary with relative fiber position, with higher local strains in regions where the random position of the fibers is preferentially aligned with the load direction. Evaluation of these types of stress results was completed as model correlation data became available (see section on Digital Image Correlation).

In addition to the strength based results of Figure 45 and Figure 46 fracture analyses have been completed with the FEA models to predict crack growth across the laminate. Preliminary data showed numerically biased results which predict crack growth along the largest element sides. Additional optimization of the automated meshing routines was completed to better configure the meshes for crack propagation analyses.

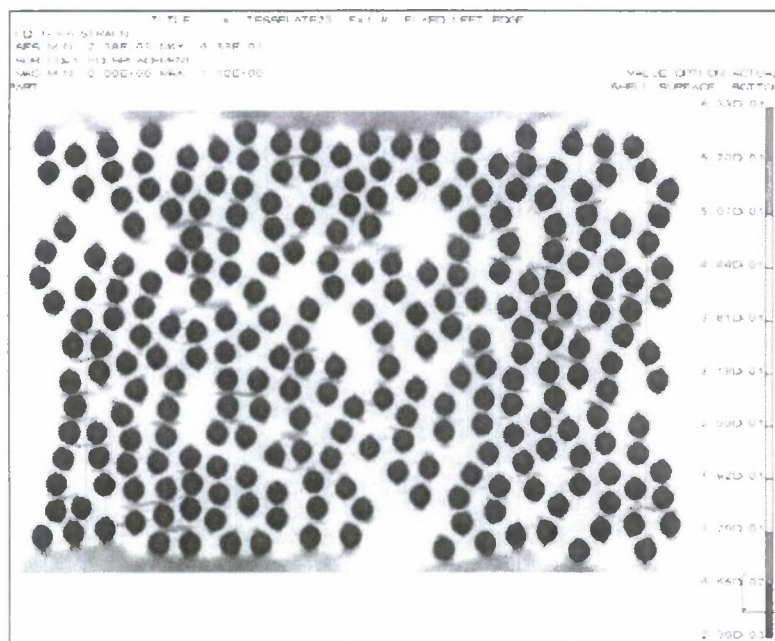


Figure 45 FEA model, predicted strain, uniform edge load at right side of specimen

imaging techniques was completed and this provided time domain displacements of individual fibers for a sample under continuously increasing edge load. The model results were correlated to these results to improve the viability of the model for strength and fracture based failure predictions.

Algorithms were successfully developed to automatically generate FEA meshes using measured fiber centers of a composite laminate specimen. The FEA models were utilized for predictions of stress, strain, and displacement of sample specimens with specific fiber locations and uniform edge loads. Analyses of crack growth predictions were also investigated, although additional optimization of the FEA mesh is required to improve these predictions. The developed technique provides a new tool for investigation of the contribution of subscale fiber structure to macro composite strength.

The development of the automated mesh generation tool described above is believed to represent a major contribution of this research. This capability, which has been integrated with the automated image analysis tool, allows rapid, convenient and realistic determination of fiber architecture effects in fiber composite laminate elements comprised of large numbers of fibers. The demonstration analyses presented in Figures 45 to 47 show the capability of this tool to accurately represent strain and stress flow paths within complex fiber architectures. The artificial regularity of profiles generated using the earlier analyses based on ideal hexagonal grids is eliminated in this computational arrangement.

While providing valuable insight into the effect of fiber architecture on microcrack initiation a more dynamic description of microcracking processes was sought in the second year of the program. When the Voronoi Cell FEA grid was used to represent crack development processes it was evident that the grid geometry exerted an influence over the predicted crack propagation directions. This highlighted the need to investigate application of adaptive meshing techniques to crack analysis.

A survey of published literature showed that a number of initiatives have identified the need for adaptive meshing techniques. However none of the analyses examined were thought appropriate for the specific problem of fiber level crack development. For example the state of the art analysis, referred to as the Virtual Crack Closure Technique (VCCT), requires the *a-priori* definition of a failure surface and as such is useful only in interrogating predetermined (essentially intuitive) crack development mechanisms. Therefore an initiative was undertaken to develop a specific adaptive meshing FEA technique for the problem at hand.

The first step in the development of a useful crack analysis tool was the representation of fundamental and intuitive crack propagation processes. Essentially this involved developing the numerical techniques for release of element nodes when critical threshold crack energies are exceeded. This is represented in Figure 48 where an essentially orthogonal grid is used to represent the development of a crack where the result is intuitive. The crack correctly grows toward the load first, and then grows sequentially in both directions from the load center.

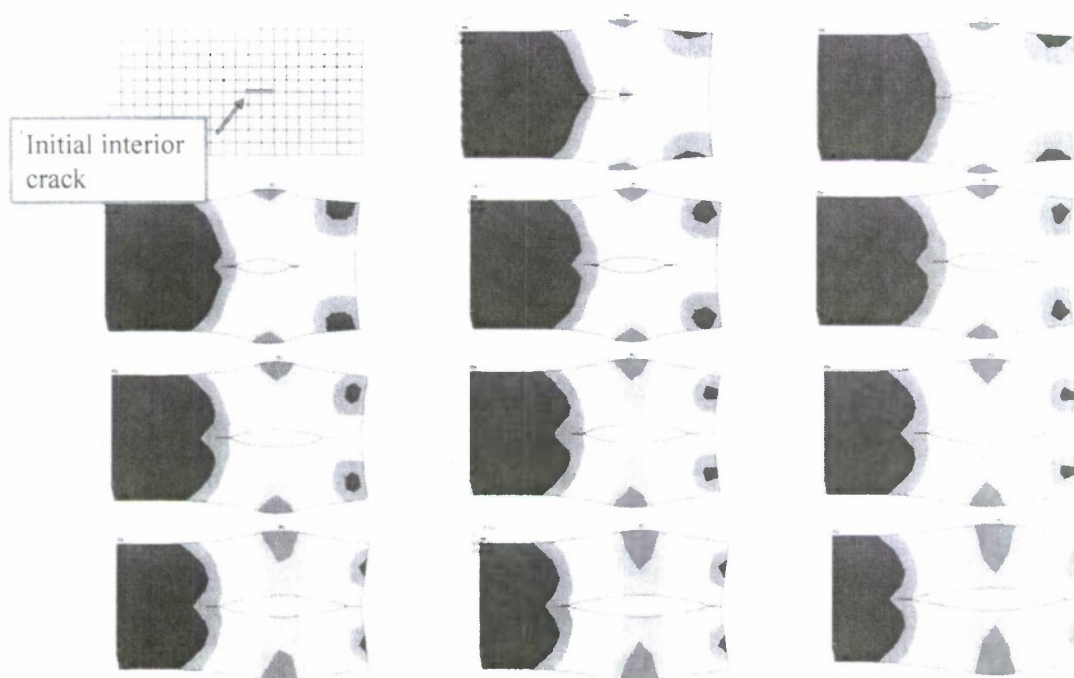


Figure 48 Mode I crack development in homogenous isotropic material subjected to a boundary crack opening displacement.

The adaptive meshing technique is applied in a further example as seen in Figure 49. Here the initial mesh is changed so that the pure mode I path is not available in the original model. The adaptive meshing correctly modifies the mesh as the crack grows to generate the pure mode I growth direction. This is a very significant demonstration because it shows that the adaptive meshing algorithms have been implemented during the solution sequence to correctly permit the modified mesh boundaries to align with the preferred mode I crack growth direction.

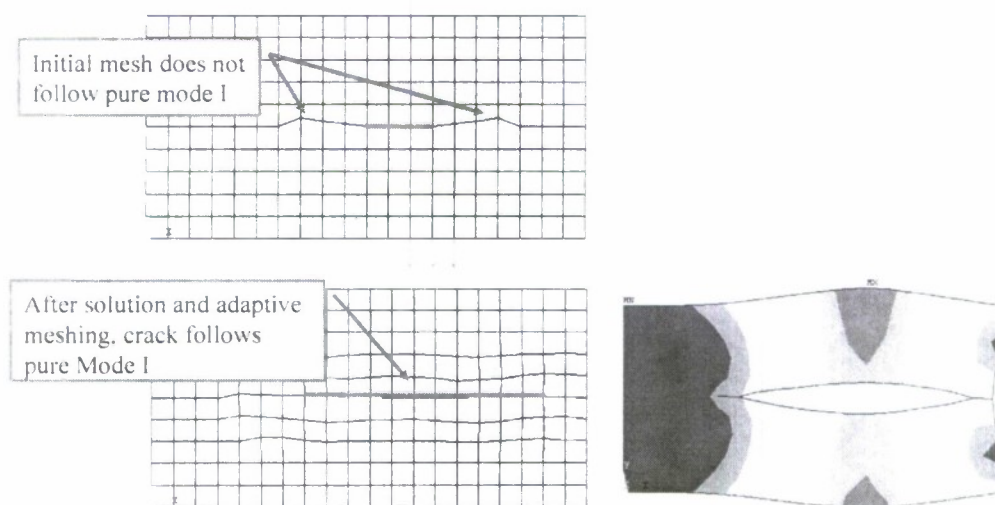


Figure 49 Internal crack propagation in two directions with adaptive meshing

The preliminary work described above allows the representation of a crack initiated in a 2-D mesh when a load is applied on an exterior boundary. Crack growth is correctly represented to proceed along internal mesh boundaries with automatically calculated adaptive meshing. Additional solution algorithms are required to ensure that crack growth direction and adaptive meshing results change with load, irrespective of initial mesh. These will capture the effects of local load redirection and reorientation in composite architectures that include internal damage. All routines must be validated with simplified meshes prior to application to fiber composite mesh.

The technique of adaptive meshing is iterative in nature. This is shown as a process flow schematic in Figure 50 which depicts the solution algorithm. The mesh is iteratively modulated at each crack growth increment until the mesh boundary aligns with the maximum crack growth energy direction. The crack is then "opened" and the process is repeated at next growth increment.

Figure 51 shows the effect of implementation of adaptive meshing on the predicted crack development in an isotropic material subjected to an eccentric load. It illustrates how crack predictions are limited without incorporation of the adaptive meshing algorithms, i.e.: it is not possible to show the correct shape of the crack growth without adaptive meshing at the crack tip. This correlates directly to proper calculation of the crack energy, failure criteria, propensity for crack growth, etc. The accuracy of the prediction provided by the adaptive meshing solution can be verified with a simple experiment. If a small tear is placed at the edge of piece of paper, and then loaded in a similar fashion to that shown the tear (crack) shape is seen to closely follow the adaptive mesh model predictions. A similar illustration of the utility of the technique is also shown in Figure 27, for the case of shear loading. It shows how the predicted crack growth shape changes with change in loads. Again, without adaptive meshing, the top view shows that only an "unzipping" of the part could be simulated, while the lower picture more closely replicates what is expected in real material response.

Output from the initial effort to apply the developed techniques to crack development in composite microstructures under load is given in Figure 53. Note that in Figure 53 fiber center data was used to develop a Voronoi Cell Finite Element mesh though isotropic material properties were applied to the entire area. Thus no real effort was made to represent the presence of the fibers. A relatively coarse angle resolution was used for convergence of the adaptive mesh solution. Effectively the exercise illustrated was one of representing crack growth at the edge of an actual fiber mesh, to see how the adaptive meshing works with a much more complicated mesh with poorly shaped elements. The results show that the algorithms work correctly with this complicated mesh, but also highlight the potential future need for incorporating Jacobian correction (element shape correction to maintain a positive determinant of the Jacobian matrix) as part of the adaptive meshing algorithms. Similar correction algorithms have been incorporated on other programs, and can be applied here as needed though this is not a trivial exercise.

The effect of adjusting the convergence criteria for adaptive meshing is shown in Figure 54. The same crack propagation problem as that analyzed in Figure 53 is again presented here. However in this case the adaptive meshing parameters are changed to refine the convergence criteria before opening the next crack segment. It is significant that with the refined convergence criteria, the adaptive meshing correctly begins to reshape the crack to more closely replicate a pure mode I. Something closer to a pure mode I is expected early in the crack growth, since the load is normal to the upper surface. Comparison of this result to that given in Figure 53 shows a lesser tendency for the crack growth to closely follow the down-ward slope of the initial mesh boundaries, i.e.: there is less adaptive meshing refinement with a coarser convergence criteria for the result given in Figure 53. Again, this tends to confirm the robustness of the algorithms, and shows the capability of the adaptive meshing to correctly represent the crack growth direction.

The completed simulations show the model method which has been developed and demonstrated to predict crack growth in the fiber microstructure. When combined with the previously described automated meshing algorithms, the total solution technique provides the capability to develop a mesh which represents measured fiber locations, predicts highest strain regions for a given load condition, and subsequently predict crack growth across the fiber microstructure for assumed crack initiation in the region of highest strain. Alternately, if voids are identified in the fiber microstructure, these can also be explicitly simulated as a crack initiation location. Validation of the model predictions using the digital imaging techniques is described in the next section of this report.

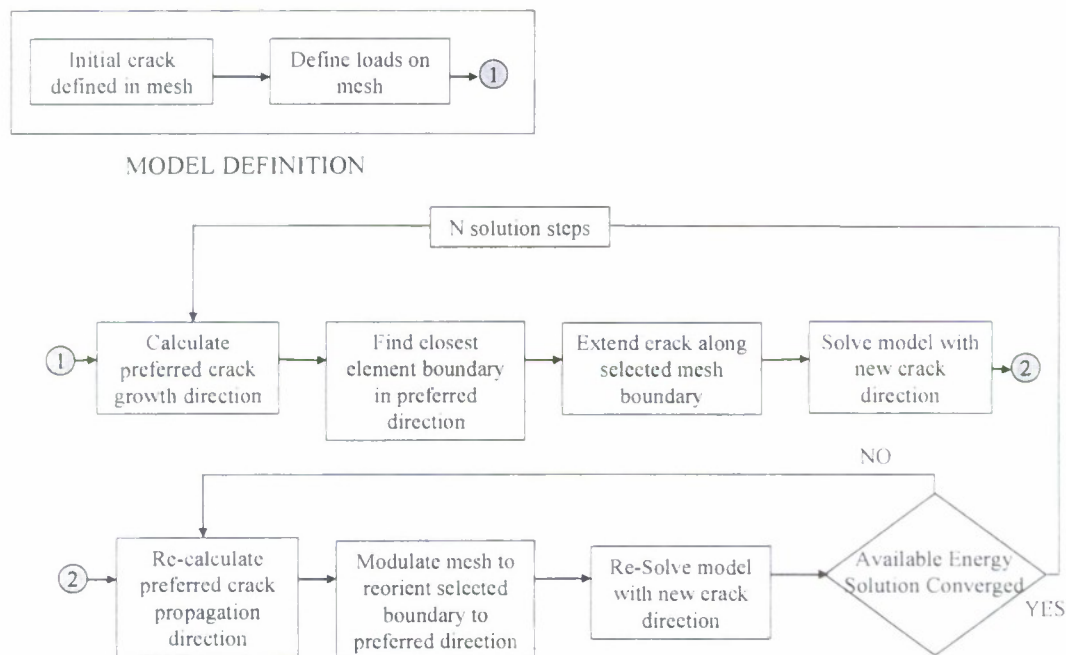
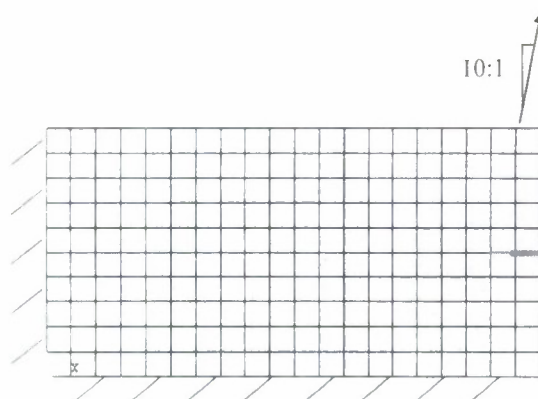
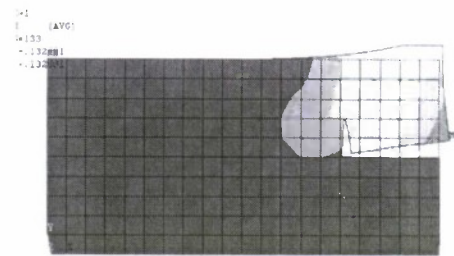


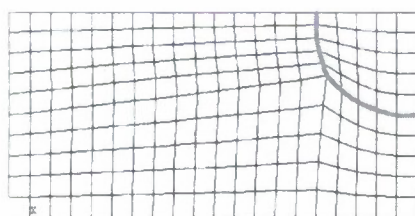
Figure 50 Flow chart of iterative adaptive meshing algorithm



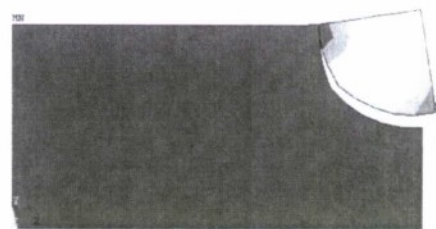
Baseline Model with Initial Crack



Without Adaptive Meshing Lateral Growth Occurs for Three Steps, then Vertical Growth

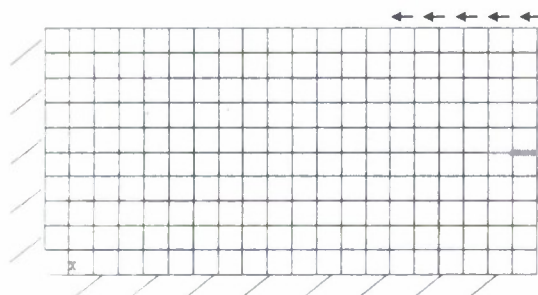


Adaptive Meshing Implemented

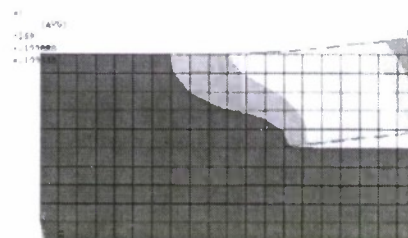


Predicted Crack Growth to Failure Using Adaptive Meshing

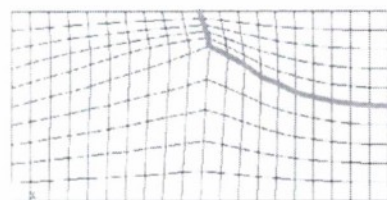
Figure 51 Comparison of predicted crack propagation mechanisms with and without adaptive meshing



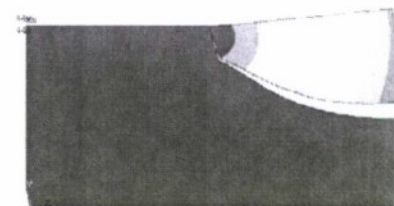
Baseline Model with Initial Crack



Without adaptive meshing crack redirection is not predicted



Adaptive Meshing Implemented



Predicted Crack Growth to Failure Using Adaptive Meshing

Figure 52 Comparison of predicted crack propagation mechanisms with and without adaptive meshing for a shear loaded crack

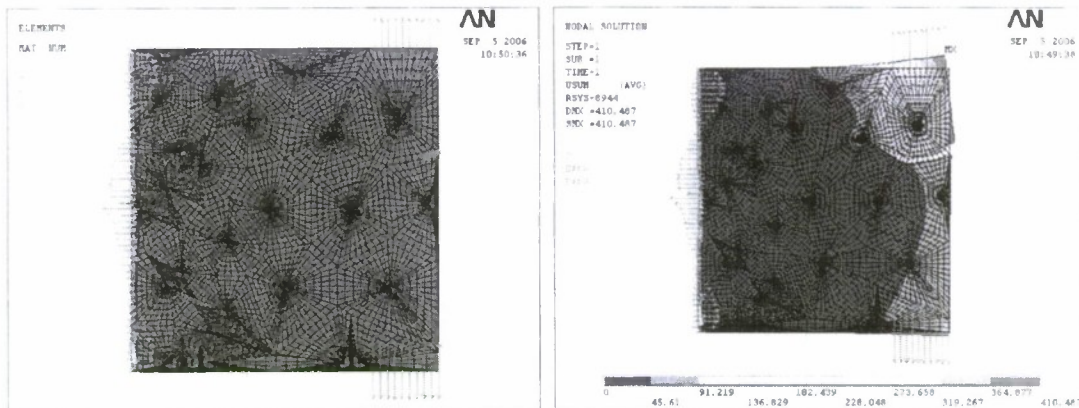


Figure 53 Application of adaptive meshing algorithm to mesh generated using voronoi cells from a real composite microstructure

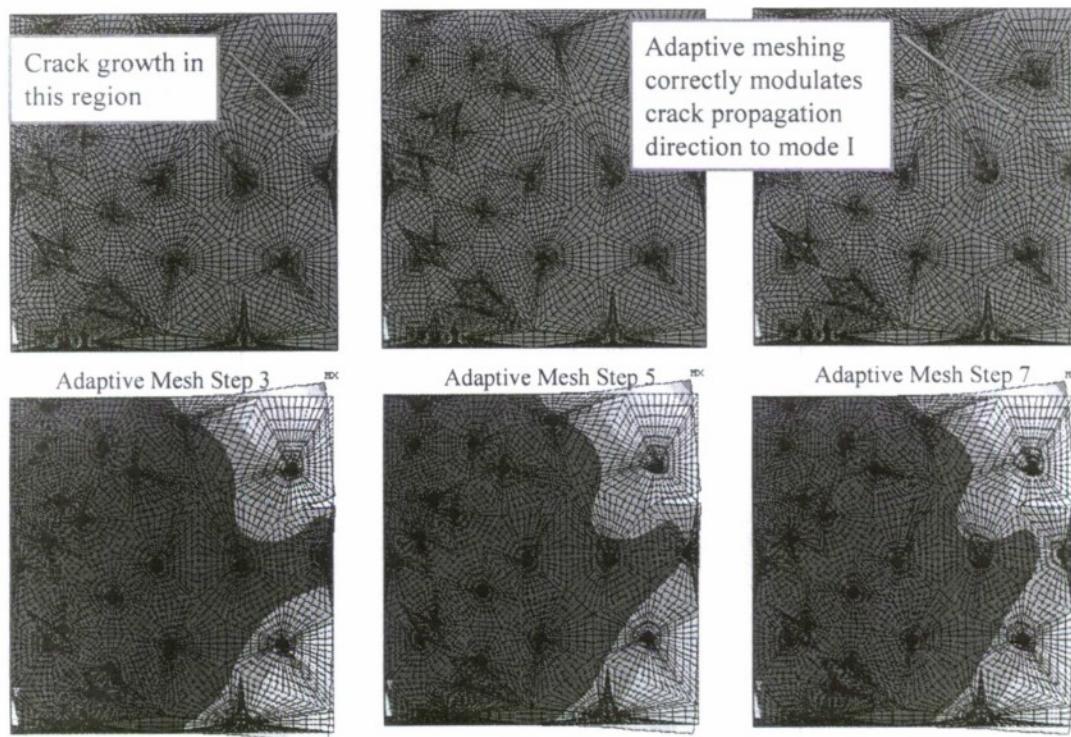


Figure 54 Application of adaptive meshing algorithm to mesh generated using voronoi cells from a real composite microstructure

5.3.2 Strain Mapping Using Digital Image Correlation

Engineering the heterogeneity of fiber reinforced laminate composites has been central concept of modern composite theory and design. While there has always been an appreciation for the importance of various length scales in the development of strength and damage tolerance in fiber reinforced composites, the relationships between the local fiber configuration and performance has remained elusive. In this work, the computational and experimental frameworks required to probe how microstructure and performance are related in these complex, modern structural materials have been developed. In this section the methodology for mapping the spatial distribution of strains in materials is detailed and the critical insights that they can provide are demonstrated. First, an overview of the digital image correlation method and its application to strain measurement is provided. Then its application to a uniaxially loaded, ultra-fine grained nickel "model system" is demonstrated. Finally, the fine structure of the strain field in fiber reinforced composites is shown.

5.3.2.1 Fundamentals of Digital Image Correlation

Digital image correlation (DIC) is a technique used for measuring strain from a sequence of images acquired during a mechanical test. Features of the microstructure are tracked and correlated between images to determine any non-uniform displacement. The image is divided into sub images which are used for tracking and correlation to provide an array of data points with corresponding strain values [16]. These data points can be used to create a strain map for examining the strain field in the specimen. The strain map can show regions of localized strain, strain gradients in the material, or even strain fields around a crack tip [17, 18].

A variety of strategies can be used to quantify the distortion in an image and the associated strain. The original, and arguably more common technique, is to use the gradients in the gray level of regions of pixels in the images [19]. However, this strategy makes critical assumptions about smoothness of the strain field [20] that may not be appropriate in composites or during highly inhomogeneous deformation processes. Consequently, in this work a "point tracking" strategy was applied where convolution was used to track and correlate key points in the sub images. In this algorithm, the sub image region of the deformed region is rotated 180 degrees and used as a convolution kernel. The convolution process is a linear filtering operation where the output pixels are a weighted sum of the input pixels, the sub image pixels of the non-deformed image. The non-deformed image is the base or initial image of the sequence. It is also possible to compare two sequential images, thereby allowing either engineering or incremental strains to be measured simply by modifying which images are compared. The convolution kernel provides the weights for the convolution operation, and the operation produces a peak in the center of the output matrix. This peak intensity, which defines the location of a tracked point, will change if the image deforms. This peak is then subtracted from the local sums of the deformed and base image, and the ratio of this subtraction for the deformed and base image produces a correlation coefficient, R , for each value in the convolution matrix. If R is 1, then the images are exactly the same, but if R is 0, then there is no correlation between the images. A perfect mismatch will produce an R value of -1.[21, 22] The peak value of the correlation matrix is determined,

and the location in the image is calculated using a second-order least squares polynomial fit. This polynomial fit provides a 1/10 subpixel resolution in peak position, and is fit over the 8-connected neighbors of the peak correlation value. This point tracking strategy can be used on random or organized arrays of key features in the images of the microstructure.

When the two locations of the points in the images have been determined, additional calculations must be made to map the displacements into a spatial distribution of strain. The position of the correlation peak for a given tracked point is then used to determine any displacement between two images. A surface map can now be created from the displacement values and peak positions for all of the points of interest, and this map is smoothed and fit to an equally-spaced grid to find the gradients of the displacement values. Equations (19), (20), and (21) are then used to find the strain values for each sub image region and the interpolated values between the regions.

$$\epsilon_{xx} = \frac{\partial u}{\partial x} \quad (19)$$

$$\epsilon_{yy} = \frac{\partial v}{\partial y} \quad (20)$$

$$\epsilon_{xy} = \frac{1}{2} \left(\frac{\partial v}{\partial x} + \frac{\partial u}{\partial y} \right) \quad (21)$$

where ϵ_{ij} are the strains with respect to principal axes x , y , and z for the respective displacements u , v , and w . The local coordinate system of the image may be misoriented with respect to the loading axis, or a specific configuration may be necessary for engineering purposes. Consequently, the strains from the image coordinate system, the principal strain values are calculated using Mohr's circle. The equations used for determining the principal strains in the material coordinate system are listed below:

$$\epsilon_{11} = \frac{1}{2}(\epsilon_{xx} + \epsilon_{yy}) + \sqrt{\left(\epsilon_{yy} - \frac{1}{2}(\epsilon_{xx} + \epsilon_{yy})\right)^2 + \epsilon_{xy}^2} \quad (22)$$

$$\epsilon_{22} = \frac{1}{2}(\epsilon_{xx} + \epsilon_{yy}) - \sqrt{\left(\epsilon_{yy} - \frac{1}{2}(\epsilon_{xx} + \epsilon_{yy})\right)^2 + \epsilon_{xy}^2} \quad (23)$$

The resulting strain maps are used to analyze the strain field of the microstructure and determine values such as the mean strain of the sample or localized strain events. In the case of a uniaxially loaded "model system", DIC enables the visualization of necking in a thin sheet of Ni. The strain in the necking region can be compared to the strain far away from the neck to quantify the effect necking has on the immediate neighboring region of the sample and provides critical insight into the heterogeneity of plastic deformation.

5.3.2.2 Model System: Materials and Experimental Methods

The accuracy of strains measured using digital image correlation methods depends heavily on proper lighting, vibration isolation, and image analysis parameters. Given the complex nature of the strain distributions that were expected in the composite systems, a uniaxially loaded model system was adopted to establish the accuracy of the applied methodology. In this section the processing history of the specimens, their geometry, and how they were prepared for testing is detailed. Then the details of the equipment and software used for testing and data acquisition are presented. Finally, the procedure used for tensile testing is reviewed.

5.3.2.2.1 Material Processing and Microstructure

The tensile specimens were manufactured using a lithographically patterned substrate and a commercial nickel electrodeposition process using a sulfamate bath. Two types of samples were used. The first were made from a sulfamate bath with organic additives using direct current (DC) electrodeposition. The second group of specimens was manufactured using a sulfamate bath without organic additives using pulse electrodeposition (PED). The chemistry and grain morphology of the films were then evaluated. Standard metallographic preparation methods were used to grind, polish, and etch the specimens to reveal the grain morphology of the materials. The DC nickel contained nanoscale grains, while the PED nickel contained columnar, ultrafine grains (~100 nm diameter).

One gram of material was analyzed using a LECO elemental analyzer by NSL Analytical Laboratories in Cleveland, Ohio. ASTM E 1587, the standard for chemical analysis of refined nickel, was used as a guideline to determine the atomic percent of C, H, N, O, and S in the nickel thin films. These elements were likely byproducts of the sulfamate baths used to deposit the nickel and would have existed as trace elements. The results of the chemical analysis are in Table 6, where DC and PED correspond to direct current and pulse electrodeposited samples respectively [8]. Although the DC deposited and PED samples both contained trace elements from the deposition bath, they contained at worst 0.6% impurities and should be considered pure nickel specimens.

Table 6 Atomic percent of elemental impurities in electrodeposited nickel specimens

Sample Type	Atomic Percentages Present					
	C	H	N	O	S	Al
DC	0.25	0.045	0.022	0.12	0.03	99.4
PED	0.037	0.0054	0.0033	0.017	0.003	99.8

5.3.2.2.2 *Specimen Geometry and Mechanical Testing Procedures*

Two sheets of 224 dog-bone tensile samples each were patterned using lithography, and each sample was marked with a specific sample number by a commercial plating company. The dog-bone samples complied with ASTM E-8 for tensile testing of metallic materials with a scaled-down geometry [24]. The geometry of the samples also adhered to ASTM E345 for tension testing of metallic foils. This standard is used for room temperature testing of specimens with a thickness less than 150 μm .

The PED samples had a trapezoidal gauge area and an average gauge length of 560 μm . The width was 125 μm on the backing plate side and 122 μm on the deposition side, and the gauge section thickness was 35 μm . The DC deposited samples had a rectangular gauge area and average gauge length of 580 μm . The average gauge width was 122 μm , and the sample thickness was 25 μm . The radius of curvature was 1.15 mm for PED and DC deposited specimens at the reduced area transition. Each specimen had support material in the form as tethers on each side of the specimen, which prevented loads from acting on the gauge section during handling and placement in the grips.

5.3.2.2.3 *Mechanical Testing System*

Mechanical testing was performed on an Instron 5848 Microtester electromechanical load frame in laboratory air. The load cell used was a 100 N Instron 2530 series low profile static load cell with a resolution of $\pm 0.1\%$. Instron micro-pneumatic grips controlled using foot pedals were used for gripping the specimens with a 40 psi air pressure. An alignment fixture was attached to the bottom grip to help prevent off-axis stresses developing during testing. PID tuning of the load frame for load control was performed using the procedure outlined in the load frame instruction manual in load control mode. The Instron 5800 console, in conjunction with custom LabView software, was used to control the actuator and record and analyze data.

A Pulnix TM-9701 monochrome progressive scan camera was used to record images of the tests and to measure the specimen geometry. The resolution of the acquired images was 768 (H) \times 482 (V) pixels. The imager was a CCD device 8.9 (H) \times 6.6 (V) mm with a cell size of 11.6 (H) \times 13.6 (V) μm . The camera was mounted on a Newport vibration damping rod attached to a Newport 560 series x-y-z stage. Motion in the x- and y-directions was controlled using Newport model ESA1330-OPT-01 electrostrictive actuators that were adjusted manually and using a Newport ESA-C controller. Vertical motion was controlled using a manual Newport SM-13 model micrometer. Focusing was accomplished by controlling the appropriate electrostrictive actuator using custom LabView software and manufacturer-provided drivers for the ESA-C Controller and NI Vision 3.6.1 and NI PC1-1422 frame grabber to control the camera for image acquisition. The entire camera system was mounted on a lab jack for coarse vertical position control. A Mitutoyo long working distance 20 \times objective (working distance approximately 3 cm) was used to acquire images of the gauge section. The load frame and camera system were mounted on an aluminum plate resting on a Minus-K model 250BM-1C 265 lb capacity vibration isolation system with model 350 BM-1 horizontal stiffening columns.

All samples were tensile tested in lab air at ~22°C. One end of a tensile specimen was aligned in the bottom grip and clamped using the micro pneumatic grips. The top grip was lowered and then clamped to the top of the tensile specimen. A preload of 1 N was applied to the sample using the Instron 5800 console "specimen protect" function to allow easy cutting of the top support tethers using the wire snips. After the top two support tethers were cut, a second preload of 1 N was applied to the sample to remove slack. The appropriate test parameters, described in the following sections, were entered in the LabView program. Next, the camera was centered on the gauge length of the specimen and focused using an autofocus algorithm that determined maximum contrast for the image. The ESA controller was swept from a minimum voltage value of 10 V to a maximum value of 120 V in 6 V increments, adjusting the electrostrictive actuator parallel to the focusing direction of the camera system. Contrasts was determined by calculating the standard deviation of a Prewitt-filtered edge detection image of the sample. The voltage corresponding to maximum contrast was used as the basis for the next sweep, starting 6 V below the peak contrast value to 6 V above the peak contrast value in steps of 1 V. A third sweep was utilized using a range of 1 V less than and greater than the new peak contrast voltage value in steps of 0.1 V, the most precision attainable using this ESA controller system. The voltage corresponding to the maximum contrast from the third sweep was used as the point of best focus. The frame rate of the camera was set and a base file name was chosen for the images, then the camera awaited a trigger from the 5800 console to begin image acquisition. Once the mechanical test was started in the LabView program, the camera triggered and acquired images at the specified frame rate. The test data was saved to a tab delimited text file and included the specified test parameters.

5.3.2.2.4 *Data and Image Analysis Methods*

The force, displacement, and image data were used to establish the mechanical properties of the thin film nickel specimens and to validate the image correlation methodology for before its application to a composite. Mechanical property calculations were performed using Microsoft Excel 2002, Kaleidagraph 7.0, and Matlab 2006a. Particular attention was given to the comparison of strains measured from crosshead displacement (via a compliance correction scheme) to those found with DIC.

Tensile tests were performed to determine reproducibility of the data and determine the compliance correction factors. A compliance correction factor was used to adjust the stress-strain behavior generated from cross-head displacement for machine compliance and specimen compliance to achieve accurate engineering strain values for all mechanical test results. A strain rate of 0.003 sec⁻¹, or crosshead displacement of 0.1mm/min, was used to comply with ASTM E-8. The elastic modulus was assumed to be 200 GPa, and then the compliance was corrected using the following equations:

$$C_s = \frac{E/E_u - 1}{E \cdot A \cdot L} \quad (24)$$

$$C_a = \frac{C_s}{1 - E_u/E} \quad (25)$$

$$\varepsilon = \varepsilon_u \left(1 - \frac{C_s}{C_a} \right) \quad (26)$$

where E is the expected modulus, E_u is the indicated modulus, A is the cross-sectional area, L is the gauge length, C_s is the system compliance, C_a is the specimen compliance, ε_u is the indicated strain, and ε is the corrected strain.

The indicated strain was calculated by comparing crosshead displacement to the specimen's original gauge length. The strain values were shifted to account for the preload using Hooke's law. The slope of the linear-elastic portion of the plot was fitted to a linear curve, and the y-intercept (stress) and its corresponding strain value for the linear fit were calculated. These values were the fitted initial stress and un-shifted strain values of the plot. The shift needed to account for the preload was just the difference between the ratio of the fitted initial stress value to elastic modulus and the initial fitted strain value. This strain shift value was typically 5-10 % of the sample's failure strain.

Digital Image Correlation (DIC) was utilized to provide an alternative method for measuring strain from the mechanical tests. A Matlab program written by Eberl at Johns Hopkins University was used to determine strain in the tensile, creep, and fatigue specimens. A sub image region size of 30×30 pixels spaced 15 pixels apart (producing a 50% overlap) was generated for the gauge section of the specimens. Correlation was performed using a convolution matrix. The input image was rotated 90 degrees with respect to the displaced image, which was used as the masking element. The result was a cross-correlated convolution matrix with a peak. This peak would shift from the center of the convolution matrix if the displacement between the two images was not uniform. The peak position was determined using a second order polynomial fit over the 9 pixels surrounding the peak value. The position of the extremum of this fitted peak provided a 1/10 pixel resolution in peak position. Strain in the specimen would shift this peak and produce a displacement u in the x-direction and displacement v in the y-direction.

To produce a strain map, the peak position data and displacement data was fit to a grid using the Matlab command "griddata" using a cubic interpolation and Qhull delaunay triangulation options Qt, Qbb, and Qc. The grid spacing for fitting the data was calculated using Equation (27):

$$S = 2^{\log_2 \left[\left(\frac{M}{x} \right) \right]} \quad (27)$$

where M was the range of movement in an axis direction, x was the number of points used in the analysis, and the exponent returned the smallest power of two that was greater than or equal to the absolute value of the quantity in the parentheses. The gradient of the displacement data fitted to the grid of peak positions in the x-direction and y-direction produced values of strain for each grid point. These strain maps could then be overlaid

onto the corresponding image to see how the strain field corresponded to the microstructure of the nickel. The mean values of these strain plots were used for matching with stress values for production of stress-strain plots. The average strain calculated is analogous to averaging achieved through utilizing an array of strain gauges (i.e. for every grid point) or a clip gauge.

The program was able to resolve $1/1000^{\text{th}}$ of a pixel of displacement for determining strain measurements. The strain rate of 0.003 sec^{-1} and frame rate of 2 provided 1 pixel of movement between images. Principal strains were calculated by applying Mohr's circle to the components of strain the x-axis, y-axis, and the shear strain. This data was correlated with the measured stress values to generate a stress-strain curve. The modulus was determined from this curve using least-squares linear fitting applied to the initial linear portion of the stress - DIC mean strain plot, typically the first 15-20 data points of 70-120 total data points.

5.3.2.2.5 *Mechanical Testing Results and Discussion*

The elastic modulus values, failure strains, and yield strengths of 13 nickel specimens (both PED and DC fabrication methods combined) were determined using both

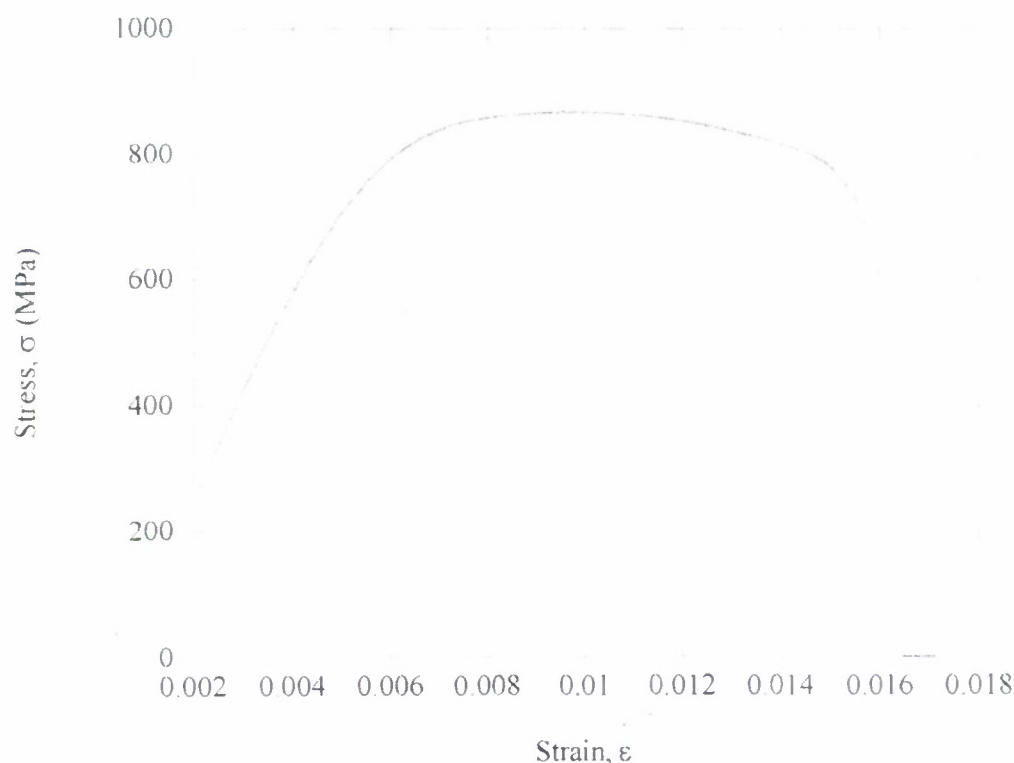


Figure 55 Tensile test of specimen 1 initially loaded to 1 N (234 MPa). The sample was PED, and strain was measured using crosshead displacement data. The values of strain are shifted to account for a preload, and the data values are compliance corrected.

compliance and image correlation methods for measuring the strains. The constitutive behavior of the PED nickel specimens resembled an elastic-perfectly plastic material, and a typical tensile test is shown in Figure 55. The ultimate tensile strength of typical PED specimens was 1130 MPa, the yield strength was 1100 MPa, and the strain to failure was 0.0150. The observed behavior was consistent with previous studies [10] and the expected behavior of the very fine grain morphology.

Digital image correlation results of tensile test images were compared to results analyzed using crosshead displacement. Figure 56 shows stress data acquired from the load cell correlated with strain data from the DIC Matlab programs compared to the results acquired from compliance correction. For samples where failure occurred within the region of interest, failure strains a magnitude higher than failure strains from crosshead displacement were observed due to localized necking in the specimen. Additionally, the measured elastic modulus of the samples was 80 to 120 GPa, or roughly half of the assumed elastic modulus of 200 GPa. This critical finding would not have been possible without applying the DIC technique.

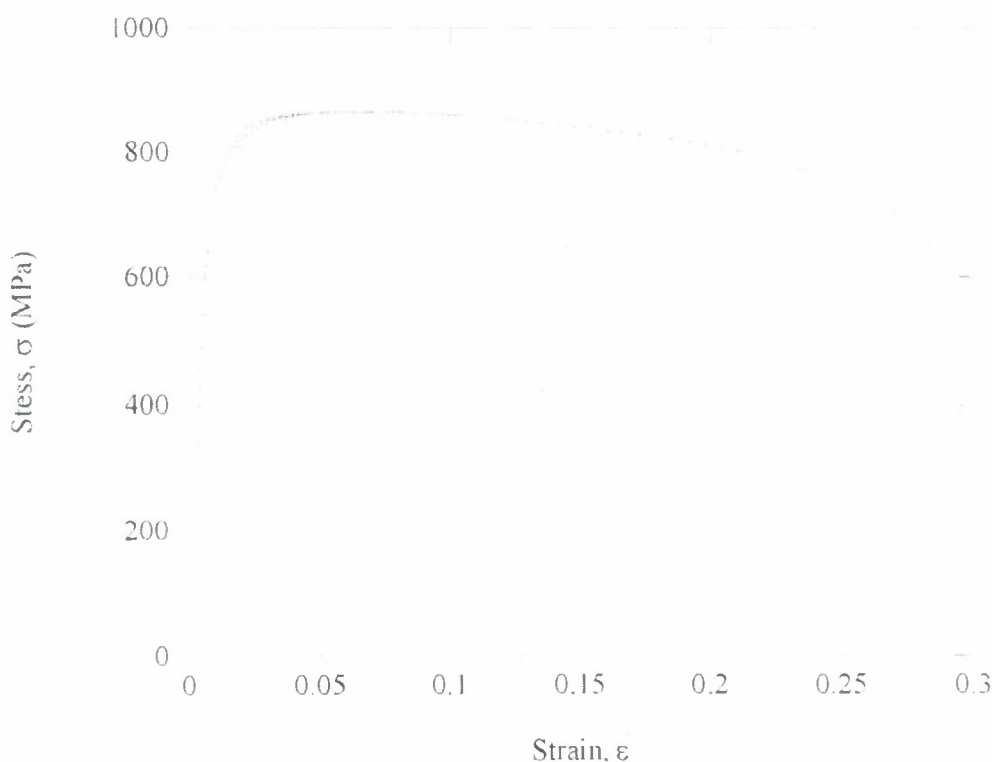


Figure 56 DIC tensile test of specimen 2, initially loaded to 1 N (234 MPa)

The DC electrodeposited samples exhibited behavior similar to the PED tensile specimens. Figure 57 compares stress and strain data from a compliance corrected plot of strain ($E = 200$ GPa) and DIC results of the tensile tests. Because the DC electrodeposited samples also exhibited localized necking, the region of the specimen that

underwent necking was analyzed in the DIC program for an accurate measurement of strain to failure. The elastic modulus measured from the DIC was between 140-160 GPa. The increase in modulus needed to approach the bulk material value of 200 GPa would be smaller for the DC electrodeposited tensile specimens when compared to the PED specimens.

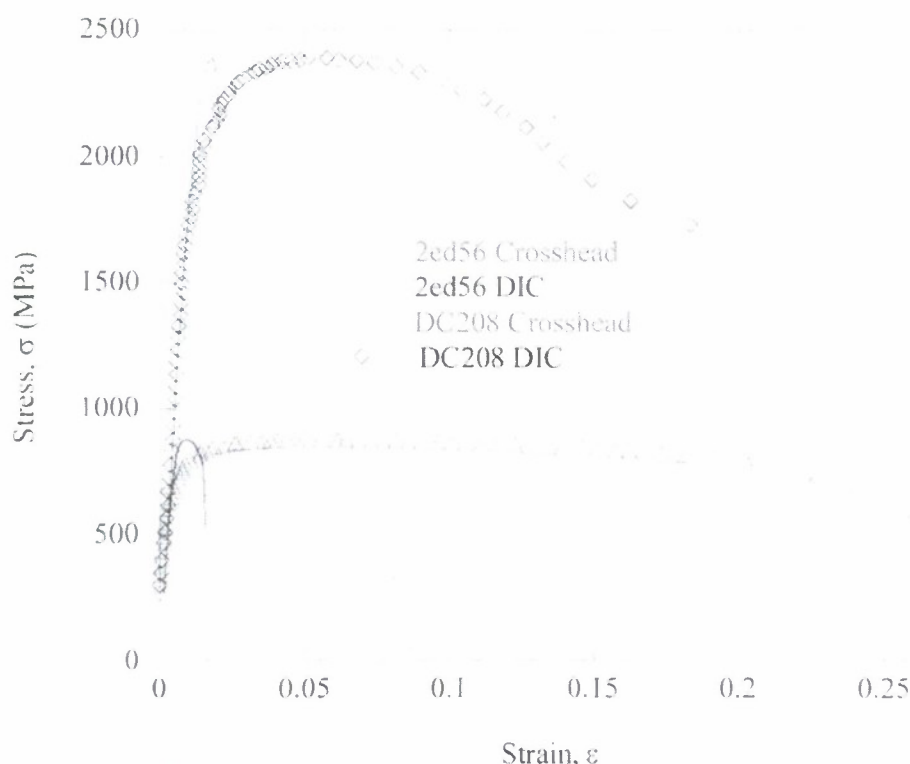


Figure 57 Comparison of strain data generated by crosshead displacement (2ed56 Crosshead and DC 208 Crosshead) to strain data generated by DIC (2ed56 DIC and DC 208 DIC). Both samples were PED. Failure strain values for DIC were much greater using DIC because necking occurred within the region of interest.

5.3.2.3 Composite System: Materials and Methods

The methodology that was developed to characterize the uniaxially loaded model system was then applied to a fiber reinforced composite specimen. As described above, the mechanical testing system (Figure 58) consisted of 3 major components. The core of the loading system was an Instron 5844 Microtester. This electromechanical loadframe has a high-resolution digital encoder (0.2 μm) and a force capacity of up to 1kN. The beam specimens (carefully polished using procedures developed at the Penn State University Applied Research Laboratory) were loaded in force, displacement, or mixed control modes with a 4-point flexure fixture. The displacements of the specimen were measured using an image acquisition system based on a Pulnix TM-9701 camera (768 by 482 pixels) and a digital image acquisition card (NI- 1422) in a personal computer (PC). The

camera was mounted on a low vibration post and a 5-degree-of-freedom alignment system. The acquisition of images was controlled via custom software written in LabView that allowed for the precise synchronization of the pictures with forces and displacements in the system. The loadframe and digital image acquisition hardware were isolated from ambient vibrations using a Minus-K (BM-250) mechanical damping system. Images collected during the test from various locations (Figure 59) were then evaluated using MATLAB code that was a modified version of the algorithms developed by Eberl.

The typical testing sequence depicted in Figure 60 demonstrates the methodology that was employed. The specimens were loaded at a controlled rate, held for a fixed period of time, and unloaded while images were captured synchronously with force and crosshead displacement. For example, consider a $[(0/90)_2]_s$ laminate (Figure 60(a)) that was loaded in 4-point flexure at 3 N per second until the outer fiber stress in the beam reached 263 MPa. The beam was then held at this peak stress for 10 seconds and then was unloaded. Optical images of the polished surface of the specimen (Figure 60 (b)) were captured at 5Hz and evaluated after testing. Three types of experiments were performed. First, the strains in the composite beam were mapped at a low resolution where the plies, but not the individual fibers, could be evaluated. Subsequent experiments were conducted at higher magnifications with a higher pixel resolution camera to establish the inter-fiber strain distribution in various plies, at ply interfaces, and in the vicinity of cracks.

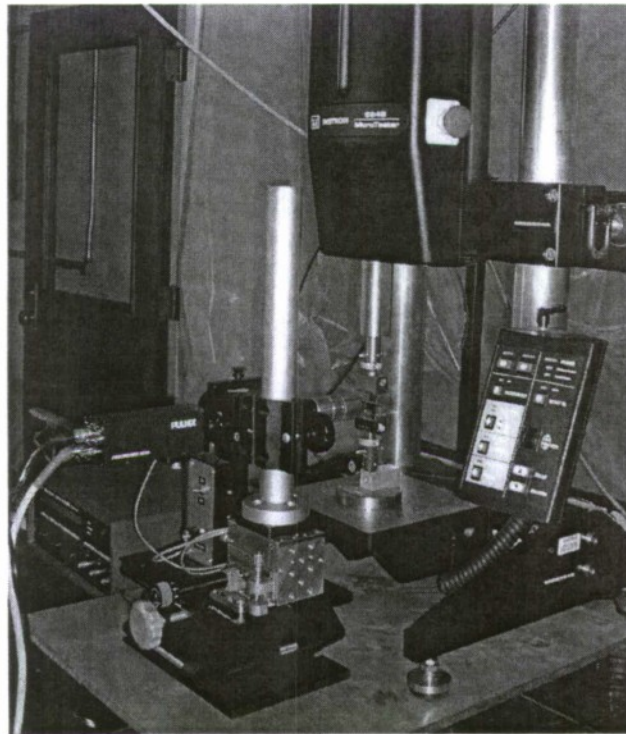


Figure 58 Photograph of the mechanical testing and strain measurement system. The Instron loadframe, specimen, grips, vibration isolation platform, and image acquisition hardware are shown.

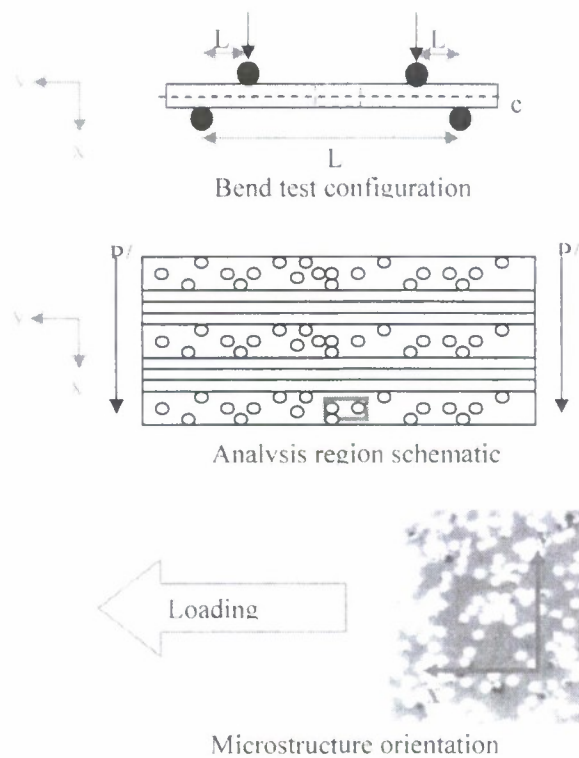


Figure 59 Schematic depiction of the composite specimen and the analysis regions.

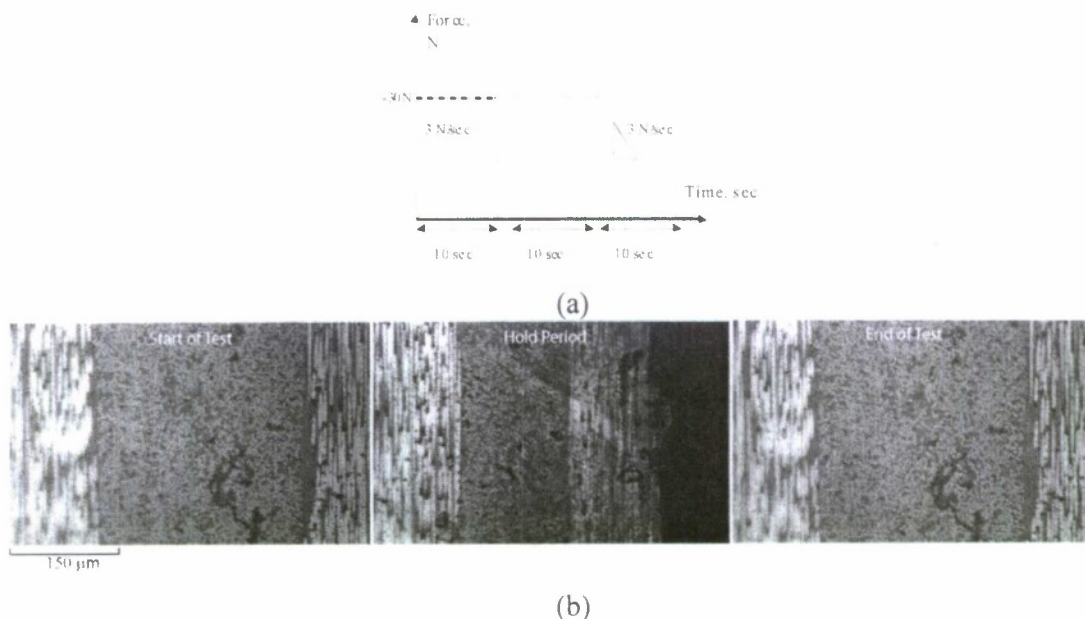


Figure 60 Typical mechanical test of a composite laminate in the Penn State system. a) The specimen is subjected to a trapezoidal waveform where the loading rate is constant (3 N/sec) until the target force of 30 N is reached, held for 10 seconds, and the force is ramped back to the initial (low) level. b) Throughout the test optical images of the specimens (20 \times objective lens) are captured for strain analysis. Motion in the images can be correlated with strains and rigid body displacements.

5.3.2.4 Composite System: Low Magnification Results and Discussion

Initially, experiments were performed with a resolution that was too coarse to resolve the inter-fiber strains. The primary purpose of varying the resolution of the system is to identify and eliminate features that are an artifact of the image acquisition and/or analysis methodologies. For this purpose, the strains in the [(0/90)₂]_s laminate surfaces shown in Figure 60 were determined at two magnifications from the digital images. Figure 61 shows the measured strain as a function of image number in the test based on a point tracking algorithm [26]. An interesting feature of this data is the effect of the different plies of the composite entering (and leaving) the analysis region of interest (the green rimmed, light, rectangular region in the figure). While it is possible to calculate strains, the average values shown in Figure 61 contain contributions from multiple plies and the interfacial regions between the layers. This illustrates the well-known inhomogeneous distribution of strains in laminate composite systems and the challenges that it presents in evaluating deformation of composite laminates.

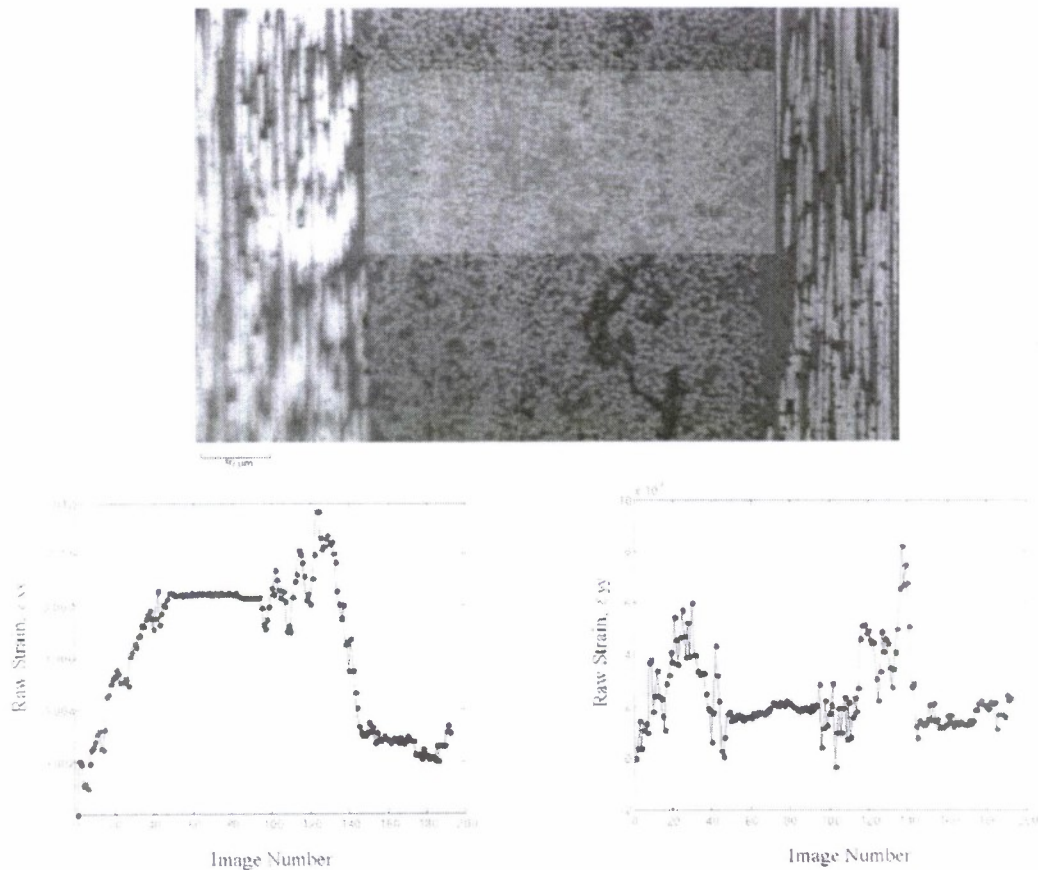


Figure 61 Average longitudinal and transverse strains measured in the composite during the flexure test. The strains were calculated for the region of interest in the central portion of the specimen (green rimmed, light, rectangular portion of the figure). Noise in the strain response is associated with the motion of different ply orientations in and out of the region of interest.

The mechanical loading range (423 to 674 MPa ramp) and the image magnification (50 \times) were adjusted to improve the testing conditions for strain mapping (Figure 62). When the laminate was evaluated at higher magnifications and more details were visible, the average value of strain was better behaved (Figure 63). In addition to the average value of strain, the spatial distribution within the composite was also determined. The variation of strains within a ply during the ramp test is shown in Figure 64. The displacements (top) and strains (bottom) were distributed inhomogeneously within the composite and showed the same general orientation as the fibers in the microstructure. This banding was then evaluated at higher magnifications.

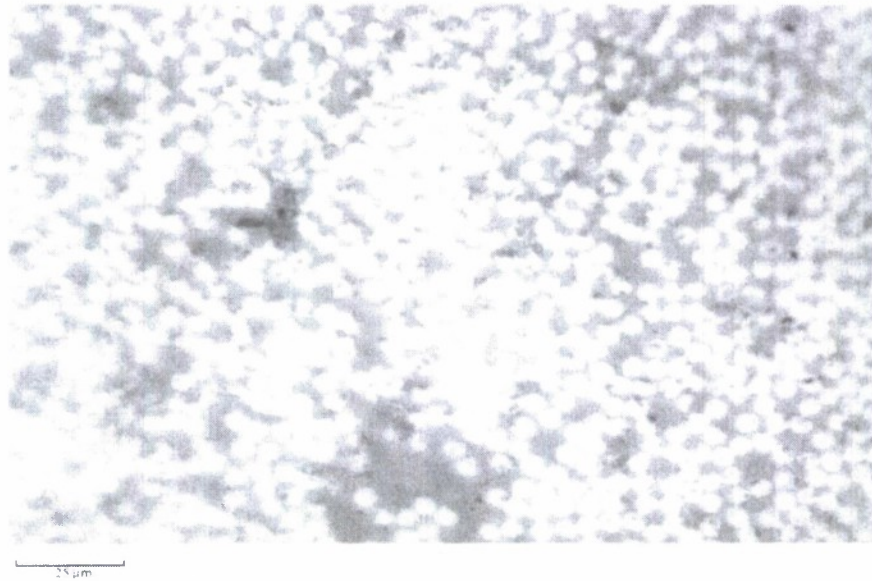


Figure 62 Optical micrograph of the [(0/90)2]s laminate surfaces at a higher magnification (50 \times objective lens) at the start (423 MPa) and end (674 MPa) of a linear ramp test under load control. Details of the individual fibers in the plies are visible.

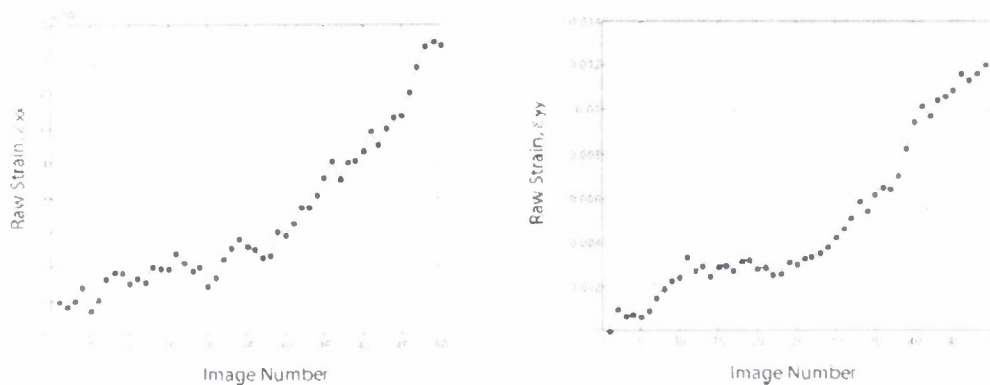


Figure 63 Longitudinal and transverse strains measured during a linear ramp from 423 MPa to 674 MPa. The average strain in the analysis field is less noisy than at lower magnifications.

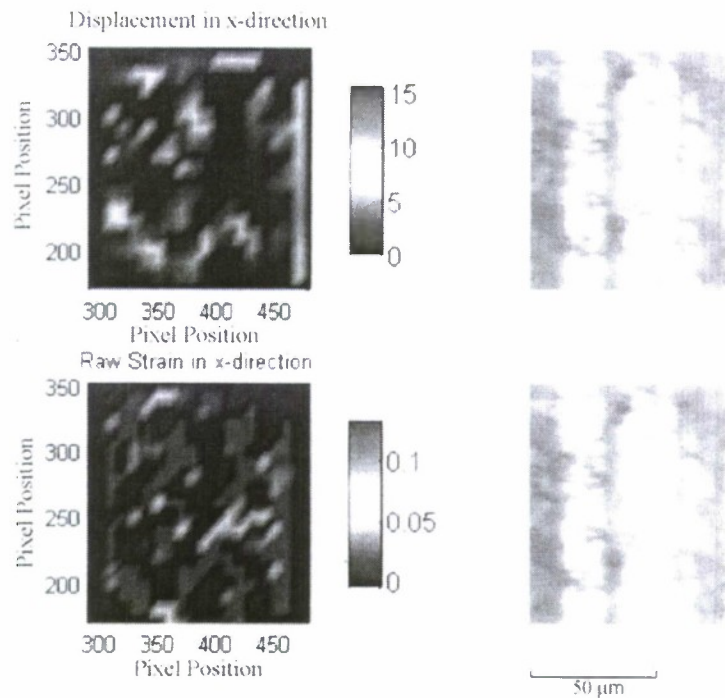


Figure 64 Spatial distribution of strains in a laminate composite. The displacements (and strains) are localized and show the same general orientation as the fibers in the microstructure.

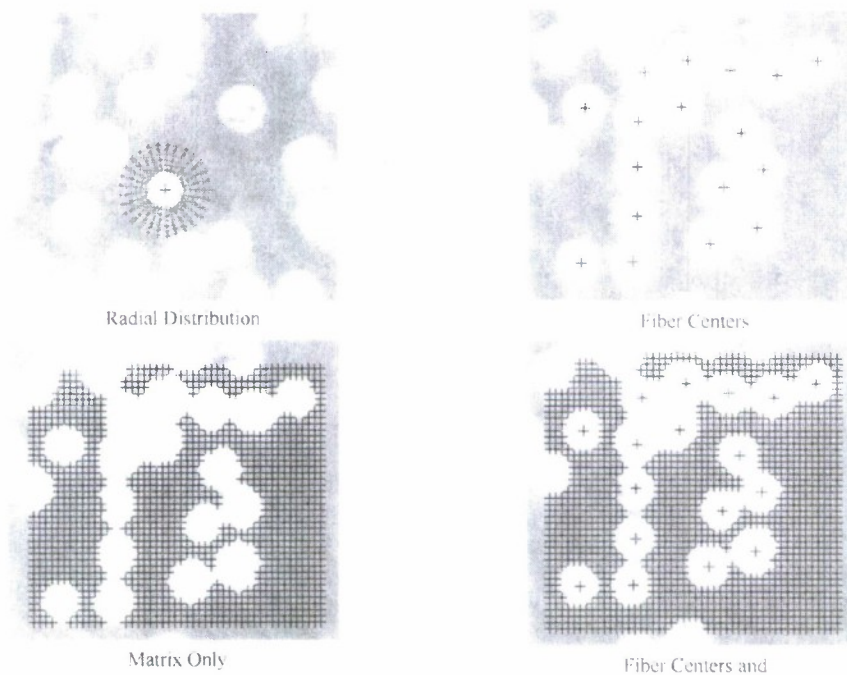


Figure 65 High resolution digital images of fibers and the various grid arrays that were used for strain mapping.

5.3.2.5 Composite System: High Magnification Results and Discussion

The "banding" of strains in the plies of the composite that was observed during low magnification mapping demonstrated that the spatial distribution of deformation in a fiber reinforced composite is very inhomogeneous. Consequently, a series of experiments was conducted with a higher resolution digital camera (PixeLink, Inc.) to verify the observation and to establish the local strains on the length-scale of the individual fibers. Additional algorithms were developed to 1) identify individual fibers in the image and 2) place a regular grid with rectangular or circular symmetry at the boundary or in the adjacent matrix (Figure 65). The ability to vary the nature of the grids used to track points and map strains allowed for the verification of the results and their relationship to microstructural features of the composites. The strains in the composite were then mapped in the tensile, neutral axis, and compressive plies.

The evolution of strains in the tensile ply are shown in Figure 66 as the applied force was monotonically increased. The banding and other trends found in the maps (Figure 67) were consistent with previous, lower magnification images. However, it is interesting to note that significant shear strains were measured in the ply. The importance of this measurement capability should not be understated. The ability to observe the precise nature of load transfer at the fiber matrix interface opens up the envelope of mechanistic interrogation to a level not previously available. It has long been recognized that the unique features of advanced composites are primarily controlled by the properties of the constituent materials and the nature of the bond or interface between them. The manner in which applied loads are transferred from the stiff phase (fibers) to the binding phase (matrix) determines to a very large degree what property spectrum might be available. This is obviously true in relation to static properties but is perhaps just as important in determining dynamic response. Impact, shock and ballistic properties of composite materials have been well characterized, in terms of measurement of salient performance parameters. However, an underlying theory of property determinants has proved elusive, at least in part because of the lack of a capability to determine the nature of the load transfer under such conditions. For instance, land combat services are aware of the desirability of using high fiber volume fraction, resin poor systems for ballistic applications. However, the reasons why such material arrangements provide enhanced performance are not well established. This leads to the situation in which ballistic optimization is largely achieved by a trial and error process. A-priori design of ballistically capable organic matrix composites remains as a goal rather than an established science. From a practical standpoint this reduces to a 'make and shoot' philosophy. It might be argued that application of techniques like Digital Image Correlation (DIC) provides a unique opportunity to uncover the controlling phenomena. Though not attempted in this program there is no practical reason why DIC cannot be applied to dynamic event measurement. Provided a stable series of images can be captured, using any imaging technology that is appropriate to the measurement, the comparative feature of the method can be applied and critical strain (and therefore stress) transfer mechanisms can be uncovered. The existence of large shear strains in the ply location illustrated in Figure 66 is an interesting case in point. The distinct out of plane shear strains are somewhat counter intuitive in the load case imposed. Shear strains in the orthogonal plane (to that viewed) might be expected, though these would also be

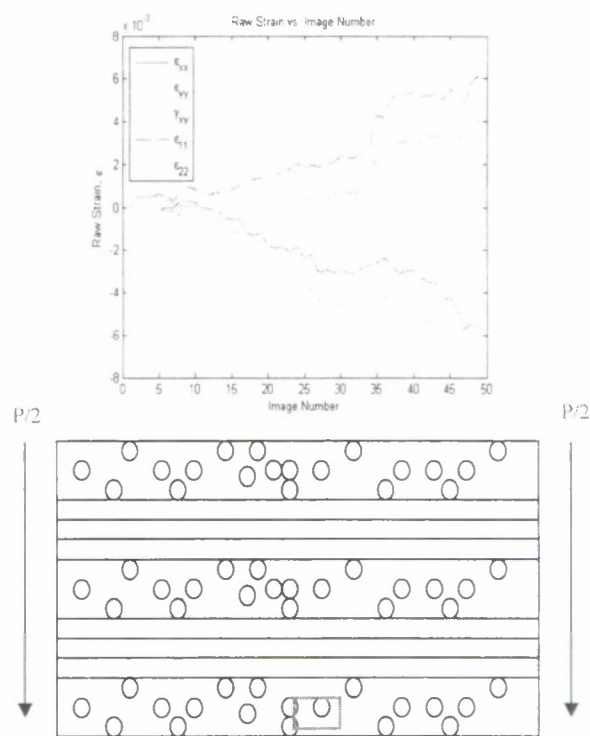


Figure 66 Evolution of strains in the central portion of the outer, tensile ply of the composite and a schematic of the location of the measurement.

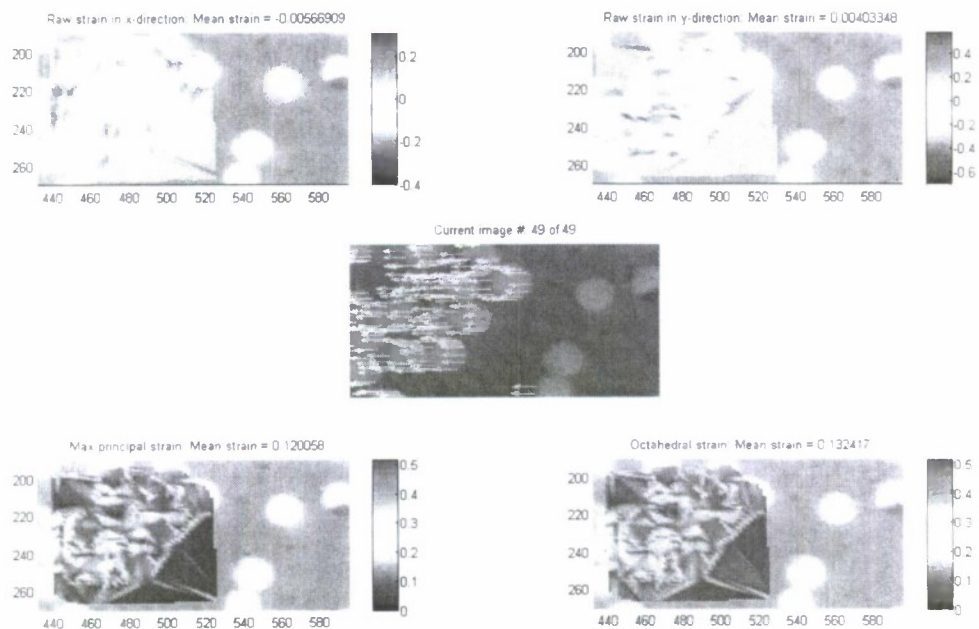


Figure 67 High resolution strain maps from the central portion of the outer, tensile ply of the composite. Tensile strains and banding on the length scale of the fibers was observed.

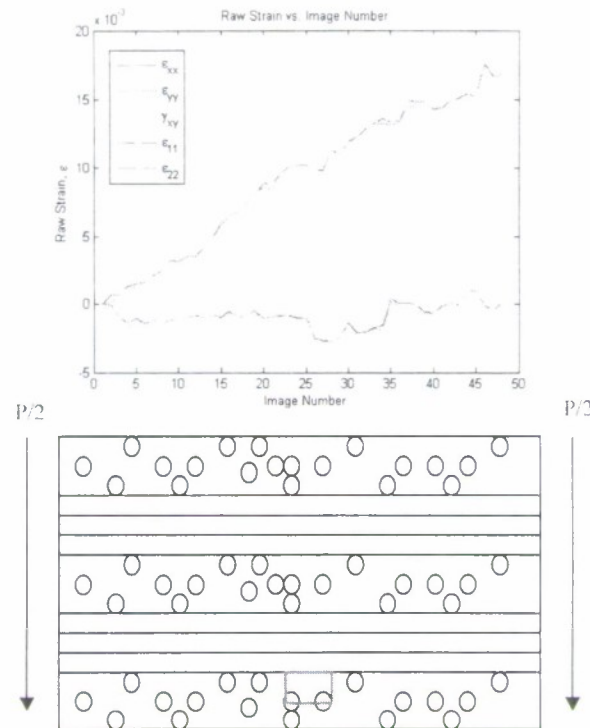


Figure 68 Evolution of strains in the [0/90] interface portion of the outer, tensile ply of the composite and a schematic of the location of the measurement.

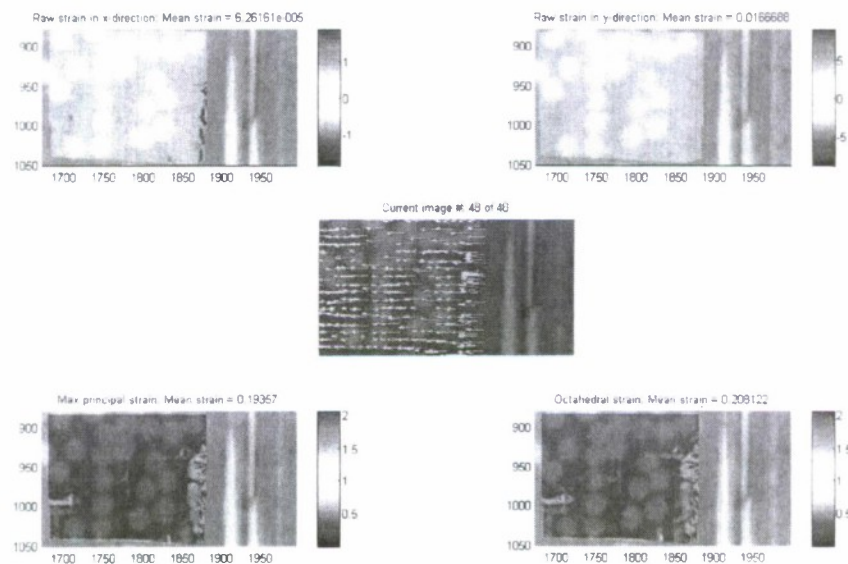


Figure 69 High resolution strain maps from the [0/90] interface portion of the outer, tensile ply of the composite. Large tensile strains oriented along the ply interface were observed.

expected to be relatively low in the outer fibers. It appears likely that the deformation (essentially a Poisson deformation) in the adjacent ply is setting up out of plane shears in the outside ply. However, the important point is that the response of the material can now be examined with a level of knowledge not previously available.

Given the importance of the interfaces between composite plies, additional images taken at the $[0/90]$ interface on the tensile side of the beam were evaluated (Figure 68). As expected, the tensile strains were large and were oriented along the interface (Figure 69). This region is of great interest in developing an understanding of progressive damage mechanisms in composites. It is known that matrix cracks grow toward the ply boundaries if sufficient crack propagation energy is imposed by the applied stresses. However, such damage may be stabilized at the ply boundary and final failure of the composite structures (be it in dynamic or static load situations) is only thought to occur if cracks coalesce and propagate at the ply boundary. Therefore the strain environment in this region is very important, as it determines, to a large extent, whether or not matrix cracks will lead to delamination. Of course the mechanism by which these stresses are created are somewhat independent of their effect. Residual stresses or thermally induced strains will be equally effective in advancing failure mechanisms to a critical state. From the standpoint of thermo-oxidative stability, opening the interply region to oxygen ingress represents a similarly critical condition. Therefore establishment of the ability to study this interface under varying load situations is considered another critical contribution of this effort.

The distribution of global strains in the flexurally-loaded composite beam evaluated with conventional beam theory would suggest that the strains along the neutral axis of the specimen would be homogeneous and small. The evolution of strains in this portion of the specimen (Figure 70) was consistent with this general theory. However, local "hot spots" in the matrix and banding on a scale of the fiber diameters was found (Figure 71). It is interesting to note that even in relatively low strain portions of the specimen, the strains are highly localized within the microstructure of a given ply. In fact, again, non-intuitive strain patterns are seen. For instance, in the case of the x-direction (through thickness) strain a number of locations are seen where a very complex load distribution pattern between fibers and matrix material exists. In the central ply region and specimen center of a four point bend test coupon axial forces (both tensile and compressive) are expected to be low, as the material response is dominated by shear (depending on the aspect ratio of the sample). However, this is the region where the stress state might be expected to be most complex, elements of axial and shear loads both exist here. It has been established that stiff load paths will pick up load more readily than more compliant directions. This can certainly explain the existence of greatly varying strain patterns as seen in Figure 71 and in other results. However close examination of the x-direction (and to a lesser extent y-direction) data reveals cases where fibers carrying magnified tensile loading are adjacent to matrix regions and other fibers that are under compression. It is very difficult to envision a stress state that could impose such a state of deformation. Of course it should always be borne in mind that a specimen edge is being analyzed and this could account for at least some of the complex strain arrangement. However it does

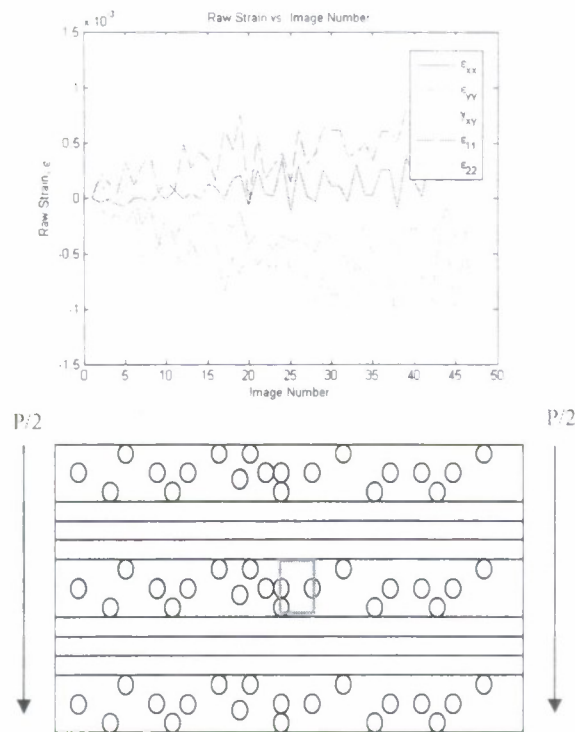


Figure 70 Evolution of strains in the neutral axis region of the composite and a schematic of the location of the measurement.

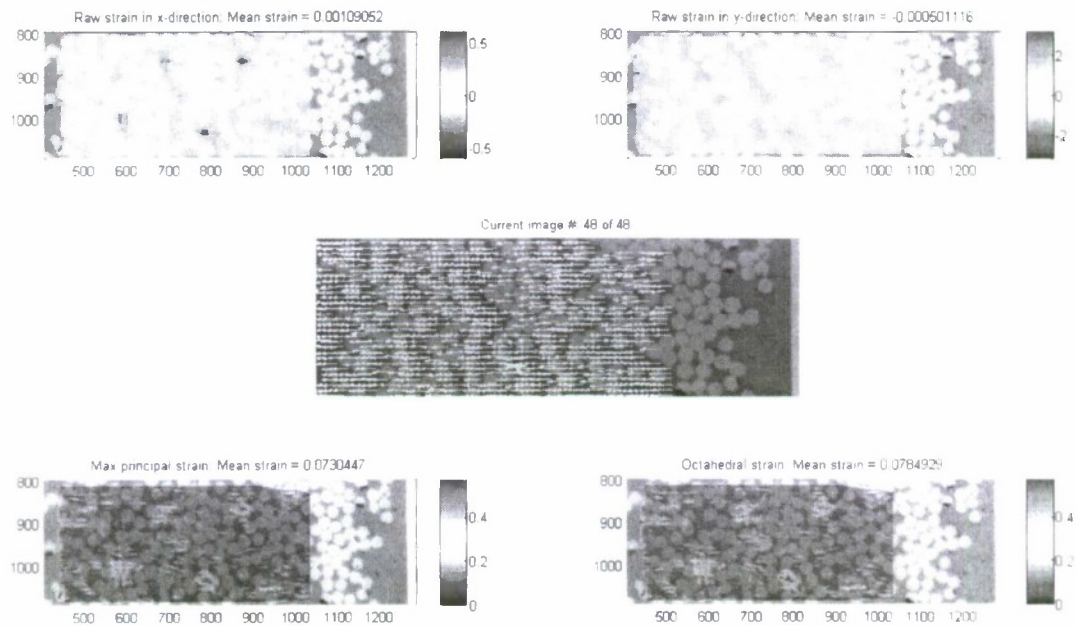


Figure 71 High resolution strain maps from the neutral axis portion of the composite. While local tensile and compressive strains are present, the overall magnitude of the strains was quite small.

appear, from repeated measurements that the nature of stress transfer is more complex than previously reported.

Finally, strain maps of the compressive side of the beam were developed under similar testing and analysis conditions (Figure 72). As expected, the overall strain in the ply was compressive. However, evaluation of the spatial distribution of the strains (Figure 73) showed that, once again, locally compressive and tensile strains are present in the ply. This result sharpens the argument presented above. The existence of tensile strains in a sample region where on compressive stresses can reasonably be expected to exist, illustrates further the complexity of the load transfer that controls material response. The inhomogeneity of strains within the composite, while not unexpected, has been previously difficult to access experimentally. Combined with the other methods developed in this program, a unique capability now exists to explore how damage evolves within composites. The finite element analysis techniques summarized in Section 5.2.7 broadly represent the preferential load paths created by the combination of materials with greatly varying properties. However the 2-D representation did not predict the development of compressive strains under the application of a global tensile load. Extension of the adaptive automated FEA mesh generation techniques to capture 3-D effects may provide explanatory simulations, though this was not completed in the current effort.

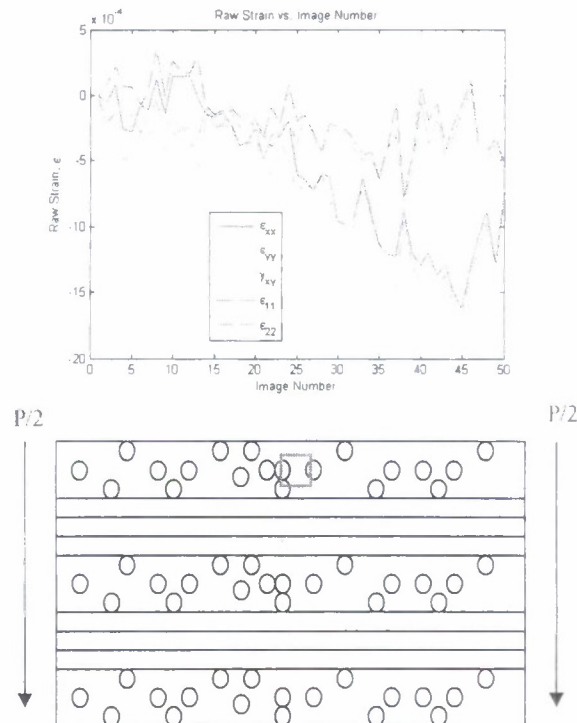


Figure 72 Evolution of strains in the compressive axis region of the composite and a schematic of the location of the measurement.

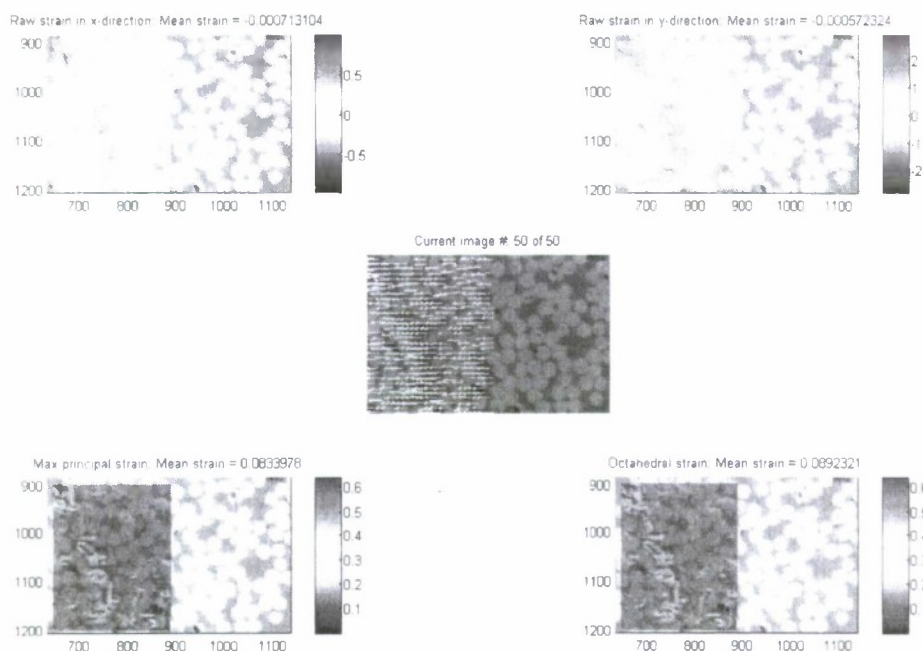


Figure 73 High resolution strain maps from the compressive axis portion of the composite. Tensile “hot spots” and banding are readily apparent in the strain maps in spite of the “globally compressive” stress state.

5.3.2.6 Composite System: Fracture Results and Discussion

The inhomogeneity of the strain distribution in the composite specimens supports the general notion that it should be possible to correlate local fiber packing and the evolution of damage of the system. This was a central focus of the research program devised in this initiative. Combined with the statistical analysis techniques, the fundamental mechanistic information provided by DIC was expected to provide a predictive capability that would

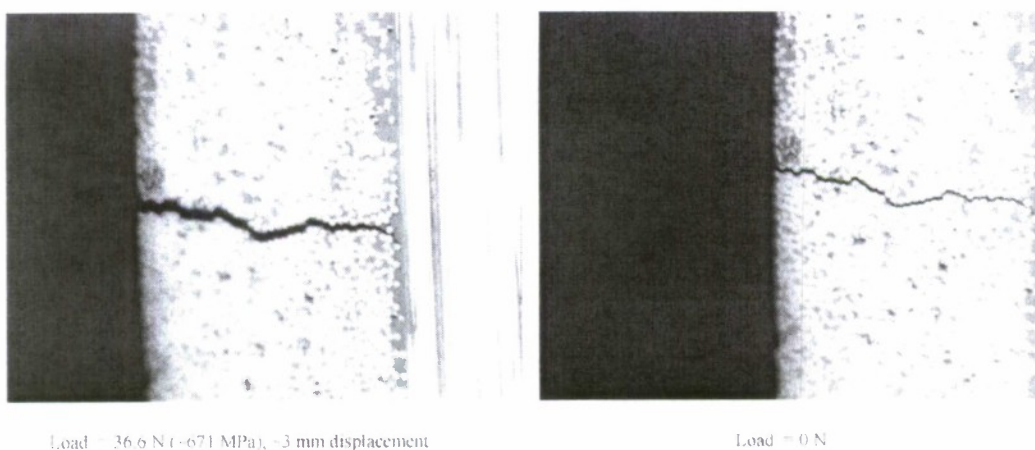


Figure 74 Cracking in the outer (tensile) ply of the composite. The crack arrested near the interface between the two plies after beginning to delaminate.

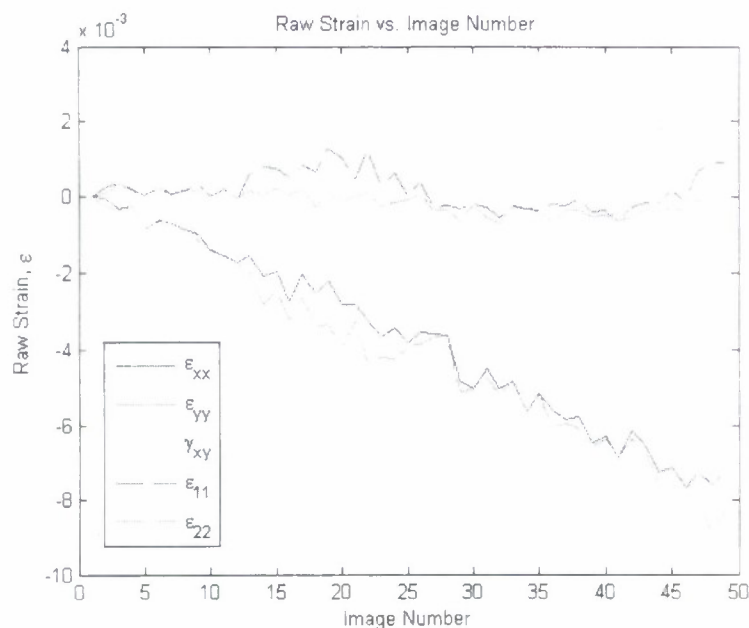


Figure 75 Evolution of strains during reloading of the cracked composite (without crack extension). The presence of the crack leads has changed the strain distribution in the ply.

allow damage susceptibility to be determined from inspection of material architecture. Consequently, a series of experiments were performed to evaluate the strain distribution in the vicinity of cracks in the outer (tensile) ply of the composite. In these experiments, the applied force was manually ramped in 1 N increments until cracks were observed (Figure 74). The cracks proceeded rapidly through the layer and arrested at the [0/90] interface, as expected. The sample was reloaded (without crack extension) and the evolution of strains was evaluated (Figure 75). As expected, the presence of the crack had modified the distribution of strains in the adjacent fibers and matrix (Figure 76) when compared to the uncracked case (Figure 69), clearly demonstrating the capability of evaluating damage evolution in composite systems. Again, no previously reported analysis of unloading due to crack propagation was found in the literature. However the importance of this measurement is evident, especially when considered in combination with the adaptive meshing techniques presented in Section 5.2.7. These tools applied in concert may provide a new technique for analysis of fracture mechanics, and certainly not solely in the context of composites. DIC has been used to detect the onset of plastic yielding and the load distribution it causes. Therefore the technique has broad implications for fracture mechanics analysis.

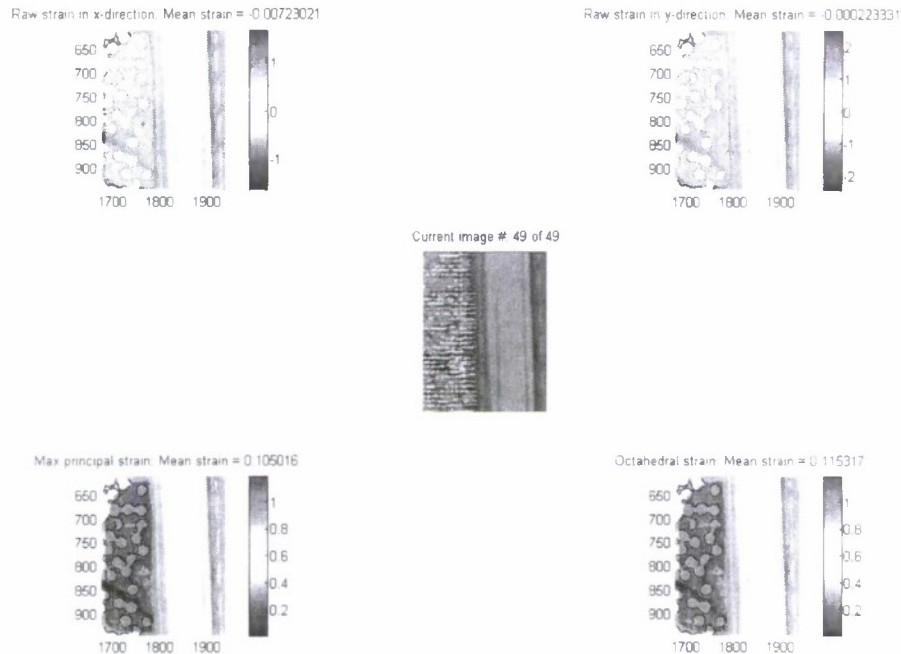


Figure 76 High resolution strain maps from the cracked portion of the composite. The presence of the crack has modified the strain distribution in the nearby fibers and matrix.

5.4 Statistical Analysis

Statistical analysis techniques were sought at the outset of the program that will allow the essential features of material variability to be represented in a fashion that clarifies its impact on structural performance. Preliminary analysis of fiber packing data provided a number of candidate statistical parameters, and effort in successive phases of the program was devoted to identifying potential links between observed microstructural variation and statistical scatter in test data.

5.4.1 Basic Methods

One key benefit of Voronoi cell analysis is that it allows parameters such as fiber volume fraction, nearest neighbor distance and number of nearest neighbors to be calculated on the scale of the fiber. Standard statistical parameters can therefore be calculated for different fiber arrangements to determine the basic structure of the data. For example, some sample populations can be conveniently interrogated by computation of Cumulative Distribution Functions (CDF) or Probability Density Functions (PDF) of parameters of interest. CDF is defined as simply the probability that some variable (volume fraction, fiber spacing, etc.) assumes a value less than or equal to some value x . It is expressed as:

$$\text{CDF} = F(x) \quad (28)$$

The probability density function is then simply the derivative of CDF and is the probability of the variable x having a certain value. It is therefore given by:

$$f(x) = \frac{dF(x)}{dx} \quad (29)$$

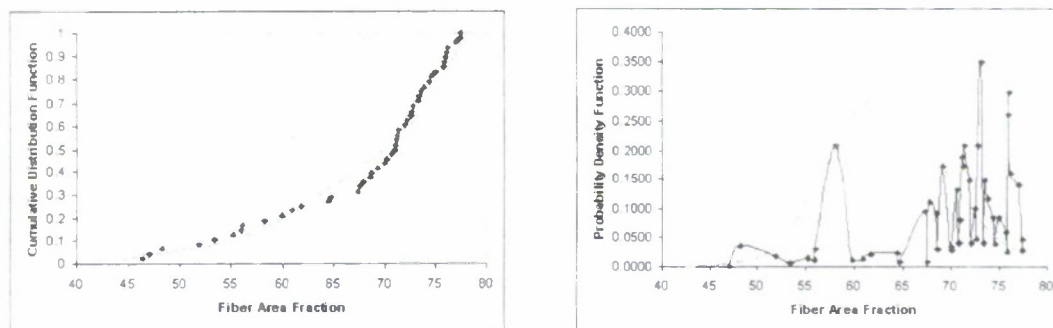


Figure 77 Cumulative Distribution Function and Probability Density Function data for Fiber Area Fraction in Sample Microstructure

Figure 77 shows these functions calculated for fiber area fraction based on an Area of Interest (AOI) containing roughly 50 fibers. In both cases the general data trend expected from a Poisson Distribution (often used to describe fiber dispersion in composites) is shown. While the CDF showed little promise in describing the material variation, the PDF exhibited some of the elements required of statistical tests for fiber packing data. For instance, the peaks in the data suggest a preference for certain packing densities that may be quite disparate in value. While it is not clear which tests or parameters will be most competent to describe the variation, it is likely that some correlation with test data may be identified, if test length scales match those of the analysis.

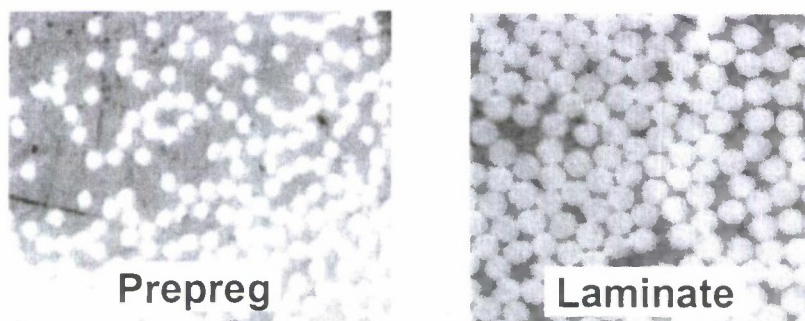


Figure 78 Micrographs of uncured graphite epoxy prepreg material and laminate fabricated by conventional autoclave processing

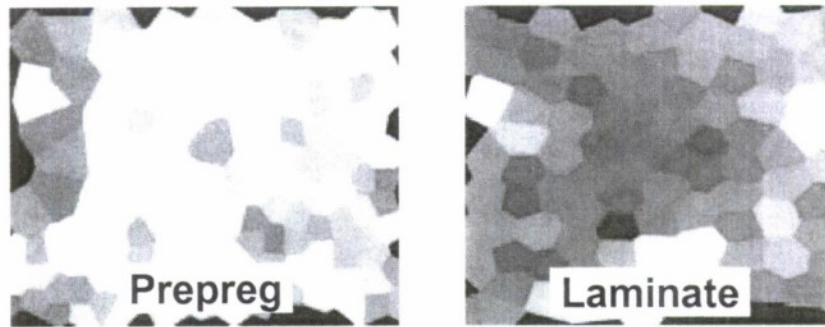


Figure 79 Fiber volume fraction maps for uncured prepreg and laminate micrographs shown in Figure 78

An illustration of how the automated image analysis tool has been used to generate data that will allow the structure of fiber packing data to be analyzed is given in Figures 78 to 80. Figure 78 shows images of uncured YLA graphite/epoxy prepreg material and a laminate processed from this prepreg by standard lay-up and autoclave cure procedures (100 psi at 350°F for 4 hours). Figure 79 shows the corresponding fiber volume fraction maps for both microstructures. The fiber volume fraction plotting facility of the automated image analysis tool outputs fiber volume fraction data for all Voronoi cells in the map to a text file that can be imported into spreadsheets or other statistical analysis

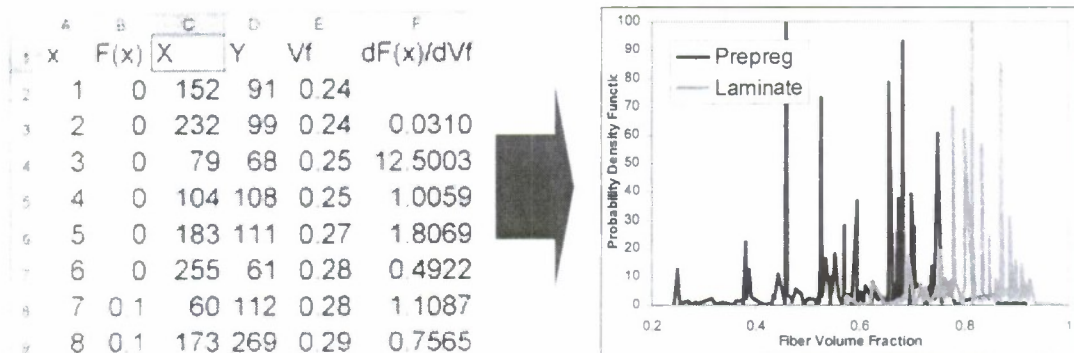


Figure 80 Example of output from automated image analysis tool being used to generate statistical data

software packages. This procedure is illustrated in Figure 80 which shows the fiber volume fraction data that is the output from the automated image analysis tool being operated on using an Excel spreadsheet. In this case the probability density function for fiber volume fraction is plotted for both the uncured prepreg and laminate images shown in Figure 78. While representing a very basic an unsophisticated analysis these data show interesting and illustrative features. Peaks in the data sets show the tendency to development of 'domains' of fiber volume fraction. Such data attributes are seen in both the prepreg and laminate numbers. This suggests that there may be a statistical mapping that would allow the final (processed) architectural parameters to be predicted from the starting point. This possibility, along with the supposition that patterns identified in packing data may influence the stochastic features of performance parameters, dictates

that significant emphasis in subsequent work was placed on identifying or developing statistical test techniques that allow such common patterns to be uncovered. Many pertinent techniques already exist. For instance, pattern recognition is a discipline that seeks to uncover what may be obscure trends in large amounts of data (in this case spatially varying fiber volume fraction). Data mining is a technique designed to extract certain features out of large databases and compare trends in different types of data. It is used in product marketing disciplines to predict purchasing trends based on personal characteristics. It might be of use in the current context to test whether trends in failure data could be related to micro features.

In neural networks (NN) certain types of data may be used to train a NN code to identify trends and then search for these trends in other types of data (again strength data and Vf data). Set theory is used (in this context) to describe the basic structure of the data. An important parameter in set theory is the Hausdorff dimension which essentially determines the dimensionality (1,2,3) of a given shape or data set. In future work it might be used to determine whether sufficient parameters (Vf, fiber spacing etc.) are being used to describe the trends in a large (say strength) dataset. Finally, discriminant factor analysis is aimed at determining the significance of selected parameters in describing a large dataset.

Determination of the appropriate scale of analysis is a key challenge that was confronted in this sub-task. Figure 32 shows prepreg (left) and laminate (right) fiber volume fraction plots similar to those shown in Figure 30, but at a much larger length scale. In this case fiber groupings of over 500 are analyzed. The corresponding probability density function for fiber area (volume) fraction data is shown in Figure 33. By comparison with Figure 31 it can be seen that many of the distinctions between the prepreg and laminate datasets are masked by the size of the data sample.

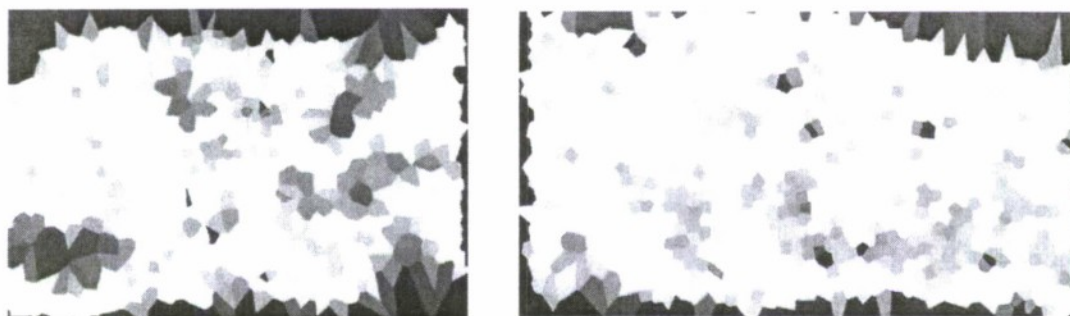


Figure 81 Fiber volume fraction plots of >500 fibers for prepreg (left) and cured laminate

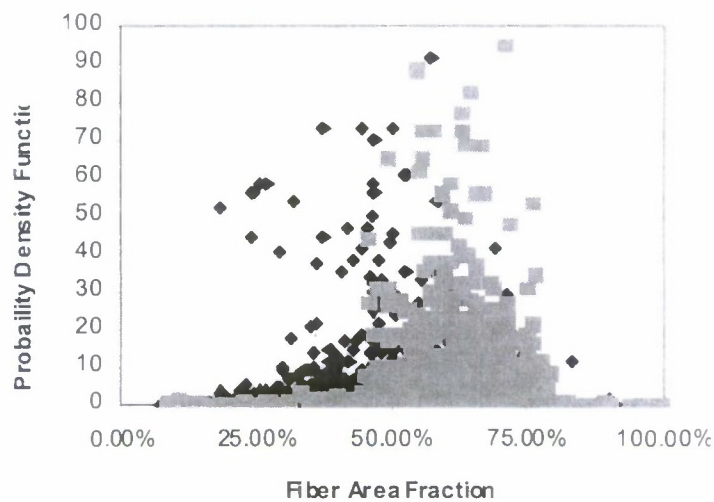


Figure 82 Probability density function of fiber volume fraction for plots shown in Figure 81 (blue – prepreg, pink – laminate)

Whatever statistical test technique is used to uncover relationships between raw material architecture and final laminate configuration and associated performance (if they exist), the combination of tools developed in this program allows experimentally verifiable analysis to be carried out at a range of different length scales. Such a capability will be invaluable in determining the impact of microstructural features on performance, crack development and resultant influence on progression of thermo oxidative degradation processes.

5.4.2 Multivariate Characterization of Microstructures

An initiative was been undertaken to use multivariate analysis techniques to develop a mathematical model of the microstructure of fiber composites. Although engineering intuition suggests properties of the microstructure that are probably important, the observed variations are far too complex to have ever been characterized in a mathematical model of higher fidelity than the fiber volume fraction yet more concise than the complete x-y map of the fibers. Indeed the fiber volume fraction map itself (described above) is a breakthrough in data collection methods. The multivariate approach allows unconstrained experimentation with variables in the new data rich x-y maps while enforcing order on the results.

There have been three repeating steps supporting the effort:

- conceiving variables to measure (or compute) from the x-y map
- writing C++ code to efficiently compute the growing list of variables from each composite cross-sectional sample
- cutting, polishing, photographing and image-processing cross-sectional composite samples

Over 200 samples were measured with the goal to surpass 1000 samples to get the robust statistics upon which the approach rests. From each of these samples many different

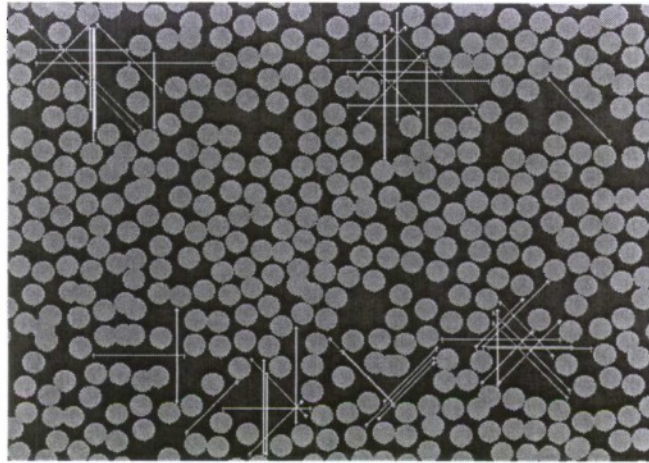


Figure 83. Portion of the output for the variable, "50 longest runs at 0°, 45°, 90°, and 135°"

measurements are taken, giving many distinct variables. The algorithms for these measurements fall roughly into four distinct categories:

Resin Area Analysis splits the cross-sectional image into segments to find the area and general shape of each resin pocket within a sample. Some examples of variables obtained by this analysis include:

- Largest resin pocket area
- Total area occupied by resin
- Largest/smallest resin height/width ratios

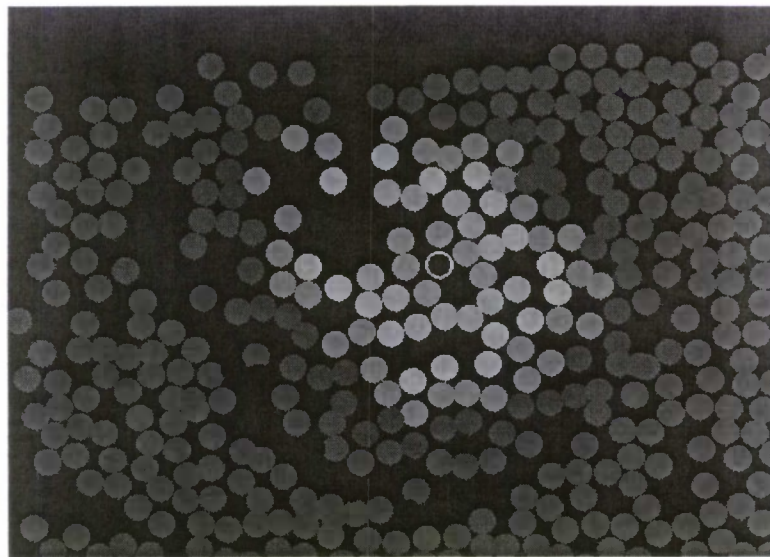


Figure 84 Delaunay triangulation analysis for the white circled cell, showing successive layers of neighboring cells

Linear Distance Analysis computes the lengths of all straight-line runs through resin at any angle (Figure 83). This analysis gives a more detailed look at the subtleties of the shape of each resin pocket, yielding variables such as:

- Longest vertical run
- Variance of longest run lengths for each of 8 different angles
- Average of the 50 longest runs (see Figure 26)

Voronoi Diagram Analysis. Creates a Voronoi diagram for the cross-section and computes the "density" (FVF) of each cell based on relative fiber volume. Several observations can then be made such as:

- Fiber Volume Fraction gradient along a given angle
- Variance of FVF

Delaunay Triangulation Analysis. This Triangulation connects each data point to its nearest neighbors so that the resulting set of interconnecting lines forms a triangular mesh, or grid. While other methods view fibers as independent points, this method represents each point as part of a network, so the relationship of each fiber to other fibers in its proximity can easily be observed:

- Average # of "next-door" neighbors per fiber
- Variance of the average distance from each point to its 20 nearest neighbors
- Variance of the average length of the perimeters formed by each layer of neighbors (see Figure 84)

The first step of the multivariate analysis approach is to take as much information from as many samples as possible. Each of the analyses mentioned can be tapped to yield a great number of variables; code was written to extract over 100 variables from each sample, with room for many more to be implemented in the future. Not only is a large quantity of variables needed, but also a large quantity of disparate variables so that the many subtle differences and nuances of each sample are accounted for.

Next, all of the variables are correlated with each other, yielding a table that shows which variables are closely related. If two variables have high correlations for a very large number of samples, it may be inferred that the variables are sensitive to some common property of the fiber distributions. If the two variables are also very dissimilar in what they measure, yet highly correlated, then whatever is common to both of them must be a more fundamental attribute than the attributes of the two variables measured alone. Consider binocular vision; although each eye sees only a plane on its own, when two eyes are used simultaneously with slightly different viewpoints, a new dimension of depth is achieved. Similarly, if many eyes are used, with drastically different viewpoints, a deeper understanding can be obtained from many "shallow" pieces of information. By using many variables (eyes) that measure a wide range of properties of each sample, which is ensured by the four disparate analyses used for variable collection mentioned above, a mathematical characterization of sufficient fidelity to support the next phase of

the research – correlation of the model images of the samples with measurable strength properties of the samples may be achieved.

Concurrent with the statistical database population, the modern updates to the theory of multivariate factor analysis were studied in order to give the approach every possibility of success. The general theme of factor analysis is that grouping different yet related variables into factors improves the robustness of statistical measures because of the relative rarity of fluke measurements occurring in many variables simultaneously. The specific choice of primary factors out of all possible rotations of axes, choice of whether to keep all the variables experimented with, and many other choices to be made in applying factor analytic methods will depend on the characteristics of the data that emerge through the correlation process when enough data points to stabilize the correlations have been acquired.

Once stable factors have been found, the final stage of the analysis can be undertaken, namely destructive testing of the composites that have been sampled and correlation of their strength properties with the corresponding points in factor space. If this correlation is not initially found, the choices made in the factor modeling can be experimented with to improve correlation with strength properties and, if necessary, further variables can be added or deleted in an effort to identify the right combination of variables to develop a model of microstructure capable of predicting strength properties of the material with confidence levels that compete with (and ideally surpass) the current lengthy and expensive destructive testing methods.

5.4.3 Statistical Correlation with Measured Data

Advanced techniques such as multivariate analysis rely on large databases that can be correlated to some measurable performance metric. In this program a large study has been conducted on the development of microcrack data under varying dynamic load conditions. Fiber center and distribution data have been collected for tensile samples with approximately 10,000 fibers being analyzed. These samples were then subjected to fatigue loading up to the point of microcrack saturation and the areas of interest re-photographed. This allows the cracks to be precisely located in the strain space, permitting the FEA techniques described above to be applied in determining the effects of local packing variations. However it also allows the fiber population in regions surrounding cracks to be subjected to rigorous multi-variate and factor analysis. It is understood that edge cracks are unlikely to represent initiation points, but the frequency of occurrence may be related to multi-variate parameters. To facilitate this an analysis tool was developed that highlights cracks generated in fatigue specimens by viewing in the dark field. This is shown in Figure 28 where the neighboring fibers are also highlighted. Slight blurring at the edges of the image is due to the fact that this is a compound image, consisting of the cracked microstructure overlaid on the original.

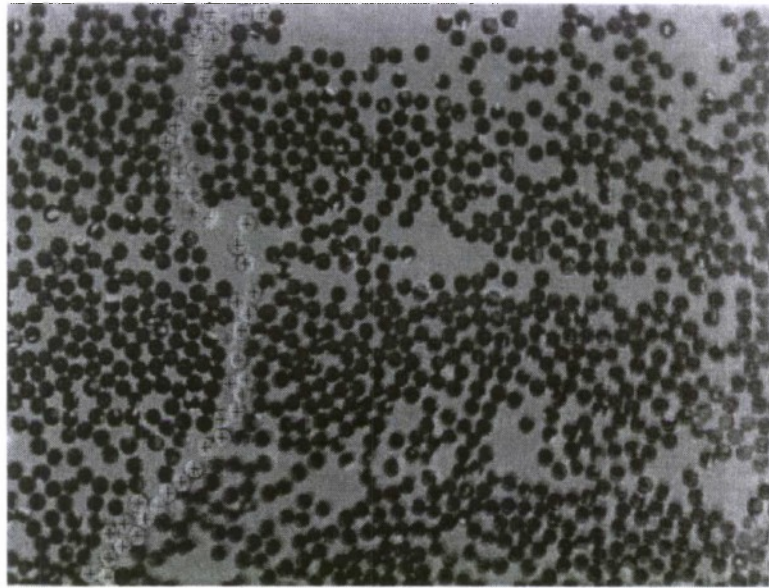


Figure 85 A microcrack located in a composite microstructure along with neighboring fibers

6.0 Concluding Remarks

A broad set of ambitious project goals was laid out in the program proposal. When work began in 2005 it was decided that the stated principal objective, to provide a rapid material implementation methodology for high temperature polymer matrix composites, could best be achieved by development of a suite of high fidelity models and analysis tools that allowed the critical material attributes to be determined from fundamental properties. A hierarchical structure for model development was proposed that would link together the critical properties modeled at distinct length scales to yield a structural analysis capability. This approach is represented schematically in Figure 86. It was felt that at each stage in the evolution, critical analyses and experiments would need to be conducted before the next level of development was attempted. This approach led to an early focus on the study of fundamental material phenomena and evaluation of alternatives for test and analyses techniques that could be sufficiently flexible and adaptive to emerging knowledge. It was in this early stage that it was decided that the basic vehicle for material modeling, both for determination of long term thermo-oxidative behavior and resultant material mechanics, should be Finite Element Analysis. This option was chosen for a number of reasons. Primarily, it was felt that a good deal of the underlying mechanisms of high temperature degradation of polymer composites remained uncharacterized. Similarly the fundamental mechanics of crack formation in loaded composite structures, while studied thoroughly, had not reached a level of scientific consensus. It was therefore believed that an FEA representation of such effects provided for the necessary flexibility in treatment required in complex systems.

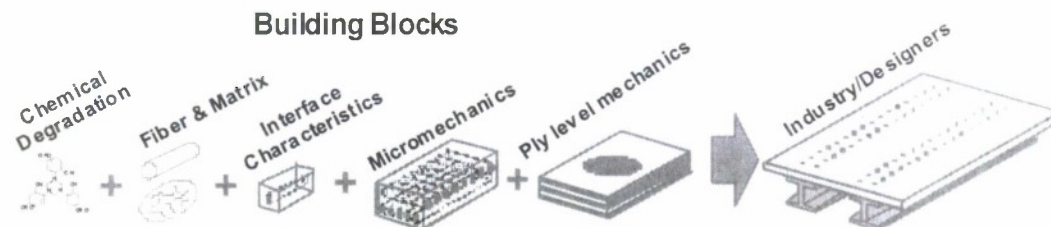


Figure 86 Levels at which modeling effort was devoted in an effort to provide for a fully integrated predictive capability

At the conclusion of this program it is evident that the initial overarching goal of the initiative has not been achieved. Notwithstanding limitations in schedule and applied resources there are a number of reasons for this result. A very complex set of mechanisms interact to manifest in thermo-oxidative degradation of polymer matrix composites. Polymers within composites are organized differently on the molecular scale, to their bulk form. The existence of the interphase effectively represents a third material within the system. Oxygen ingress, which fuels the critical degradation reaction, is facilitated by microcracking, but the existence of a degraded material envelope may set up the stress patterns that cause micro-cracking in the first place. Such complex cause and effect relationships and their relative contributions to overall behavior must be accounted for in any comprehensive treatment. The program team stepped through these issues in a structured way and in the final analysis all elements of the building block approach were addressed in some depth. For instance, the degradation mechanisms of high temperature polymers were studied early on and a basic phenomenological model of material behavior was formulated. The roles of fibers and resins in the degradation composite systems were studied independently and in combination and gaps in material knowledge were highlighted as the work progressed. Reliable directional data for diffusivity in fibers and interfaces are not available, but a sensitivity analysis when compared to experimental measurements provided a self consistent description of observed behavior. The effect of physical and chemical aging on unreacted polymer material was also incorporated into the model description of composite response, and the result was an analysis framework that included the key components of lamina response prediction capability.

Developments aimed at determining damage mechanics of high temperature polymer matrix composites were focused on understanding the fundamental nature of ply cracking, and sought to provide an analysis capability that would uncover the link (if any) between material architecture and resultant failure mechanics. This was thought to be a particularly critical topic in characterizing thermo-oxidative degradation, since the formation of sub surface cracks was shown to have a dramatic effect on oxygen ingress. Adaptive meshing techniques were developed that allowed real microstructures to be interrogated in the stress and strain domains and the fundamental link between recognizable features and the occurrence of cracks was studied. It was not possible, however, to apply this tool in a multi-scale analysis environment though the basic outline of such an analysis was established. However, studying stress and strain profiles at the

fiber level only acquired scientific value with the application of Digital Image Correlation which allowed measurement of these parameters for the first time. It was shown that the general trends predicted by the adaptive FEA techniques were actually observed in the DIC measurements, though program activity ended before the full potential of this tool could be realized. Similarly, an initiative was undertaken to uncover the statistical parameters in fiber packing data that might be related to failure mechanisms and a large database was developed that would allow such properties or 'factors' to be identified. It is intended that this tool be applied to the large amount of micro-cracking data generated in this program.

The MEANS II program has been successful in developing a suite of analysis tools that forms a solid framework for the determination of the durability of high temperature polymer matrix composites. Integration of these tools into a design development database remains as a task that would assemble the key elements of the solution originally proposed. A large number of resultant publications detail the various fundamental phenomena studied in the program. Many of these analyses will be applied in future initiatives aimed at rapid characterization of certification of high temperature polymer matrix materials as well as other systems.

7.0 Personnel Supported

The following personnel were supported by this MEANS II program:

Dr. Gregory A. Schoeppner- Senior Materials Engineer- AFRL/MLBC
Dr. G.P. Tandon – Distinguished Researcher - Univ of Dayton Research Institute
Mr. Erik Ripberger – Materials Engineer - Univ of Dayton Research Institute
Mr. Ken Goeke – Technician - Univ of Dayton Research Institute
Mr. Josh Briggs – Materials Engineer - Univ of Dayton Research Institute
Mr. Mike Nickell – Materials Engineer - Univ of Dayton Research Institute
Mr. Bill Ragland – Technician - Univ of Dayton Research Institute
Dr. Sirina Putthanirat – Materials Engineer – Univ of Dayton Research Institute
Ens Susan Mendelhall – MS student – Air Force Institute of Technology
Ens Grant Robinson – MS student – Air Force Institute of Technology
Ens Patrick Link – Air Force Institute of Technology
Ms Susanna Branion – Univ of Dayton
Prof Hongbing Lu – Oklahoma State University
Prof Samit Roy – University of Alabama
Prof Marina Ruggle-Wrenn - Air Force Institute of Technology
Prof. Kishore Pochiraju – Prof of Mechanical Eng. – Stevens Institute of Technology.
Eva Yu - Ph.D. Student – Stevens Institute of Technology
Yunn-Tzu Yu – PhD Student - Stevens Institute of Technology
Shaochen Fan – PhD student - Stevens Institute of Technology
Harold Cook - Undergraduate Researcher – Stevens Institute of Technology
Dr. Gregory P. Dillon – Research Engineer, Principal Investigator – ARL/Penn State
Dr. James Tarter – Research Associate – ARL/Penn State
Terri Merdes – Research Associate – ARL/Penn State
Adam Roslund - Assistant Research Engineer – ARL/Penn State
Deborah Corl – Administrative Assistant - ARL/Penn State
Linda Jones - Administrative Assistant - ARL/Penn State
James Collins – Material Science and Eng Graduate Student - Penn State University
Prof. Christopher Muhlstein – Associate Professor – Material Science and Engineering -
Penn State University
Prof. James Runt – Professor – Material Science and Engineering - Penn State University
Dr. Christopher Byrne – Research Associate – ARL/Penn State
Michael Dougherty – Graduate Student - Penn State University

8.0 Publications

The following papers were published or accepted for publication as a result of program funding and during the period of performance:

1. Ripberger, E., Tandon, G.P., and Schoeppner, G.A., "*Characterizing Oxidative Layer Development in AFRPE-4 Resin*," Proceedings of SAMPE 2004, San Diego, CA, 15-18 Nov 2004
2. Ripberger, E.R., Tandon, G.P., and Schoeppner, G.A., "*Anisotropic Oxidation Behavior of Unidirectional G30-500/PMR-15 Composites*," Presented at the SAMPE 2005 Symposium & Exhibition Long Beach, California, May 1-5, 2005
3. Pesta, B.L., Murray, P.T., Thorp, K.T., and Schoeppner, G.A., "*XPS Evaluation of AFR-PE-4 High Temperature Polyimide*," Presented at the SAMPE 2005 Symposium & Exhibition Long Beach, California, May 1-5, 2005
4. Tandon, G.P., Pochiraju, K., and Schoeppner, G.A., "*Modeling of Oxidative Development in PMR-15 Resin*," Presented at the SAMPE 2005 Symposium & Exhibition Long Beach, California, May 1-5, 2005
5. Ripberger, E., Tandon, G.P., and Schoeppner, G.A., "*Experimental Techniques for Characterizing Thermo-Oxidative Behavior in High Temperature Polyimide Composites*," Proceedings of the 2005 SEM Annual Conference & Exposition, Portland, OR, June 7-9, 2005
6. Tandon G.P., Ripberger E.R., and Schoeppner, G.A., "*Accelerated Aging Of PMR-15 Resin at Elevated Pressure and/or Temperature*," Presented at the SAMPE Fall Technical Conference, Seattle, WA, Oct 31- Nov, 2005
7. Pochiraju, K.V., Schoeppner, G.A., and Tandon, G.P., "*Role of Fiber-Matrix Interface on the Thermo-Oxidative Degradation*," Proceedings of the American Society of Composites Conference, Philadelphia, PA, September 7-9, 2005
8. Pochiraju, K. and G. Tandon "*Modeling Thermo-Oxidative Layer Growth in High-Temperature Resin*," Journal of Engineering Materials and Technology, January 2006, Volume 128, Issue 1, pp. 107-116
9. Tandon, GP., Pochiraju, KV, and Schoeppner, G.A., "*Modeling of Oxidative Development in PMR-15 Resin*," Polymer Degradation and Stability, 91(8), Aug 2006, 1861-1869
10. Schoeppner GA, Tandon GP, and Ripberger ER, "*Anisotropic Oxidation and Weight Loss in PMR-15 Composites*," Composites Part A: Applied Science and Manufacturing, 38(3), March 2007, 890-904
11. Schoeppner, GA, Tandon, GP and Pochiraju, KV, "*Predicting Thermo-Oxidative Degradation and Performance of High Temperature Polymer Matrix Composites*" in Multiscale Modeling and Simulation of Composite Materials and Structures, Kwon, Allen, Talreja (Eds) Springer
12. Putthanarat S, Tandon GP, and Schoeppner GA, "*Influence of Polishing Time on Thermo-Oxidation Characterization of Isothermally Aged PMR-15 Resin*," Accepted to *Polymer Degradation and Stability*, June 2007
13. Pochiraju, KV, Tandon, GP, Schoeppner, GA, "*Evolution of Stress and Deformations in High Temperature Polymer Matrix Composites during Thermo-*

Oxidative Aging," submitted to *Journal of Engineering Materials and Technology*, Aug 2007

14. Pochiraju, K., H. Cook, Tandon, G., and Schoeppner, G., " *Modeling Thermo-Oxidation in High Temperature Polymer Matrix Composites*," Proceedings of the American Society for Composites, 21th Annual Technical Conference , September 17-20, 2006 – Dearborn, MI
15. Pochiraju, KV, Tandon, GP and Schoeppner, GA,, " *Modeling Viscoelastic Response of Polymer Matrix Composites in Thermo-Oxidative Environments*," Presented at Symposium on Joining Technologies for Advanced Materials and Structures, International Mechanical Engineering Congress and Exposition, Orlando, FL, Nov 5-11, 2005.
16. Tandon, G.P., Briggs, J., and Schoeppner, G.A., " *Thermo-oxidative Degradation of Carbon Fibers for High Temperature Polymer Matrix Composites*," Proceedings of the American Society for Composites, 21th Annual Technical Conference , September 17-20, 2006 – Dearborn, MI
17. Tandon, GP and Schoeppner, GA, " *Thermo-Oxidative Behavior Of Unidirectional T650-35/AFR-PE-4 Composites*," Presented at SAMPE 2006, Long Beach, CA, April 30-May 4, 2006.
18. Tandon, GP, Ripberger, ER, and Schoeppner, GA, " *Accelerated Aging of PMR-15 Resin at Elevated Pressure and/or Temperature*," Presented at SAMPE 2005, Seattle, WA, Oct. 31 -Nov. 3, 2005.
19. Schoeppner GA and Tandon GP, " *Thermo-Oxidative Behavior of BMI Resin and Composites*," presented at High Temple 2007, Sedona, AZ, Feb 12-15, 2007
20. Pochiraju KV, Tandon GP, Schoeppner GA, " *Coupled Damage and Thermo-Oxidative Evolution in High Temperature Polymertic Matrix Composites*," presented at High Temple 2007, Sedona, AZ, Feb 12-15, 2007
21. Tandon GP, Pochiraju KV, and Schoeppner GA, " *Thermo-oxidative Behavior of High Temperature PMR-15 Resin and Composites*," Second International Conference On Recent Advances In Composite Materials (ICRAM-2007), Feb 20-23, 2007
22. Putthanarat S, Tandon GP, Schoeppner GA, " *Effect of Polishing Time on Measured Oxidation Thickness and Elastic Modulus of Isothermally Aged PMR-15 Neat Resin*," Presented at SAMPE 2007, Baltimore, MD, June 3-7, 2007.
23. Pochiraju KV, Tandon GP, Schoeppner GA, " *Time Dependent Evolution of Stress and Strain Fields in Composites during Thermo-Oxidation*," Presented at ASME Applied Mechanics and Materials Conference (McMat 2007), June 3-7, 2007, University of Texas at Austin
24. Tandon GP, Pochiraju KV, Schoeppner GA, " *Thermo-Oxidative Behavior of PMR-15 Resin and Composites*," Presented at ASME Applied Mechanics and Materials Conference (McMat 2007), June 3-7, 2007, University of Texas at Austin
25. Tandon GP, Ragland WR, and Schoeppner GA, " *Monitoring Anisotropic Oxidation Growth in High Temperature Polymer Matrix Composites*," to be Presented at 22nd American Society of Composites Conference, Seattle, WA Sept 17-20, 2007

26. Schoeppner GA, Tandon GP, and Pochiraju KV, "*Modeling Thermo-Oxidation of Polymer Matrix Composites*," to be presented at Stretching the Endurance Boundary of Composite Materials: Pushing the Performance Limit of Composite Structures, Island of Maderia, Portugal, 23-28 Sept 2007
27. Putthanarat S, Tandon GP, and Schoeppner GA, "*Influence of Polishing Time on Thermo-Oxidation Characterization of Isothermally Aged PMR-15 Resin*," *Polymer Degradation and Stability*, 2007
28. Pochiraju, KV, Tandon, GP, Schoeppner, GA, "*Evolution of Stress and Deformations in High Temperature Polymer Matrix Composites during Thermo-Oxidative Aging*," *Journal of Engineering Materials and Technology*, 2007

9.0 Interactions/Transitions

Interactions and transitions have been continued in this program as outlined below.

9.1 Presentations at Conferences/Meetings

1. Pochiraju, K., Tandon, G.P., and Schoeppner, G.A., "Thermo-Oxidative Degradation in Polymer Matrix Composites," Presented at High Temple Workshop, 14-17 February 2005, Clear Point Alabama
2. Ripberger, E.R., Tandon, G.P., and Schoeppner, G.A., "Isothermal Oxidative Aging of PMR-15 and AFR-PE-4 Resins and Composites," Presented at High Temple Workshop, 14-17 February 2005, Clear Point Alabama
3. Pesta, B., Schoeppner, G.A., Thorp, K.E.G., and Murray, P.T., "XPS Evaluation of AFR-PE-4 High Temperature Polyimide," Presented at High Temple Workshop, 14-17 February 2005, Clear Point Alabama
4. G. P. Tandon, K. Pochiraju, and G. A. Schoeppner, "Modeling Of Oxidative Development in PMR-15 Resin", SAMPE May 1-5, 2005, Long Beach, CA
5. Kishore V. Pochiraju, Gregory Schoeppner, Gyaneswar P. Tandon, "Role of Fiber-Matrix Interface on the Thermo-Oxidative Degradation," Proceedings of the 20th Technical Conference of the American Society for Composites, Drexel University, Philadelphia, PA, September 7-9, 2005.
6. R. Hall, G. Schoeppner, K. Pochiraju, G. Tandon, E. larve, D. Mollenhauer, "Progress Toward Thermodynamic Environmental Durability Modeling of High Temperature Polymer Matrix Composites", Proceedings of the 5th International Conference on Mechanics of Time Dependent Materials (MTDM-5), Karuizawa, Nagano, Japan, Oct. 3-6, 2005.
7. Dillon G, G. Schoeppner and K. Pochiraju "Automated Analysis Tools for Determination of Structural Integrity and Durability of High Temperature Polymer Matrix Composites", AFOSR Polymer Program Review, San Diego, CA, August 12th, 2005
8. Briggs, J., Tandon, GP, and Schoeppner, GA, "Thermo-Oxidative Degradation of Carbon Fibers and Carbon-Fiber Reinforced Composites," Presented at 1st Dayton Engineering Sciences Symposium, Dayton, OH Oct. 31, 2005.
9. Pochiraju, KV, Tandon, GP and Schoeppner, GA, "Long Term Micro-Mechanical Behavior Modeling of High Temperature Polymeric Composites," Presented at High Temple 26th Workshop, Austin, Texas, Feb. 13-16, 2006.
10. Pochiraju, KV, Tandon, GP and Schoeppner, GA,, "Modeling Viscoelastic Response of Polymer Matrix Composites in Thermo-Oxidative Environments," Presented at Symposium on Joining Technologies for Advanced Materials and Structures, International Mechanical Engineering Congress and Exposition, Orlando, FL, Nov 5-11, 2005.
11. Putthanarat, S., Tandon, G.P. and Schoeppner, G.A., "Influence of Temperature, Time and Environments on PMR-15: Nanomechanical Characterization," presented at 31st Dayton Cincinnati Aerospace Science Symposium, Dayton, OH, March 7, 2006

12. Schoeppner, GA and Tandon, GP, "Oxidation and Weight Loss in PMR-15 and AFR-PE-4 Composites," Presented at High Temple 26th Workshop, Austin, Texas, Feb 13-16, 2006.
13. Schoeppner, GA, Pochiraju, KV, Tandon, GP," Long-Term Aging and Durability of High Temperature Polymer Composites," Presented at COMPTTEST 2006, 10-12 April 2006, Porto, Portugal
14. Dillon G. "Rapid Design Database Development for High Temperature Polymer Matrix Composites" AFOSR Polymer Program Review, Long Beach, CA, May 6th, 2006
15. Kishore V. Pochiraju, Gregory Schoeppner, Gyaneswar P. Tandon, "Oxidative Degradation in High Temperature Polymer Matrix Composites", Proceedings of the 21st American Society For Composites, Dearborn, MI, September 2006
16. Dillon G. "Multi Scale Deformation Mechanics Modeling of Carbon Fiber Composites," Carbon Workshop, Penn State University, University Park, PA, October 16-17, 2006
17. Defense Sciences Research Council Workshop on Reliable Polymer Studies, Chicago, IL Feb 8 2007
18. Dillon G. "Rapid Design Database Development for High Temperature Polymer Matrix Composites" AFOSR Polymer Program Review, National Composite Center, Kettering, OH, August 8th, 2007
19. USAF Special SAB Study: Presentation on Composites Sustainability – 17 May 2007, WPAFB

9.2 Consultative and Advisory Functions to Other Laboratories and Agencies

None.

9.3 Technology Transitions

Technologies at a maturity level necessary for transfer to government agencies or industry were not developed in the duration of this program. However the non contact strain measurement techniques developed (Digital Image Correlation) continue to be developed under internal funding at Penn State, with a view to incorporation into material and structure qualification protocols for Defense applications.

10.0 New Discoveries, Inventions, or Patent Disclosures

No new discoveries, inventions or patent disclosures have resulted from the initial stages of program research.

11.0 Honors/Awards

No honors or awards have resulted from the initial stages of program research.

12.0 References

1. Ripberger, E.R., Tandon, G.P. and Schoeppner G.A., "Characterizing Oxidative Degradation Of PMR-15 Resin ", Proceedings of the SAMPE 2004 Symposium/Exhibition May 16-20, Long Beach, California (ITAR restricted)
2. Nam, J.D. and Seferis, J.C., "Anisotropic Thermo-oxidative Stability of Carbon Fiber Reinforced Polymeric Composites," SAMPE Quarterly, Vol 24, No. 10, 1992, pg. 8
3. Skontorp, A., "Isothermal High-Temperature Oxidation, Aging and Creep of Carbon-Fiber/Polyimide Composites," Dissertation University of Houston, May 1995
4. Bowles, K.J. and Nowak, G., "Thermo-Oxidative Stability Studies of Celion 6000/PMR-15 Unidirectional Composites, PMR-15, and Celion 6000 Fibers," Journal of Composite Materials, Vol 22, Oct 1988, pp. 966-985
5. Bowles, K.J., Tsuji, L., Kamvouris, J., and Roberts, G.D., "Long-Term Isothermal Aging Effects on Weight Loss, Compression Properties, and Dimensions of T650-35 Fabric-Reinforced PMR-15 Composites – Data," NASA TM-2003-211870 (2003)
6. Thorp, K.E., PhD Dissertation, University of Dayton, December 2000
7. Wise, J., Gillen, K. T., Clough, R. L. "Quantitative model for the time development of diffusion-limited oxidation profiles." Polymer, 38, 1929-1944 (1997)
8. Gibson T, Price W, Arnold F, Uttermohlen D, Storage T, Jacques A (2006) Physical and mechanical properties of AFR-PE-4 and BIM-15 with S-2 and Astroquartz-III composites. Presented at 26th High Temp Workshop, Austin, TX
9. Eckstein BH (1981) The oxidation of carbon fibers in air between 230°C and 375°C. Fiber Science and Technology 14:139-156
10. Gibbs HH, Wendt RC, Wilson FC (1979) Carbon fiber structure and stability studies. Polymer Engineering Science 19:342-349
11. Bowles KJ (1992) Effect of fiber reinforcements on thermo-oxidative stability and mechanical properties of polymer matrix composites. SAMPE Quarterly April 2-12
12. McMahon PE (1978) Oxidative resistance of carbon fibers and their composites. In Advanced Composite Materials-Environmental Effects, ASTM STP 658, J. R. Vinson, Ed., American Society for Testing and Materials, pp. 254-266
13. Wong MS, Skontorp A, Wang SS (1994) Thermal oxidation of carbon fibers and carbon-fiber reinforced high-temperature polyimide composite at elevated temperature. In: Proc. of Am. Soc. Comp. -9th Tech. Conf., Technomic Publ. Co., Lancaster, PA., 458-467
14. Tandon GP, Briggs J, Schoeppner GA (2006) Thermo-oxidative degradation of carbon fibers for high-temperature polymer matrix composites. Proceedings American Society for Composites, 21st Technical Conference, Univ. of Michigan-Dearborn, Dearborn, MI
15. Tandon, G. P., K. V. Pochiraju, and G. A. Schoeppner. 2007. "Thermo-Oxidative Behavior of High Temperature PMR-15 Resin and Composites," presented at 2nd International Conference on Recent Advances in Composite Materials, New Delhi, India, Feb. 20-23, 2007.

16. Amodio, D., et al., "Digital speckle correlation for strain measurement by image analysis." *Experimental Mechanics*, 2003. **43**(4): p. 396-402.
17. Abanto-Bueno, J. and J. Lambros, "Investigation of crack growth in functionally graded materials using digital image correlation." *Engineering Fracture Mechanics*, 2002. **69**(14-16): p. 1695-711.
18. Lafarie-Frenot, M.C., C. Henaff-Gardin, and D. Gamby, "Matrix cracking induced by cyclic ply stresses in composite laminates." *Composites Science and Technology*, 2001. **61**(15): p. 2327-2336.
19. Sutton, M., et al., "Determination of displacements using an improved digital correlation method." *Image and Vision Computing*, 1983. **1**(3): p. 133-139.
20. Knauss, W.G., I. Chasiotis, and Y. Huang, "Mechanical measurements at the micron and nanometer scales." *Mechanics of Materials*, 2003. **35**(3-6): p. 217-231.
21. Sutton, M.A., et al., "Application of an Optimized Digital Correlation Method to Planar Deformation Analysis." *Image and Vision Computing*, 1986. **4**(3): p. 143-150.
22. Lagattu, F., J. Brillaud, and M.-C. Lafarie-Frenot, "High strain gradient measurements by using digital image correlation technique." *Materials Characterization*, 2004. **53**(1): p. 17-28.
23. Zapata, M.C., A. Minor, and C.L. Muhlstein, "Strain localization and fatigue in ultra-fine grained nickel films." 2006, International Congress on Fatigue, Fatigue 2006, Atlanta, GA.
24. ASTM, E 8 "Standard test methods for tension testing of metallic materials." *Annual Book of ASTM Standards*. Vol. 03.01. 2001, West Conshohocken, PA: ASTM. 56-76.
25. Zapata, M.C., A. Minor, and C.L. Muhlstein, "Fatigue of Electrodeposited Nickel Films, in TMS Annual Meeting: Mechanical Properties of Thin Films and Small Structures." 2005: San Francisco, CA.
26. Eberl, C., "Digital Image Correlation and Tracking with Matlab". 2007.